Department of Physics and Astronomy

University of Heidelberg

Diploma Thesis in Physics

submitted in November 2009

by Robert Gast, born in Gießen, Germany

Investigating Systematics in the Energy Reconstruction of the H.E.S.S. Telescopes

This diploma thesis has been carried out

by Robert Gast

at the Max-Planck Institute for Nuclear Physics

under the supervision of

Prof. Werner Hofmann

Abstract

H.E.S.S. is an array of four Imaging Atmospheric Cherenkov Telescopes that aims at exploring the non-thermal universe by means of photons with energies between 100 GeV and 100 TeV. These very-high-energy (VHE) γ-rays can be detected and their energy can be reconstructed by observing the Cherenkov light of extensive particle showers the VHE γ-rays induce in the atmosphere.
This work presents systematical studies of the H.E.S.S. energy reconstruction. The differences in the responses of the individual telescopes are tested and it is investigated whether such asymmetries have an effect on the overall accuracy of the energy reconstruction. Therefore the H.E.S.S. Standard Analysis is tested using Monte Carlo simulations and VHE γ-ray data sets obtained from the observation of the Crab Nebula and the active galactic nucleus PKS 2155–304.
Minor differences in the telescope responses at percentage level are found, which have increased slightly during the last five years, mirroring the decay of the optical components of the telescopes. However, the effect of these inter-telescope systematics on the energy reconstruction is negligible, especially when compared to the $\simeq$ 17% overall energy resolution of the experiment.

Kurzfassung

H.E.S.S. ist ein System vier abbildender Cherenkov-Teleskope, welches die Beobachtung des nicht-thermischen Universums mittels der Detektion von Photonen mit Energien zwischen 100 GeV and 100 TeV ermöglicht. Mithilfe des Cherenkovlichtes ausgedehnter Teilchenschauer in der Atmosphäre kann diese hochenergetische Gammastrahlung nachgewiesen und die Energie der Gammaquanten bestimmt werden.
Die vorliegende Arbeit befasst sich mit systematischen Studien der H.E.S.S. Energierekonstruktion. Es wird überprüft, ob Unterschiede im Verhalten der einzelnen Teleskope bestehen und ob solche Asymmetrien eine Auswirkung auf die Genauigkeit der Energierekonstruktion haben. Zu diesem Zweck wird die H.E.S.S. Standard-Analyse mit Monte Carlo-Simulationen und Beobachtungsdaten des Krebsnebels sowie des aktiven Galaxienkerns PKS 2155–304 getestet.
Diese Untersuchungen offenbaren geringfügige Unterschiede auf Prozentniveau zwischen den einzelnen Teleskopen. Die Asymmetrien haben sich im Laufe der letzten fünf Jahre leicht vergrößert, was auf die Verschlechterung der optischen Komponenten der Teleskope zurückzuführen ist. Diese Effekte zwischen den Teleskopen haben jedoch keinen signifikanten Einfluss auf die Energierekonstruktion, insbesondere da die Energieauflösung des Experiments mit $\simeq$ 17% deutlich ungenauer ist.

Contents

List of Figures

List of Tables

Chapter 1

Introduction and Motivation

> *If a man will begin with certainties, he shall end with doubts; but if he will be content to begin with doubts, he shall end in certainties.* – Francis Bacon (English philosopher, 1561-1626, "The advancement of learning")

Since the scientific revolution in the 16th and 17th century, doubt has been the driving force of progress. Books like Rene Descartes' *"Meditations on First Philosophy"* (1641) paved the way for scientific thinking by arguing that doubt is the only thing one can really be certain of. This initial thought was followed by the birth of modern science, and in the following centuries, experiments and deduction - instead of superstition and dogmatism - have been used to understand and predict nature.

In the case of modern astrophysics, already common sense dictates doubt. The distance to most objects that are the subject of astrophysics exceeds our imagination. Theories about (inter-)stellar objects are solely built on the observation of light and other cosmic messenger particles that reach us - after having travelled for thousands or millions of years.

In order to gain further insights in the cosmos, astrophysical disciplines like very high energy (VHE-, ($E > 100\,\mathrm{GeV}$)) gamma-ray astronomy investigate electromagnetic radiation that is not visible to the human eye. These observations open a window to the **non-thermal universe**, i.e. to radiation from the most energetic processes in the cosmos.

However, highly energetic photons are absorbed in the atmosphere. This obstacle to their observation can be overcome by using satellite bound experiments (like the FERMI Gamma-ray Space Telescope that was launched in 2008) which reconstruct the photon's energy with a semi-conductor based calorimeter. However, in the last twenty years, a ground-based alternative in the form of **Imaging Atmospheric Cherenkov Telescopes** (IACTs) has emerged. These utilise the atmosphere as a calorimeter by observing the Cherenkov light of particle showers that were triggered by the absorption of highly energetic photons in the atmosphere (see chapter 2). They therefore have a significantly larger detection area than satellite-bound detectors ($\simeq 10^5\,\mathrm{m}^2$ compared to $\simeq 1\,\mathrm{m}^2$) and are able to observe photons of even higher energies, which are more rare than photons with lower energy.

The difficulty of this detection technique is that highly energetic photons have to be discriminated from a variety of other particles that impinge on the atmosphere every second. This particle flux of about 1000 particles per square metre per second (above energies of 1 GeV, ([1]) was first discovered by **Victor Hess** in the year 1912 [2]. Hess (who was awarded the Nobel prize in 1936) conducted balloon experiments in the higher layers of the atmosphere, from which he noticed that on board electroscopes discharged more rapidly with increasing altitude. This effect was attributed to highly energetic charged particles from outer space, which were called **cosmic rays**[1]. Their discovery triggered intensified research of energetic particles from space (culminating in the discoveries of particles like the positron, the kaon and the pion) which some decades later inspired the construction of the first earth-bound particle accelerators.

The cosmic ray riddle

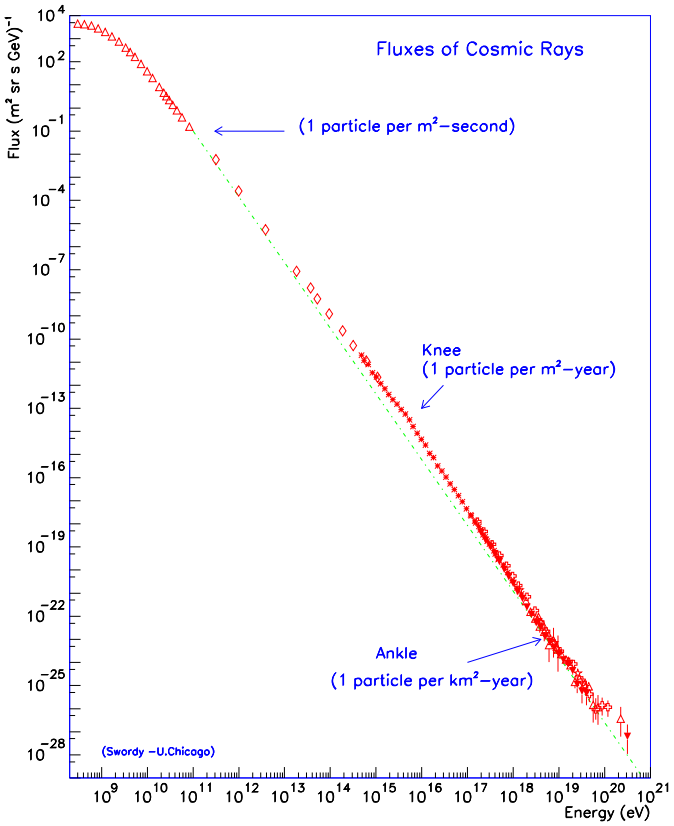

Fig. 1.1: Energy spectrum of cosmic rays. The red data points were collected by various experiments, the dashed green line corresponds to a power law with an averaged index and is drawn in order to visualize the actual spectrum's deviation from it (image taken from [3]).

Today, many aspects of the cosmic rays have been investigated and it has been found

[1] the term is a bit misleading since the particles arrive individually and not in beams of particles

that they consist mainly of protons ($\approx 85\%$) and α-particles ($\approx 11\%$), but also with contributions from heavier nuclei (1%), electrons, positrons (together 1.8%) and photons [4]. The energies of the particles cover ten orders of magnitude, ranging from 10^{10} eV up to 10^{20} eV. Their **energy spectrum** (Fig. 1.1) decreases steeply (i.e. there are many fewer particles of higher energy than there are of lower energies), obeying a power-law $\frac{\mathrm{dN}}{\mathrm{dE}} \propto E^{-\Gamma}$ with slightly varying index. The energy spectrum steepens a bit at the so called **"knee"** (from an index of $\Gamma = 2.7$ to $\Gamma = 3.1$) at around 10^{16} eV, but flattens again at the **"ankle"** (to $\Gamma = 2.7$) at approximately 10^{19} eV.

Despite the fact that cosmic rays have been investigated for almost one century, their exact origin is still contentiously debated. It is widely believed that cosmic rays with energies up to the knee are accelerated in the shock-waves of supernova explosions[2], however, a decisive proof of this hypothesis is still pending. Determining the **origin of the cosmic rays** is complicated by the fact that - due to Lorentz forces - charged particles are deflected in interstellar magnetic fields and therefore all directional information of the cosmic rays is lost when they reach earth.

VHE γ-rays

Photons, on the other hand, are not affected by magnetic fields and therefore the direction in which they are observed points back towards their emission region. VHE-photons are emitted in stellar regions where cosmic particles are accelerated to highest energies. Their detection with arrays of IACTs therefore allows to study cosmic accelerators like supernova remnants or pulsar wind nebulae. There are three known processes that can cause the emission of VHE γ-rays:

1. **Synchrotron emission / Bremsstrahlung**: charged particles that are accelerated in an external field emit photons. This mechanism is only relevant as a source of VHE-photons in case of very strong magnetic fields and electrons with very high energies (conditions that can e.g. be found close to the surface of a neutron star).

2. **Inverse Compton (IC)- Scattering**: low energy photons (e.g. from the cosmic microwave background) are up-scattered by populations of highly relativistic electrons or positrons via the inverse Compton-effect and are thereby obtain very high energies. The IC-component usually peaks in the VHE-range of the energy spectrum.

3. **Core-Core-Collisions**: if atomic nuclei (e.g. protons) are accelerated and collide with other nuclei (that e.g. drift through the interstellar medium), neutral pions can be created via the strong interaction. These pions subsequently decay into a pair of VHE-photons (see 2.1.1).

Each of these processes emits radiation that is characterized by a unique energy spectrum. IACTs allow the observer to reconstruct the spectra of cosmic sources in the very high en-

[2]For cosmic rays of more than 10^{18} eV, one suspects an extragalactic origin, mainly due to the fact that the gyro radius of particles with such high energies in the galactic magnetic fields exceeds the size of our galaxy [5].

ergy range. The most successful ground-based VHE γ-ray experiment is the High Energy Stereoscopic System (H.E.S.S.), which consists of four IACTs located in the Namibian desert. It started operation in 2003. To date, H.E.S.S. has discovered more than 50 VHE γ-ray sources within our galaxy [6] and various extragalactic VHE γ-ray emitters, e.g. active galactic nuclei (AGNs), Radio Galaxies and - quite recently - a Starburst Galaxy [7].

Solving the cosmic ray riddle by observing supernova remnants

One important result obtained from H.E.S.S. observations is a spatially resolved image of the supernova remnant RX J1713.7–3946 (see Fig. 1.2), in which excessive VHE γ-ray emission in the outer shell structure can be seen. By studying the energy spectrum of this radiation, one is able to draw conclusions about the particles that are responsible for the VHE γ-ray emission.

If mostly protons and other hadrons were accelerated to very high energies by the shock-wave of the supernova, the VHE γ-ray spectrum would be dominated by photons originating in the decay of neutral pions. Alternatively, if primarily electrons and positrons were accelerated to very high energies, one would expect a spectrum associated with the VHE γ-ray emission due to the IC-scattering of the accelerated leptons by the microwave background radiation.

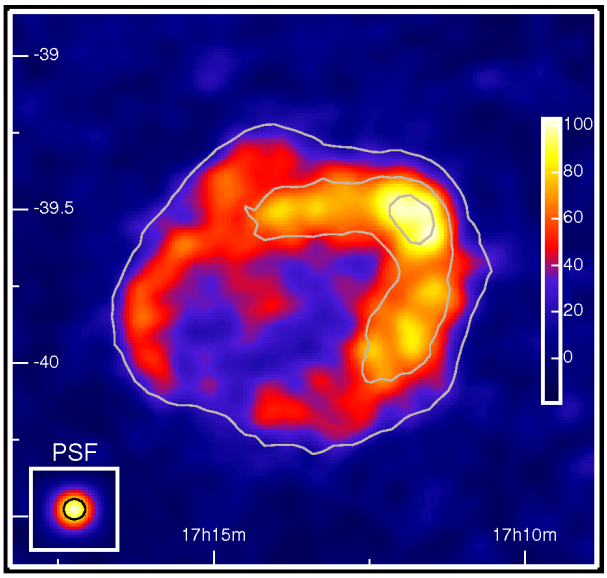

Fig. 1.2: Sky map showing VHE γ-ray excess events in the region of the extended supernova remnant RX J1713.7–3946 that was observed by H.E.S.S. in 2004 and 2005. The overlay in the lower left corner shows the point spread function, i.e. the size a point source would have in this sky map (image taken from [8]).

Consequently, the reconstruction of the VHE-range of the energy spectrum with IACTs could provide the missing clue for unraveling the origin of the cosmic rays. Unfortunately, the energy spectrum reconstructed for RX J1713.7–3946 based on the H.E.S.S. data (see Fig. 1.3) does not rule out the IC-model as a predominant emission mechanism, in par-

ticular because the exact shape of the expected spectra for both scenarios depends on additional parameters (e.g. the magnetic field and the effective ambient density). Nevertheless, the proton scenario seems to be favoured, which would suggest a direct connection between supernova explosions and cosmic rays.

Common to the spectra of all VHE γ-ray emitters is a steepening above a source-specific **cutoff energy**. The physical reason behind this is that cosmic accelerators can accelerate particles only up to a certain energy. In a leptonic scenario, particles with energies above the cutoff energy subsequently lose energy due to synchrotron radiation, with the maximum intensity being emitted at a frequency of $\nu_{\mathrm{synch}} \propto E^2$ [9]. Hence, by determining the cutoff energy, one is able to predict the shape of the synchrotron spectra, which can be reconstructed using X-ray astronomy experiments. With such a multi-wavelength analysis, further evidence regarding the acceleration scenario can be collected.

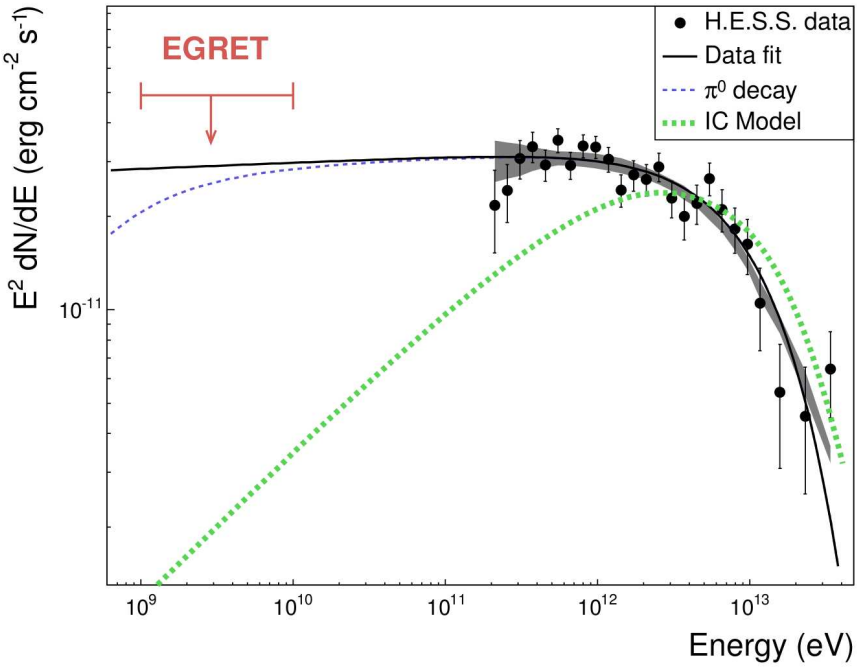

Fig. 1.3: H.E.S.S. data points for the supernova remnant RX J1713.7–3946 plotted in an energy flux diagram. The small dashed line (blue) describes the VHE γ-ray emission spectrum due to π^0-decay, whereas the broad dashed line (green) describes the expected distribution according to the leptonic IC-model. The upper limit obtained from EGRET measurements is plotted as a red arrow. The shaded grey band displays the systematic error that is inherent to the measurement (image taken from [10]).

Motivation for systematic tests of the energy reconstruction

As can be seen in the example of RX J1713.7–3946, an accurate reconstruction of the energy spectrum at low and high energies is essential for the discrimination between the leptonic and the hadronic scenario on the basis of H.E.S.S. data. Obviously an accurate energy reconstruction is also desired for other parts of the energy range.

Motivated by the need of an accurate energy estimation of the observed VHE γ-rays, this thesis investigates the present day energy reconstruction of H.E.S.S.. The objective is to check whether the accuracy of the event reconstruction has changed over the last five years. Therefore new systematical studies are presented. These consist of two parts: First, the energy reconstruction of the whole telescope array will be investigated and major systematical effects will be quantified (chapter 3); second, in chapter 4 it will be tested whether the responses of the individual telescopes have changed relative to each other, thereby introducing new systematical effects. Additionally, the time-wise evolution of differences between the telescopes will be evaluated.

In order to analyse the energy reconstruction of H.E.S.S., Monte Carlo simulations of VHE γ-rays are used to test the response of the telescope system. Furthermore, two bright VHE γ-ray sources (the Crab Nebula and the AGN PKS 2155–304), that were observed intensively and in regular intervals during the last five years, are analyzed in order to study the energy reconstruction of real air showers.

Before the systematical tests that were performed for this work are discussed, chapter 2 will give an introduction to the physics of air showers and to the H.E.S.S. experiment. A special focus of this chapter will rest on the explanation of the complex analysis chain that is required to infer the energy of VHE-photons from the Cherenkov-light of air showers.

Chapter 2

The H.E.S.S. Experiment

The **H**igh **E**nergy **S**tereoscopic **S**ystem (H.E.S.S.) is an array of four **Imaging Atmospheric Cherenkov Telescopes** (IACTs) located in Namibia. H.E.S.S. observes sources of highly energetic VHE γ-rays by detecting the Cherenkov light of particle showers that are triggered by the absorption of VHE γ-rays in the atmosphere. This chapter discusses

Fig. 2.1: The four IACTs on the H.E.S.S. site, that is located on the Goellschau farm in Namibia.

general properties of air showers in the atmosphere and gives insights into the detection of Cherenkov light with arrays of IACTs like H.E.S.S.. Furthermore, the general layout of the H.E.S.S. experiment is introduced, followed by a detailed description of the Hillas analysis technique, which is used to reconstruct the direction and the energy of the VHE γ-rays observed by the telescopes.

2.1 Detection of VHE γ-rays with Cherenkov telescopes

2.1.1 The physics of air showers

Ground-based Cherenkov telescopes use the atmosphere as a detection medium, i.e. they observe the deposition of the energy of highly energetic particles in the atmosphere.

Whenever a VHE γ-ray or a highly energetic cosmic ray particle hits the atmosphere and interacts with air-molecules, secondary particles are produced. The energy of these secondary particles is sufficient to produce further particles. Thereby a cascade of secondary particles - an **air shower** - is created, that descends towards earth. Depending on which particle triggered the air shower, one discriminates between electromagnetic and hadronic air showers.

Whereas electromagnetic air showers are primarily triggered by photons and electrons, hadronic showers result from the absorption of protons and heavier nuclei from the cosmic ray flux. Responsible for the development of electromagnetic air showers is the inter-

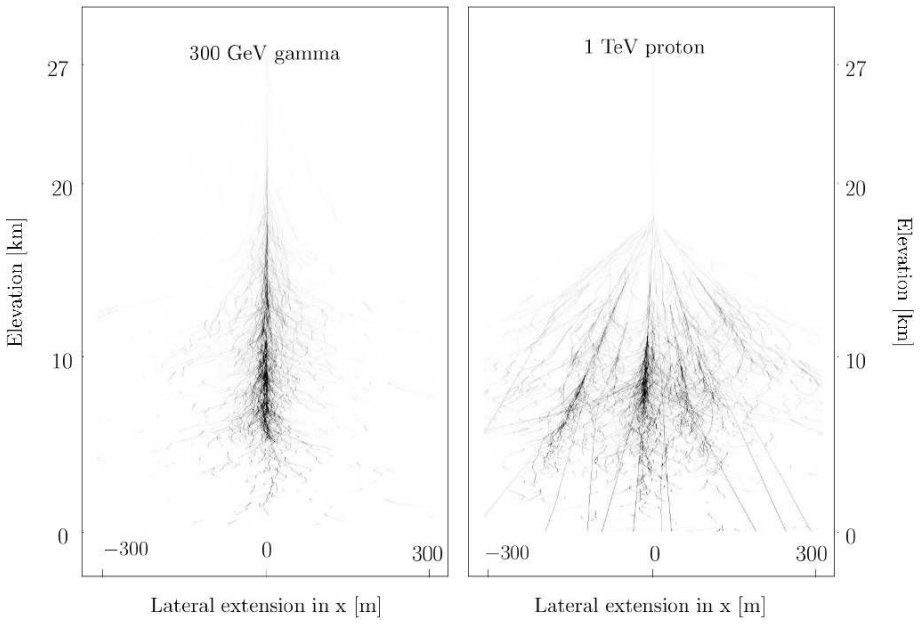

Fig. 2.2: Longitudinal shower development, i.e. particle trajectories for a simulated 300 GeV photon and a 1 TeV proton [11].

play of the processes of **Bremsstrahlung** and **pair production**: The interaction of the highly energetic primary particle with the Coulomb potential of an atmospheric nuclei produces an electron-positron pair. Both the electron and the positron retain a large fraction of the primary energy and continue their propagation through the atmosphere. In the Coulomb-field of other atmospheric nuclei these secondary particles lose energy and emit Bremsstrahlung. The Bremsstrahlung photons are again apt to produce additional electron-positron pairs, that again emit Bremsstrahlung. This interplay continues until the produced electrons primarily lose energy due to the ionisation of the ambient medium

instead of Bremsstrahlung, at which point the shower development abates. electromagnetic showers usually have a small lateral extend and develop symmetrical around the shower axis.

Hadronic air showers are in many respects similar to electromagnetic showers. However, the fact that hadrons are also subject to the strong interaction, results in a drastically different shower development. If a highly energetic proton encounters an atmospheric nuclei, the proton is scattered inelastically via the strong interaction, resulting in the production of mesons (pions and kaons) and additional nuclei (protons, neutrons). A part of these secondary hadrons are neutral pions that have a very short lifetime ($\approx 8 \times 10^{-17}$ seconds [12]) and decay almost immediately in two photons. The photons induce electromagnetic sub-showers that again develop according to the interplay of Bremsstrahlung and pair production. However, due to the inelastic nature of strong interactions, these have a bigger lateral momentum than primary electromagnetic showers, resulting in an overall larger lateral extend of hadron-induced air showers (see Fig. 2.2).

The differences in the development of electromagnetic and hadronic showers allow a discrimination between gamma-induced and nuclei-induced showers. Such a discrimination is especially important since even for the brightest VHE γ-ray sources, only about 0.1% of all observed air showers were induced by VHE γ-rays. The exact discrimination technique will be discussed in more detail when introducing the standard analysis of H.E.S.S. in section 2.3.4.

2.1.2 Cherenkov light of air showers

Whenever a particle moves through a medium with a velocity that exceeds the velocity of light in this medium, Cherenkov light is emitted. The velocity of light in a medium is $c_{\mathrm{n}} = \mathrm{c/n}$ with n being the refractive index of the medium and c the speed of light in vacuum.

This Cherenkov condition is fulfilled for the secondary particles of an air shower passing through the upper layers of the atmosphere. Hence, air showers can be observed by detecting the Cherenkov light that they emit. The Cherenkov-light is only emitted within a narrow cone around the direction of the shower, with an opening angle of:

$$\Theta_c = \frac{1}{\beta \cdot n} \tag{2.1}$$

where $\beta = \frac{v}{c}$, with v being the velocity of the shower particle and n the refractive index of the atmosphere. The diameter of the Cherenkov light pool at observation level is then

$$d_{\text{light-pool}} = h \cdot \tan\left(\Theta_c/2\right) \simeq h \cdot \Theta_c/2 \tag{2.2}$$

with h being the height of the **shower maximum**, i.e. the height above observation level at which the maximal intensity of the shower can be found. For a photon with $E = 300\,\mathrm{GeV}$, the shower maximum is located at $h \simeq 10\,\mathrm{km}$. The angle under which Cherenkov light is emitted in this case takes values in between 0.5° and 1.0°, which

translates to a light-pool diameter on the ground of $d_{\text{light pool}} \simeq 250\,\text{m}$. Θ_c depends on the height of the shower; due to the lower density of the ambient air, it increases with decreasing h (see [10], page 16). This results in a superimposition of the light cones that are emitted by the shower in different heights at observation level. Due to multi-scattering of the secondary particles, a diffuse component of the Cherenkov photons reaches the ground outside of the radius of the Cherenkov light-pool. A lateral distribution of the Cherenkov light on the ground (based on simulations) for a VHE γ-ray and for a proton can be found in Fig. 2.3.

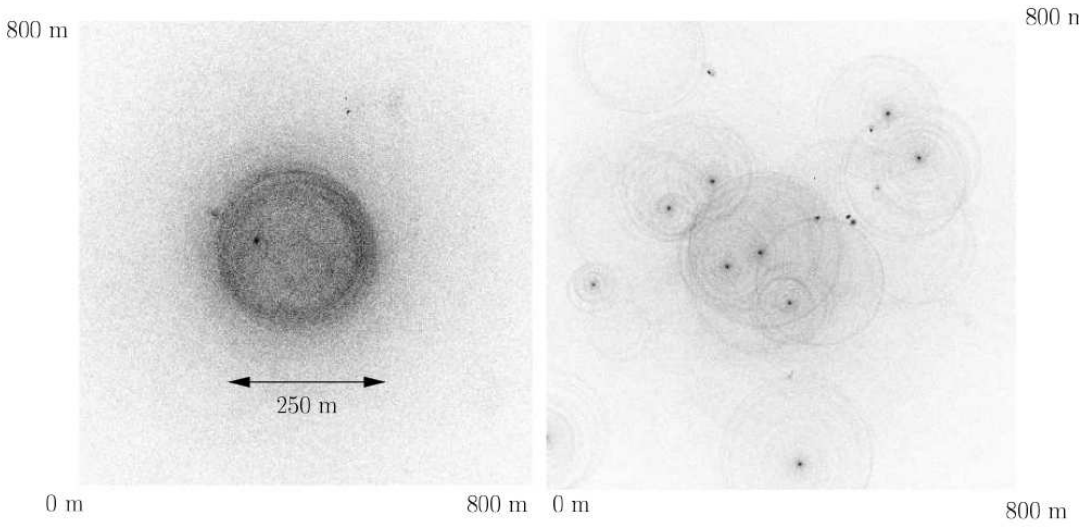

Fig. 2.3: Lateral Cherenkov light distribution of the shower from Fig. 2.2 ([11]).

2.1.3 Zenith angle and light-pool radius

With ground-based telescopes, most sources are not observed at zenith (i.e. directly above the telescopes), but at an angle of inclination towards the horizon. This **zenith angle** has two effects on the observation of air showers with IACTs:

1. In addition to the larger horizontal distance between shower and telescope, showers that are observed at large zenith angles reach their maximum intensity in greater height. This is the case because the shower maximum develops after the shower covered a certain distance in the atmosphere, which - given the horizontal propagation of the shower - results in a shorter expansion in vertical direction. Hence, the distance between the telescopes and the shower maximum in the atmosphere increases. On the one hand, this larger distance between the telescope array and the shower results in smaller images of the shower in the telescope-cameras, which reduces the accuracy of the shower reconstruction (see section 3). On the other hand, the Cherenkov light travels a longer way through the atmosphere and - due to the absorption effects in the medium - is fainter when reaching the telescope. Thus, when a source is observed under a large zenith angle, a VHE γ-ray must have a larger energy in order for its shower to be detected by the telescope array.

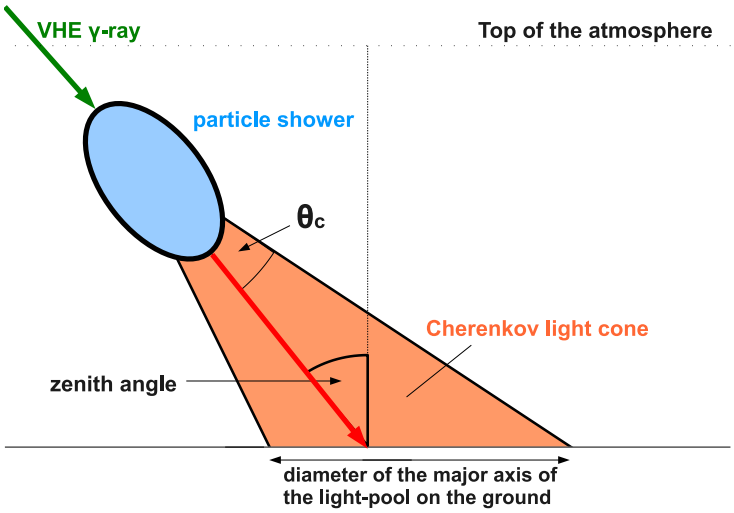

Fig. 2.4: Sketch illustrating the widening of the Cherenkov light-pool at ground level for observations under a large zenith angle. Note that in reality, the height of the shower above observation level is much larger than its lateral distance from the telescopes.

2. The Cherenkov light distribution on the ground is influenced by projection effects: due to the greater height of the shower, the Cherenkov light cone has widened when reaching the ground. In addition, the light-pool on the ground is stretched in one dimension due to observing under an angle (see Fig. 2.4).

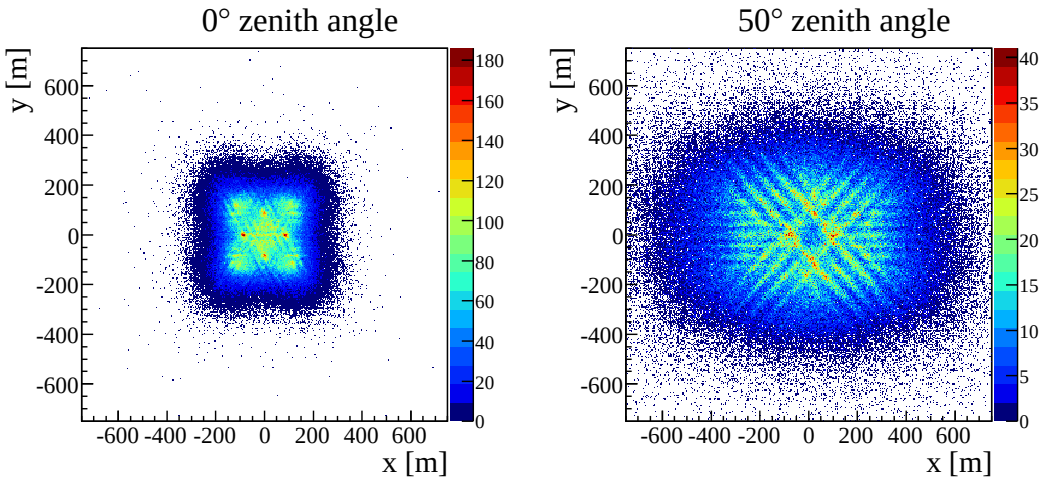

Fig. 2.5: Distribution of impact positions on the ground of simulated VHE γ-ray showers incident at 0° offset angle and 0° (*left*) and 50° zenith angle *right*, respectively. (0,0) corresponds to the center of the telescope array, whereas the bright dots at ±84 m coincide with the telescope locations. The zenith in the simulations is simulated in negative x-direction.

The distribution of the impact points of VHE γ-ray showers on the ground based on simulations for 0° and 50° zenith angle, respectively, can be found in Fig. 2.5. One can

clearly see that the impact points for observations at large zenith are scattered over a much larger area. As the zenith angle is simulated in negative x-direction, the distribution is stretched in x-direction, with $\approx 51\%$ of the impact points having positive x-values. Note that the diagonal structures in both plots (better discernible in the right plot) reflect the hexagonal shape of the camera pixels (see the discussion of the geometry reconstruction in 2.3.3).

The widening of the Cherenkov light-pool at observation level also becomes apparent in Fig. 2.6. Here, the mean image amplitude, i.e. the average number of photo electrons collected by an IACT, as a function of the perpendicular distance between the shower axis and the telescope is displayed for different energy bands.

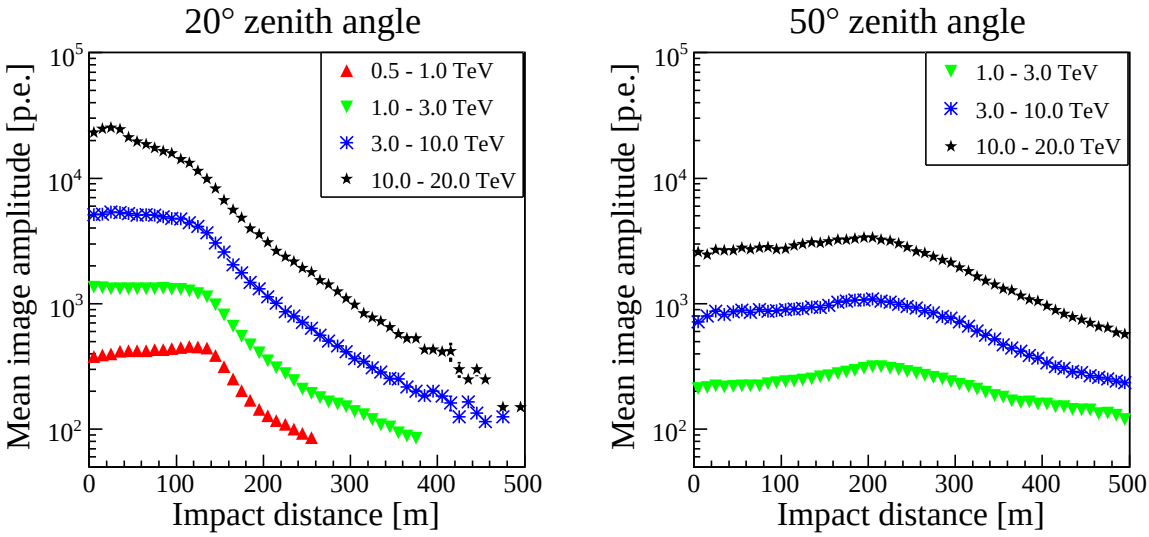

Fig. 2.6: The mean image amplitude, i.e. the average number of photo electrons collected by an IACT, in dependence of the impact distance for one telescope of H.E.S.S., displayed for different energy bands and simulated VHE γ-ray showers incident at 20° (*left*) and 50° zenith angle *right*.

For observations at 20° zenith angle, the mean image amplitude stays roughly constant for distances up to an edge in the plot at 130 m, from which on it decreases rapidly. This distance is just the ring radius of the central Cherenkov light-pool on the ground (visible in Fig. 2.3) and is called the *Cherenkov shoulder*. The decline in photo electrons for distances past the Cherenkov shoulder can be explained by the fact that outside of the central region of the Cherenkov light-pool, only (the fainter) Cherenkov light from multi-scattered secondary particles is detected.

For increasing energies, the amount of collected light naturally increases for a fixed distance between the shower axis and the telescope. Low energy showers only trigger the telescope system up to a certain distance, e.g. 250 m for showers with $500\,\mathrm{GeV} < E_\gamma < 1.0\,\mathrm{TeV}$.

For 50° zenith angle, a larger area is covered by the Cerenkov light-pool. Thus, the Cherenkov shoulder is shifted to larger distances, i.e. the number of collected photons is roughly constant up to ≈ 230 m. As will be seen in chapter 3.3, at such a zenith angle, the

energy reconstruction for photons with an energy of less than 1 TeV suffers from strong systematics. Therefore only energy bands above this threshold were included in the right hand plot in Fig. 2.6.

2.2 Experimental setup of H.E.S.S.

H.E.S.S. consists of four identical IACTs located in the Khomas Highland in Namibia, 100 km outside the capital Windhoek. At 1800 m altitude, the site provides optimal conditions for astronomical observations. One of the telescopes (CT3) has started operation in July 2002, with the construction of the other three telescopes being completed in December 2003. The full telescope array has been taking data since then.

2.2.1 The telescope array

The four telescopes are distributed on the corners of a square with 120 m side length, being oriented in a way that seen from the center of the square, there is one IACT in each point of the compass (i.e. the diagonals of the square are orientated in north-south and east-west direction). A picture of all four telescopes can be found in Fig. 2.1 whereas Fig. 2.7 shows one of the IACTs.

The layout of the telescope array represents a compromise: On the one hand, a large spacing between the telescopes is desirable, as the observation of air showers with two or more telescopes allows a three-dimensional reconstruction of the primary particle's direction. The stereoscopic observation additionally allows for a superior selection of cosmic ray events concerning the rejection of single muon events (see section 2.3.6) or background events triggered by the night sky, as these in general are not observed by two telescopes at the same time. Consequently, the larger the spacing between the telescopes, the higher the accuracy of the geometry reconstruction. Additionally, a large side length of the array also increases the total detection area of the array.

Fig. 2.7: One of the four Imaging Atmospheric Cherenkov Telescopes of H.E.S.S..

On the other hand, as one wants that showers are detected by two or more of the IACTs in the array, the maximal distance between telescopes is limited by the radius of the Cherenkov light-pool on the ground ($\simeq 120\,\mathrm{m}$, see Fig. 2.3). With 120 m in between telescopes, the Cherenkov light-pool of most detected showers covers two or more telescopes, while a stereoscopic geometry reconstruction is still possible.

2.2.2 Detection of Cherenkov light with H.E.S.S.

The Cherenkov light of air showers is very faint: for a primary photon with an energy of 1 TeV, only about 100 photons per m^2 reach the ground. The arrival time of the Cherenkov photons lie in a time frame of a few nanoseconds [13]. In order to detect these signals, each of the four H.E.S.S. telescopes consists of 382 mirror segments mounted on a hexagonal dish. Each segment has a diameter of 60 cm, giving each telescope a detection area of $107\,\mathrm{m}^2$. The dish to which the mirrors are attached is constructed such that it has a radius of curvature of 15 m which at the same time is also the focal length of the telescope.

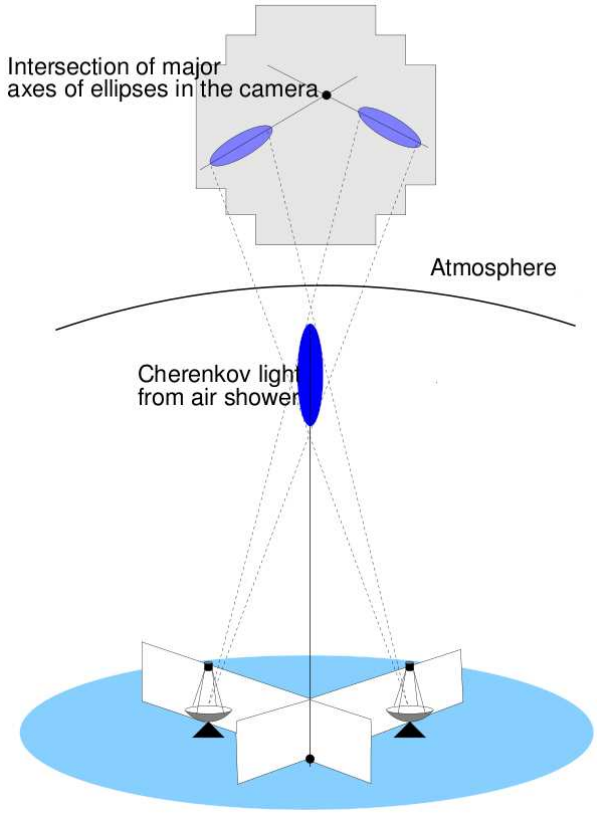

Fig. 2.8: The principle of the detection of Cherenkov light with IACTs like H.E.S.S.. As will be explained in section 2.3.3, the two camera images are intersected in the same coordinate system in order to reconstruct the direction of the shower (image taken from [14]).

The incident light is reflected and focused into a camera, which consists of 960 photo multipliers with a size of 0.16° each. Winston cones are installed in front of each photo

multiplier in order to focus light onto the active area of the multiplier. The camera has a total field of view of 5°. Each camera is connected to a central trigger unit that starts the camera readout, as soon as a shower is seen by two or more telescopes. The typical trigger rate for observations at zenith is $\simeq 200\,\mathrm{Hz}$. The telescope system is triggered by showers that were induced by primary particles with an Energy $> 100\,\mathrm{GeV}$. A sketch displaying the general detection principle and the projection of the shower image in the camera plane can be found in Fig. 2.8.

H.E.S.S. stores data in 28 minute long **runs**. The amount of collected data is often given in terms of **live time**, which is the run duration subtracted by the dead time of the detectors. Observations are carried out in moon-less nights during good weather conditions. During a run, the telescopes track the observation position in the sky, which is usually 0.5° - 0.7° away from the target position, i.e. the direction of expected VHE γ-ray emission.

This small angular distance between the pointing direction and the source direction is called **offset angle**. Usual offset angles are 0.5° - 0.7°, whereas the direction of the offset on the sky is subsequently shifted with each run. This technique is called **wobbling** and it allows to collect comparable data on the background regions surrounding the respective VHE γ-ray source, which becomes important when estimating the fraction of background events in the source region. This is used for the spectral reconstruction and is discussed in detail in [15].

2.3 The H.E.S.S. Standard Analysis

In the following, the H.E.S.S. Standard Analysis will be introduced and explained. In the run of the analysis, ellipse-like camera images are first parametrised using an approach introduced by Hillas. Then the direction and the energy of the primary particle are determined based on these parameters.

2.3.1 Run selection and image cleaning

However, before camera images are parametrised, suitable runs are selected and the remaining camera images are cleaned. Runs are discarded if they were taken under bad weather conditions or if eventual hardware failures occurred. Then, the camera images of the remaining runs are calibrated, i.e. differences resulting from varying signal amplification and sensitivity of the different pixels in the camera are corrected.

When Cherenkov photons are recorded by the camera, also photons from the night sky background are detected. These can be removed by selecting pixels that have registered at least 5 photo electrons and have a neighbouring pixel with 10 p.e. or more and vice versa. Pixels that do not fulfil these conditions are no longer used in the analysis. A detailed description of the image calibration can be found in [16].

2.3.2 Hillas parametrisation

With the cleaned image, a parametrization of the intensity distribution in the camera can be undertaken. Camera images of gamma-induced air showers have a longitudinal stretched shape (see Fig. 2.9) and can in first order be approximated by an ellipse. The image can be parametrised using the Hillas method [17] with the following parameters:

- **Width** and **length**, i.e. the minor (respectively the major) axis of the image.
- the **size**, i.e. the number of photo electrons in the cleaned image.
- the **center of gravity** (COG), i.e. the position of the center of the ellipse in the camera.
- θ, i.e. the orientation of the shower in the camera plane.

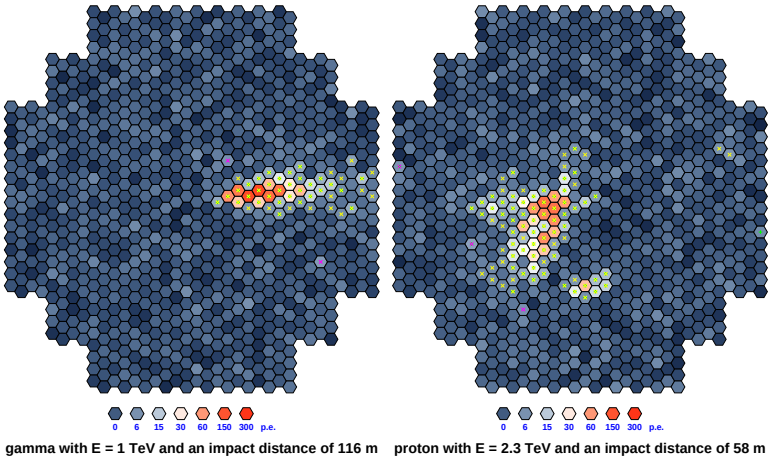

Fig. 2.9: Camera images of air showers induced by a photon with 1 TeV (*left*) and a simulated proton with 2.3 TeV (*right*).

These Hillas parameters (except the size) are visualized in Fig. 2.10.

The geometry-based parameters, i.e. width, length, COG and image orientation of two or more telescopes are used for the reconstruction of the shower direction and the intersection point of its axis with the ground level. This geometry reconstruction is discussed in section 2.3.3. The size, i.e. the amount of light collected by a telescope, for a fixed zenith- and offset-angle is proportional to the energy of the primary particle. Thus, together with the information obtained from the geometry reconstruction, it can be used to obtain a seperate energy estimate from each of the telescopes. The estimates of the different telescopes are then averaged to determine the energy estimate of the whole array. This is discussed in section 2.3.5.

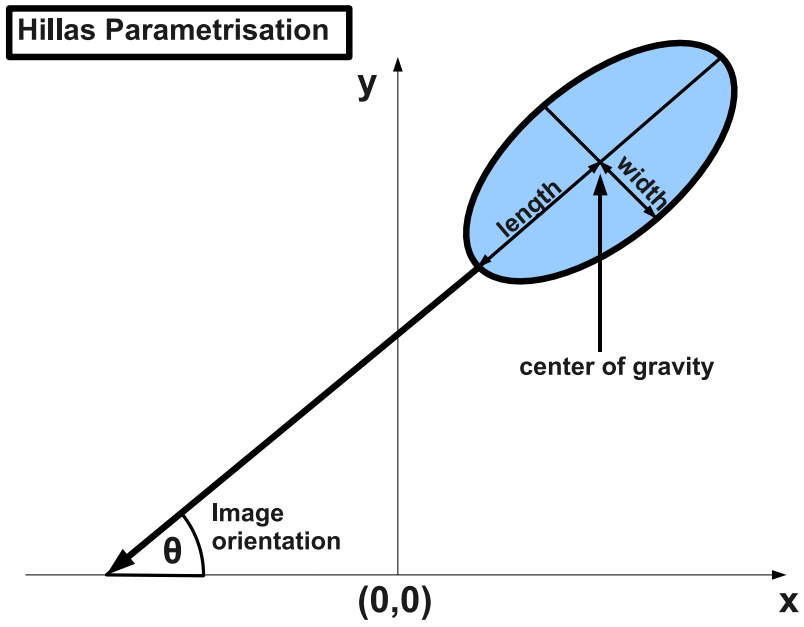

Fig. 2.10: Hillas parameters of an ellipse, describing the Cherenkov light distribution of a shower image in the camera.

Preselection of images

However, prior to the geometry reconstruction of the shower, suitable shower images for this reconstruction are selected. Therefore two **preselection** cuts based on the Hillas parameters of the individual images in the camera are applied:

1. A cut on the size, which excludes faint shower images for which only a bad shower reconstruction would be possible.
2. A cut on the local distance, i.e. the distance of the COG from the center of the camera in metres, is applied in order to discard images in which a part of the shower image lies outside of the camera.

The geometry of the shower is only reconstructed for those shower images that pass the preselection cuts. A camera image is not used in the further analysis if its size is < 80 p.e. (for standard cuts, see table 2.1), and its local distance < 0.525 m. Other cuts are applied after the geometry has been reconstructed. These **postselection** cuts are used to discriminate gamma- from hadron-induced showers and are discussed in section 2.3.4.

2.3.3 Geometry reconstruction

The stereoscopic approach, i.e. the fact that images of showers are only taken when at least two telescopes have seen the shower, allows to determine both the incident direction

of the primary particle and the **core position**, i.e. the point where the shower would have hit the ground, with high accuracy.

In order to reconstruct the incident shower direction, one defines the **image axis** as a line along the major axis of the Hillas ellipse [18]. The image axis then points towards the source direction in the nominal system.[1] For example, if the telescope points directly at the source, the image axis will go through the center of the camera. In order to get an averaged estimate of the **shower direction**, one intersects the image axes of the telescopes pairwise[2] in a common coordinate system and thereby obtains one estimate for the shower direction for each telescope pair (see Fig. 2.8). Before these intersection points are averaged, they are weighted according to the following criteria:

- Intersection points obtained by telescope pairs with camera images with large size and a pronounced longitudinal extend of the ellipse receive a large weight.
- The intersection points are also weighted with the sine of the angle in between two image axes, the **stereo angle** (see appendix A), mirroring the fact that telescope pairs with large stereo angles provide a more accurate estimation of the shower direction.

The weighted average of all intersection points then yields the incident direction of the shower. The core position is determined by intersecting the image axes in the array-wide ground-(coordinate) system instead of the nominal system.[3] The distance of one of the telescopes to the core position is called the **impact distance**.

2.3.4 Gamma/hadron separation

The Hillas parameters also allow a discrimination between gamma- and hadron-induced showers. As was explained in section 2.1, non-gamma cosmic ray events create showers with a large lateral extension in comparison to VHE γ-ray photons that trigger longitudinally stretched particle cascades. By applying cuts on the Hillas parameters that describe the image shape, one is thus able to suppress the vast majority of cosmic-ray background events.

In order to obtain parameters which are independent of the zenith angle and the offset with which an event was observed, one introduces the scaled width (SCW) and the scaled length (SCL) for each event and telescope. The scaled width (length) of telescope i is defined as the deviation of the width (length) from its expected value (that was obtained using Monte Carlo γ-ray simulations[4]) in units of standard deviations:

[1] The nominal system is the coordinate system in which the four camera images are superimposed.

[2] For the four telescopes of H.E.S.S. one gets six intersection points if all telescopes have detected the shower.

[3] For long shower images, the hexagonal shape of the camera pixels results in a preference of certain shower directions, which translates to the preference of certain core-distance values. This becomes apparent when investigating the simulated core distance distribution in Fig. 2.5.

[4] In which VHE γ-ray events are simulated and the length and width-values for each telescope - according to the respective size and the distance between the shower impact point and the telescope - are filled into lookup tables.

$$\mathrm{SCW}_i = \frac{\mathrm{Width}_i - < \mathrm{Width}_i^{\mathrm{MC}} >}{\sigma_i} \tag{2.3}$$

where $< \mathrm{Width}_i^{\mathrm{MC}} >$ is the expected width of the shower image, Width_i the width obtained from the Hillas parametrisation and σ_i the spread of the expected value.

In order to get a measure for the average scaled width of all telescopes, one calculates the **mean scaled width** (MSCW) of the shower:

$$\mathrm{MSCW} = \frac{\sum_i^{\mathrm{N}_{tel}} (\mathrm{SCW}_i \cdot \omega_i)}{\sum_i^{\mathrm{N}_{tel}} \omega_i} \tag{2.4}$$

where $\omega_i = \frac{<\mathrm{Width}_i^{\mathrm{MC}}>^2}{\sigma_i^2}$ is a weighting factor. The mean scaled length (MSCL) is defined in an analog way.

The distribution of these two quantities for simulated VHE γ-rays and protons as well as observational Off data[5] can be found in Fig. 2.11. The apparent difference between the distributions of simulated protons and Off-data can be explained by the abundance of heavier nuclei in the latter data set, which increase the lateral spread of momentum (see 2.1.1) and therefore lead to an overall larger MSCW.

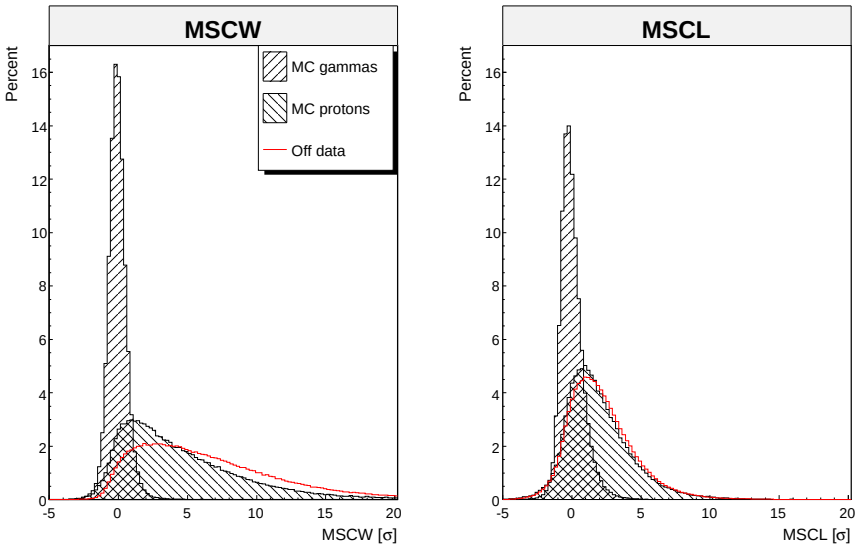

Fig. 2.11: Mean Scaled Width (*left*) and Mean Scaled Length (*right*) for VHE γ-ray Monte Carlo simulations in comparison to simulated protons and Off-data. By selecting only events with MSCW < 0.9 (standard cuts), one is able to exclude the majority of the background events. (image taken from [19])

All events that pass the preselection are subject to the **postselection**, in the course of which the MSCW and MSCL of each shower is calculated. Only events that pass

[5] Off data are obtained from observations in regions where no VHE γ-ray source is expected and just consists of hadronic cosmic-ray events.

cuts on these two quantities remain in the analysis. In addition, a cut on θ^2, i.e. the square of the angular distance between the source direction and the reconstructed shower direction can be used for the analysis of point sources. In this case, events are only used for the reconstruction of the spectrum if they are detected within a predefined circular region around the VHE γ-ray source. Because of the isotropy of the cosmic ray signals, one thereby dramatically reduces the amount of background events in the analysis, particularly for the observation of point sources. Values for the different preselection- and

config.	MSCW min	MSCW max	MSCL min	MSCL max	Size min[p.e.]	θ^2
loose	-2.0	1.2	-2.0	2.0	40	0.04
standard	-2.0	0.9	-2.0	2.0	80	0.0125
hard	-2.0	0.7	-2.0	2.0	200	0.01

Tab. 2.1: Values of the different cut parameters for the three cut configurations (loose, standard and hard) in the H.E.S.S. standard analysis.

postselection-cuts are chosen according to three configurations that were optimized for different source types. "Loose" cuts are optimised for a strong source with a similar intensity as the Crab Nebula and a hard spectra (index 2.6), whereas the "standard" configuration obtains a maximal significance [20] for a point source with spectral index of 2.6 and a flux of $\approx 10\%$ of the Crab Nebula. The "hard" configuration obtains best results for faint point sources ($\approx 1\%$ Crab) with a spectral index of 2.0.

The values for the cuts on the specific parameters discussed above can be found in table 2.1.

2.3.5 Energy reconstruction

All shower images that pass the preselection cuts are used to estimate the energy of the primary particle. The energy estimate is obtained by comparing the size and the reconstructed geometry of a shower image with the results of Monte Carlo simulations.

These simulations consist of two steps: At first, air showers induced by VHE γ-rays with different energies are simulated for different zenith- and offset-angles. Then, the response of the telescope array to these air showers is simulated and the reconstructed size and impact distance for each of the telescopes is filled in separate tables that link these two parameters to the simulated energy of the VHE γ-ray. These **lookup tables** (see Fig. 2.12) are produced for various zenith- and offset-angle combinations of the simulated VHE γ-rays, since the reconstruction of the impact distance (i.e. the geometry) strongly depends on these parameters.[6] The comparison of the size and the impact distance obtained by the reconstruction of the real shower with the corresponding entry in the energy lookup tables, allows to reconstruct the energy of the VHE γ-ray that induced the observed particle shower. In order to select the lookup table that resembles the

[6]Lookup tables are also produced for the RMS spread of the energies in each size and impact distance bin. These are used to estimate the error for a specific reconstructed energy.

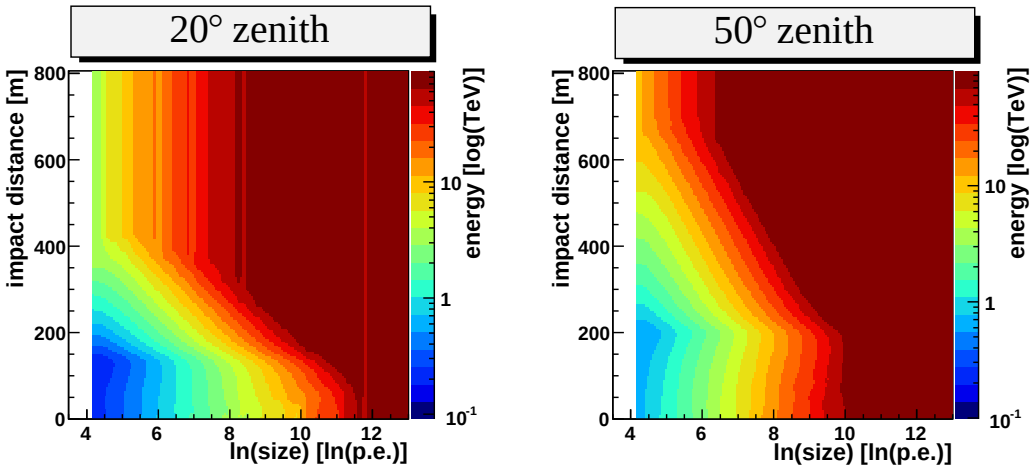

Fig. 2.12: Energy lookup tables simulated at 0.5° offset, and 20° zenith (*left*) and 50° zenith (*right*), respectively.

observational conditions best, both the offset- and zenith-angle of the observation are interpolated to the closest respective value for which lookup tables exist.

During the last years, energy lookup tables were produced several times. Each time, the telescope system was simulated with different properties, taking into account the change of the responses of the various telescopes with time. In this work, lookup tables based on two sets of Monte Carlo simulations are used:

1. **Phase1** simulations were produced shortly after the complete array started observation. To take into account that CT3 was already running for one and a half years and its mirrors and Winston cones had already degraded significantly, it is only simulated with a reduced response of 92%, whereas the other three telescopes are attributed 100% optical efficiency (see section 2.3.6).

2. **Phase1b** simulations were performed one year later when the whole array had degraded substantially and it was measured that all telescopes have the same (reduced) optical efficiency of 70%.

	CT1	**CT2**	**CT3**	**CT4**
Phase1	100%	100%	92%	100%
Phase1b	70%	70%	70%	70%

Tab. 2.2: Simulated responses of the different telescopes in Monte Carlo simulations from Phase1 and Phase1b.

When reconstructing the energy with the H.E.S.S. analysis software, a specific **configuration** is chosen, which uses either the energy lookups based on phase1 or phase1b simulations. In this work, predominantly the "std south 1b" configuration is used, that uses energy lookup tables from phase1b simulations of the southern hemisphere together with standard cuts for the event selection.

Finally, after obtaining the energy estimate of each telescope from the respective lookup tables, the energy estimates of the N_{tel} telescopes that passed the preselection cuts are averaged to get the mean energy of the event:

$$E_{1,2,3,4} = \sum_{i=1}^{N_{tel}} \frac{E_i}{\sigma_i^2} \tag{2.5}$$

where E_i is the reconstructed energy of telescope i, σ the error of the energy (whose square is used as a weighting factor).

The optical efficiencies attributed to the different telescopes in the simulations (summarized in table 2.2) are obviously only a rough guess of the actual optical efficiencies of the system. However, it is possible to estimate the optical efficiencies of the individual telescopes by observing muon events. When observing VHE γ-ray sources, the energy estimate of each telescope is accordingly corrected using the estimate of the optical efficiency obtained from the **muon correction**. This technique is discussed in the following.

2.3.6 Muon correction

H.E.S.S. investigates air showers by converting the N_γ Cherenkov photons emitted by the shower to $N_{p.e.}$ photo electrons. It is crucial to know what the ratio of these parameters, i.e. the optical efficiency $\epsilon = \frac{N_{p.e.}}{N_\gamma}$ is. There are a number of effects that influence the conversion of Cherenkov photons emitted by the extensive air shower to photo electrons measured by the camera. Some of these effects with estimates of their importance are[7]:

- The camera casing and the telescope arms shade a fraction of the mirrors, thereby reducing the amount of photons in the air shower that reach the camera by 11% [21].
- The reflectivity of the mirrors for Cherenkov light with wave lengths of $\lambda \simeq 300\,\text{nm}$ in 2004 was of the order of 75% and has since then decreased. In the case of H.E.S.S., this decrease is mainly caused by the dry and hot environment the site is located in [22].
- The Winston cones that are used to focus the incoming photons onto the respective camera pixels transmit only about 75% of the incoming light [23]. Again, the reflectivity worsens with increasing age of the Winston cones.
- The quantum efficiency of the photo multipliers amounts to 20% for a wave length of $\lambda \simeq 300\,\text{nm}$, but varies strongly with λ and also decreases significantly over time [24].

Since three of these four factors change with time, it is important to monitor the optical efficiency of the telescopes on a regular basis. This is done using the muon-correction technique, that is discussed in detail in [25].

[7] The following percentage values were obtained by simulations that were performed prior to the completion of H.E.S.S..

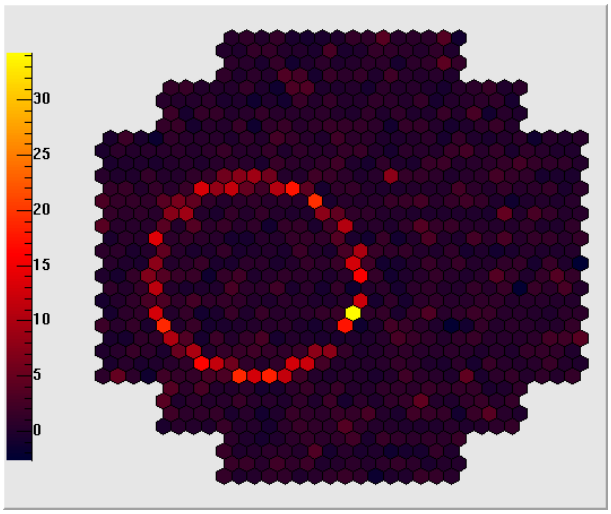

Fig. 2.13: Ring-like image in the camera of a muon that directly impinged on one of the mirrors. Note that this image was not cleaned, which explains the image noise in most of the pixels.

The technique uses the fact that hadron-induced air showers (see 2.1.1) include many muons that mostly originate from the decay of charged pions and kaons according to:

$$\begin{aligned} \pi^{\pm} &\longrightarrow \mu^{\pm} + \nu_{\mu}(\overline{\nu}_{\mu}) \qquad (\approx 100\%) \\ K^{\pm} &\longrightarrow \mu^{\pm} + \nu_{\mu}(\overline{\nu}_{\mu}) \qquad (\approx 63.5\%) \end{aligned}$$

Muons are not subject to the strong interaction and mostly lose energy due to ionisation of the atoms and molecules in the atmosphere. Compared to electrons, their larger mass makes them minimally ionising. They therefore penetrate deeply into the atmosphere and reach the surface. Due to the high energy of muons in cosmic ray-induced showers, they emit a significant amount of Cherenkov light.

Compared to air showers, the opening angle of the Cherenkov emission is smaller, and the detected light is emitted much closer to the telescope, which results in a much smaller area being illuminated by the Cherenkov light of the muon. Therefore muon events are mostly only observed by one telescope. For array systems with multiplicity trigger like H.E.S.S., this light is the major background component for a single IACT. Indeed, muon images are only taken "by accident", i.e. the telescope system is triggered by a background event and in one of the cameras a muon is detected, discernible by a ring-like image (see Fig. 2.13).

Since the opening angle of the Cherenkov cone depends on the energy of the muon, the geometry of the muon-ring in the camera allows to estimate the number of Cherenkov photons that have arrived in the camera. By comparing this number with $\mathbf{N}_{p.e.}$, one is able to obtain an estimate for the optical efficiency of the telescope. Based on this value, a muon correction factor for the reconstructed energy of the telescope is calculated and applied to the initially reconstructed energy of this telescope.

However, there are no regular cross checks of the effectiveness of the muon correction, which given its importance, leaves room for doubt regarding the accuracy of the overall energy reconstruction, especially since there are a number of effects that are not taken into account by the muon correction (e.g. fluctuations in the atmospheric density). The methods to compare the different telescope responses that are presented in chapter 4 allow to investigate the effectiveness of the muon correction. Before this, in chapter 3, general systematics in the energy reconstruction of H.E.S.S. are investigated.

Chapter 3

Systematics of the Energy Reconstruction

In the last chapter it was explained how the energy reconstruction of the H.E.S.S. experiment works. It was shown how the images of Cherenkov showers in the different telescopes are parametrised using the Hillas approach and how, based on these parameters, the shower geometry and the energy of the primary particle can be reconstructed.

This chapter focuses on the *known* systematics in this reconstruction chain, whereas in the next chapter possible yet *unknown* systematics stemming from the differences in the telescope responses will be discussed.

The major causes responsible for the inaccuracy in the energy reconstruction discussed in this chapter will be investigated by testing the system with two sets of Monte Carlo simulations, that were simulated with 0.5° offset angle and a zenith angle of 20° and 50°, respectively.[1] In order to simulate the response of the telescope system with properties similar to those of present day H.E.S.S., phase1b simulations were used, in which a reduced optical efficiency is attributed to the individual telescopes (see section 2.3.5). Furthermore, the VHE γ-ray spectrum is simulated with a soft spectral index of $\Gamma = -2.0$.

First, the accuracy of the geometry reconstruction is tested by evaluating the deviation of the reconstructed core position from the simulated one. Such uncertainties propagate to an error in the energy reconstruction, which will be evaluated by comparing the simulated event energy to the energy that was reconstructed by the telescope system. Based on the scatter of the reconstructed energies around the simulated energy, an estimate for the overall energy resolution of H.E.S.S. can be given. In chapter 4, this estimate will be compared to the systematic errors obtained by pairwise comparisons of telescopes.

Apart from explaining the overall energy systematics, this chapter focuses on the effect of the **multiplicity**, i.e. the number of telescopes that are used for the reconstruction of the shower, on the estimation of core position and energy. This is important since not all of the H.E.S.S. data is reconstructed using all four telescopes (see section 2.3.4). In

[1] 20° and 50° zenith angle were specifically chosen since the VHE γ-ray sources PKS 2155–304 and the Crab Nebula that will be used for the intercalibration in the following chapter, were observed under comparable zenith angles.

order to investigate the systematics when reconstructing events with only two or three telescopes, the studies regarding the geometry and energy reconstruction in the following sections will be carried out separately for events with different multiplicities.[2]

3.1 Multiplicity distribution

Before the systematics of the energy reconstruction for different multiplicities will be estimated, one is interested in how relevant events with a specific multiplicity are at different energies and for different core distances.

One is also interested in how the respective distributions differ regarding the post-trigger and the post-selection multiplicity of events, which is caused by the cuts of the preselection (see section 2.3.2). On the one hand, even though all four telescopes are located within the Cherenkov light-pool on the ground, the number of detected photo electrons in one or two telescopes may not be high enough to pass the size cut. This happens primarily for showers with lower energies. At higher energies, all telescopes register enough Cherenkov light even if the respective shower's core position is located far outside of the array. However, in this case the telescope(s) on the opposite side of the array detect a shower image whose center of gravity is located at the edge of the camera. These images are frequently discarded due to the local distance cut (see section 2.3.4).

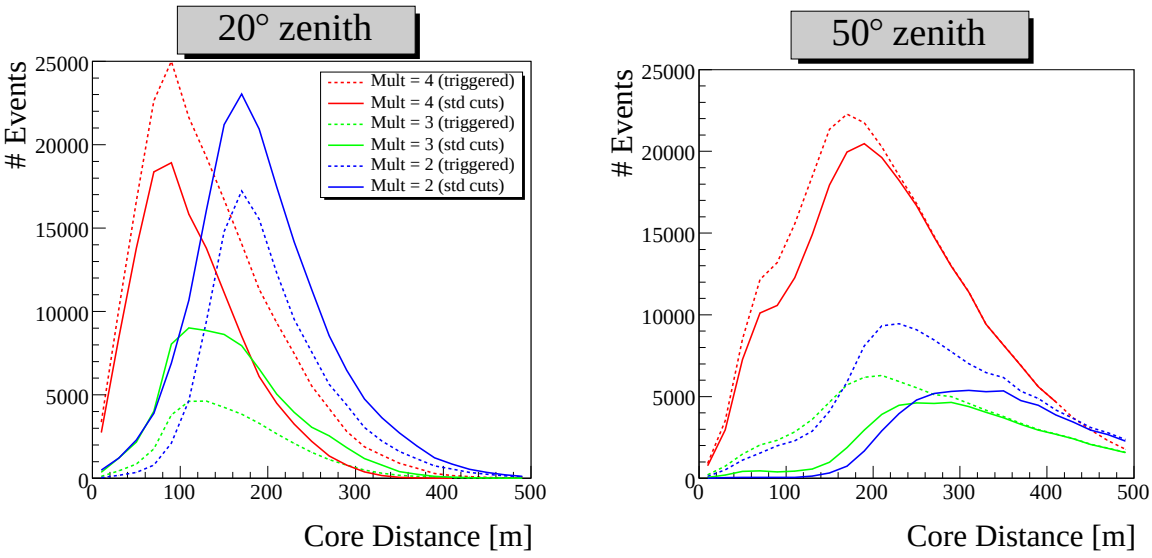

Fig. 3.1: Distribution of multiplicities as a function of the core distance. The same data sets as in 3.2 were used. Events from the full energy range are included in the distributions.

The discrepancy between the event group involving post-selection multiplicities and the

[2]When investigating multiplicities, it is necessary to distinguish between the number of telescopes that detected the shower and the number of telescopes in which the shower image passed the applied cuts and was actually reconstructed. A significant fraction of events e.g. is detected by four telescopes but only passes preselection cuts in two or three of the telescopes. 'Multiplicity' in the following refers to the number of telescopes in which an event passed the applied cuts.

events with post-trigger multiplicity can be seen in Figs. 3.2 and 3.1, that display the multiplicity distribution for different core distances and energies, respectively.

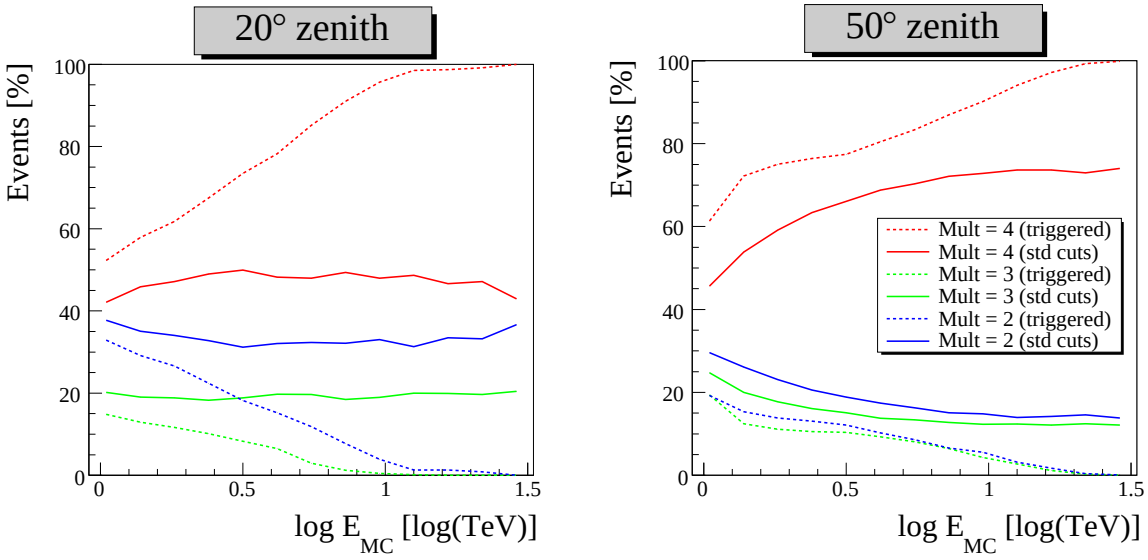

Fig. 3.2: Distribution of multiplicities for different energies, for two different Monte Carlo simulations with 20° (*left*) and 50° zenith angle (*right*), respectively. The dashed lines refer to the case where the respective telescopes have triggered, whereas the continuous lines show those events which pass standard cuts.

Regarding the multiplicity distribution in dependence of the core distance, one sees that at 20° zenith angle, events with small core distances, i.e. showers whose impact point lies within the array, are mostly four-telescope-events, whereas for core distances $> 120\,\mathrm{m}$ the majority of events have multiplicity two. For 50° zenith angle, the majority of the events for all core distances are four-telescope-events. This mirrors the fact that the Cherenkov light-pool on the ground widens for large zenith angles (see Fig. 2.4), making it less probable that one telescope is outside of the area illuminated by the Cherenkov light cone. Since the number of Cherenkov photons that is emitted in this cone increases with the energy of the primary particle, the fraction of four-telescope-events increases with increasing energy.

3.2 Core resolution

As was discussed in section 2.3.3, the event reconstruction relies on the stereoscopic approach, i.e. the fact that showers are registered and reconstructed by the different telescopes independently. For N telescopes that registered the shower, $N(N-1)/2$ estimates for the core position can be derived. Consequently, if only two or three telescopes are used to reconstruct an event, the core position estimate will be less accurate than for events where all four telescopes are used for the reconstruction. In the following it will be investigated how good the **core resolution** is, i.e. the deviation of the reconstructed core position from the simulated core position of the shower, for different multiplicities and varying zenith angles. The **error on the core reconstruction** is defined as:

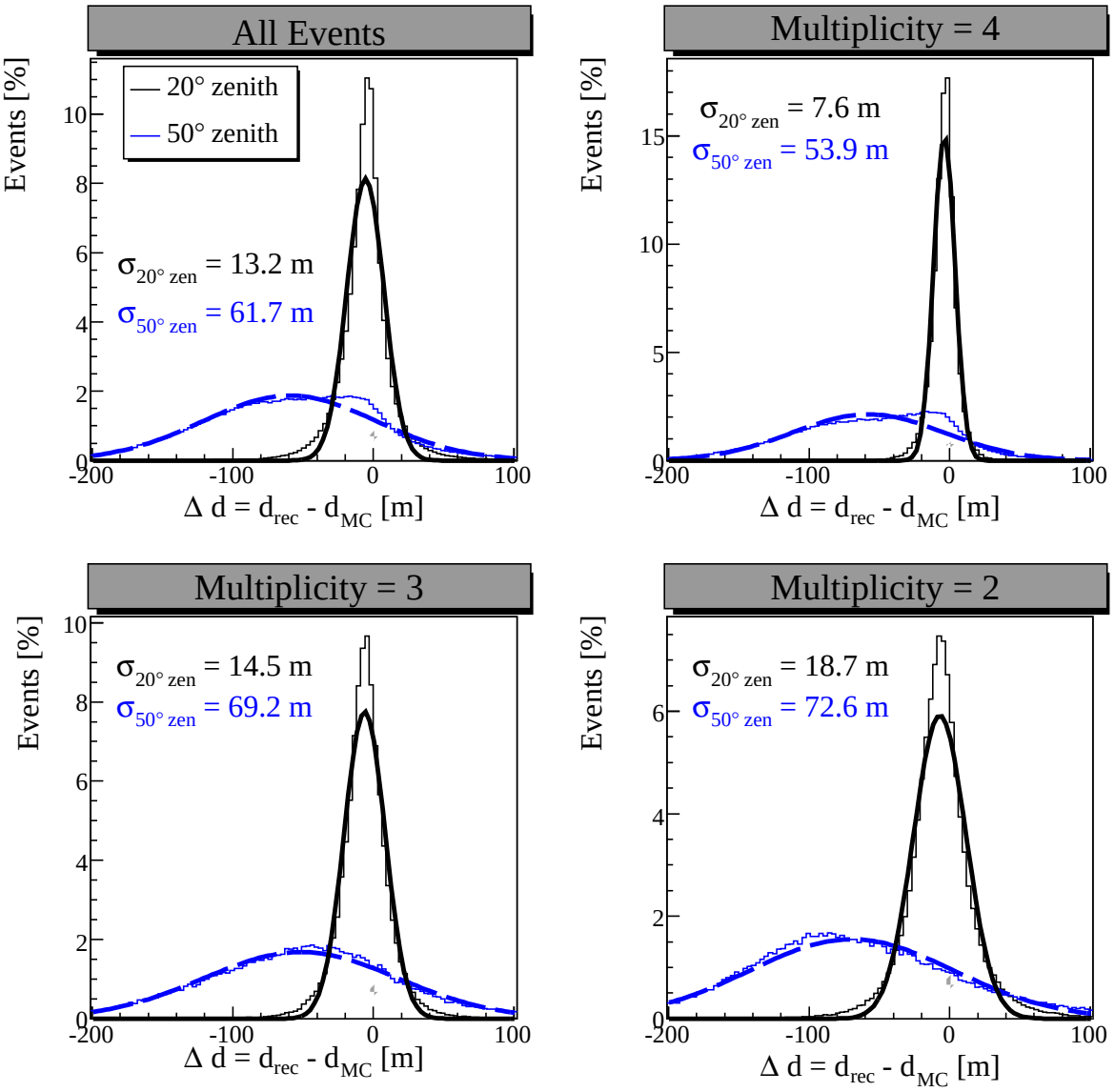

Fig. 3.3: Core resolution distributions with Gauss fit for Monte Carlo simulations with 20° zenith (black) and 50° zenith (blue). Sigma denotes the standard deviation of the Gaussian that was fitted to the respective distribution. Note that the number of entries in each bin was scaled with the total number of entries in the histogram.

$$\Delta d = d_{\mathrm{rec}} - d_{\mathrm{MC}} \tag{3.1}$$

where d_{rec} is the reconstructed core distance and d_{MC} is the distance to the true core position given by the Monte Carlo simulations. Fig. 3.3 shows the core resolution for different multiplicities and 20° and 50° zenith angle, respectively. A Gaussian fitted to the respective distributions describes the distributions reasonably well. The σ of the Gaussian was taken as a measure for the average core resolution. The respective values for different multiplicities are summarized in table 3.1.

At 20° zenith angle (for which the average reconstructed core distance in the used data set is $\simeq 163\,\mathrm{m}$), the core resolution for all events combined amounts to $\Delta d \simeq 13\,\mathrm{m}$. For two-telescope-events, the core resolutions worsens to $\Delta d \simeq 19\,\mathrm{m}$, reflecting the fact that only two image axes are intersected. Additionally, as discussed above, these events show large core distances for which a small inaccuracy in the stereo angle introduces a large inaccuracy in the core distance estimation.

zenith angle	**all events [m]**	**Mult=4 [m]**	**Mult=3 [m]**	**Mult=2 [m]**
20° zen	13.20 ± 0.02	7.58 ± 0.02	14.53 ± 0.06	18.70 ± 0.05
50° zen	61.70 ± 0.08	53.85 ± 0.08	69.24 ± 0.20	72.59 ± 0.19

Tab. 3.1: Values for the average core resolution, i.e. RMS-values of the Gaussians of the core error distributions (see Fig. 3.3).

For events that are observed at 50° zenith angle, the core resolution worsens significantly to $\Delta d \simeq 61\,\mathrm{m}$ for all events combined, whereas the average reconstructed core distance of this data set is $\simeq 254\,\mathrm{m}$. The worsening of the core resolution can be explained by the larger distance between the shower maximum in the atmosphere and the telescope array, which leads to smaller images in the camera and therefore to an overall worsening of the geometry reconstruction (see section 2.1.3).

One also sees that the mean of the core error distribution is shifted to negative values, i.e. on average the reconstructed core distance is significantly smaller than the true core distance.

In the next section it will be investigated how the reduced core resolution for two- and three-telescope-events (especially for 50° zenith angle) influences the energy reconstruction.

3.3 Energy bias

As discussed in section 2.3.5, the energy of the primary particle is reconstructed by comparing the reconstructed size and impact distance with lookup tables. Since the impact distance is the distance from the center of the array to the core position of the shower, the core resolution is crucial for the accuracy of the energy reconstruction.

In order to quantify the accuracy of the energy reconstruction for a particular event, the relative error in the reconstructed energy E_{rec} with regards to the simulated energy, E_{MC}, is determined. One then defines the **energy bias** $\overline{\Delta E}$ as the relative error of the reconstructed energy averaged over all events with a specific energy:

$$\overline{\Delta E} = \quad < \frac{E_{\mathrm{rec}} - E_{\mathrm{MC}}}{E_{\mathrm{MC}}} > \tag{3.2}$$

The relative error of the energy reconstruction as a function of E_{MC} is filled into a two dimensional histogram using the same Monte Carlo simulations that were used to estimate

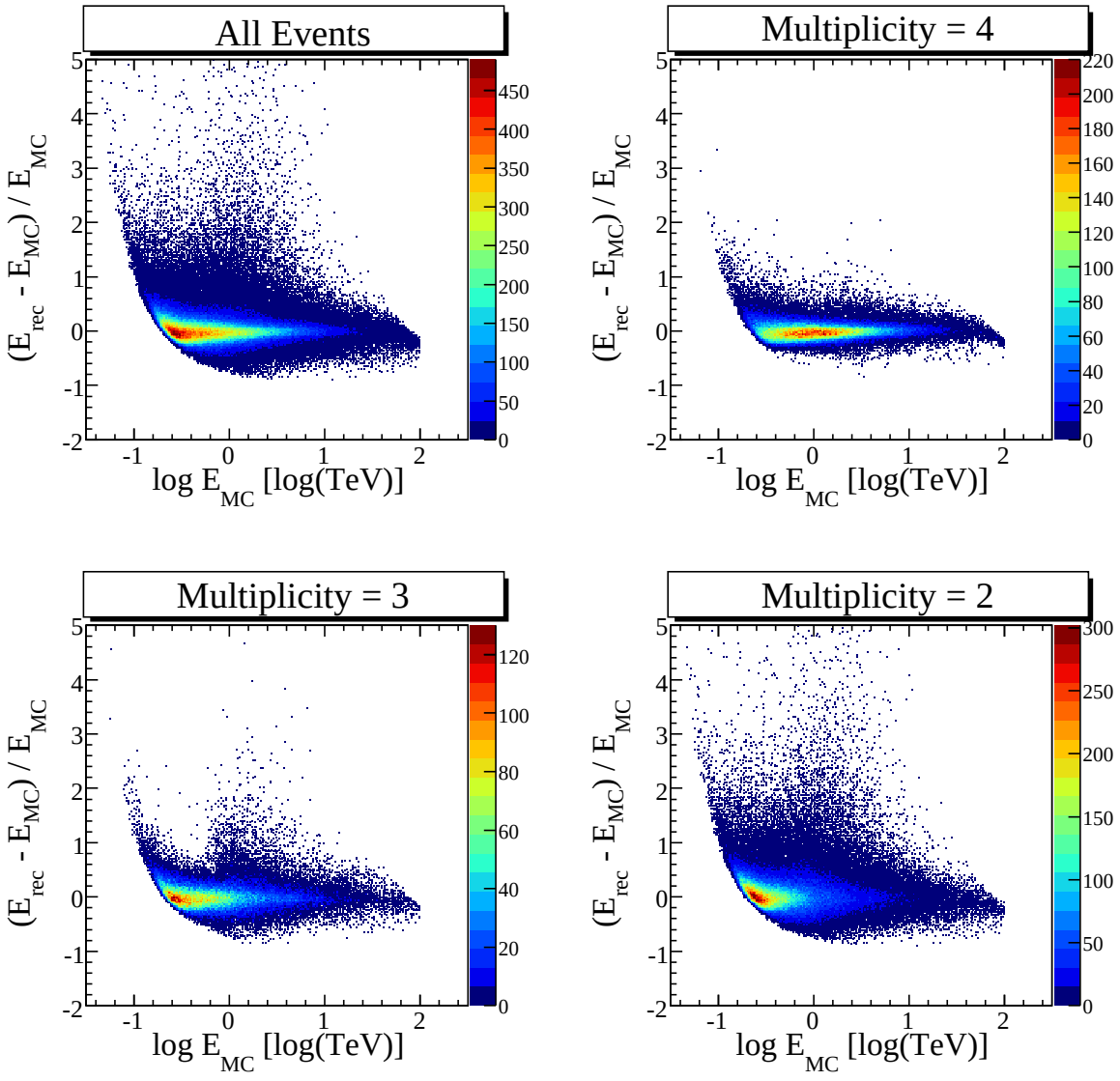

Fig. 3.4: Two dimensional distributions displaying the relative energy error $\Delta E = \frac{E_{\mathrm{rec}} - E_{\mathrm{MC}}}{E_{\mathrm{MC}}}$ as a function of the energy for VHE γ-rays simulated at 20° zenith and 0.5° offset for different multiplicities. Only events that passed standard cuts are included.

the core resolution. For 20° zenith, these histograms for the respective event multiplicities are shown in Fig. 3.4. The corresponding histograms for 50° zenith can be found in Fig. 3.5.

In order to get an average value for the energy bias in a specific energy range, the distribution was sliced in energy bins and each slice fitted by a Gaussian. The results for both 20° and 50° zenith can be found in Fig. 3.6.

Discernible in all plots is an increase of the energy bias at small energies, which is the result of a selection effect: showers with low energies that show an upward fluctuation in size remain in the analysis while others are rejected by the size cut. As a consequence, the reconstructed energy of these events is generally higher than the simulated energy,

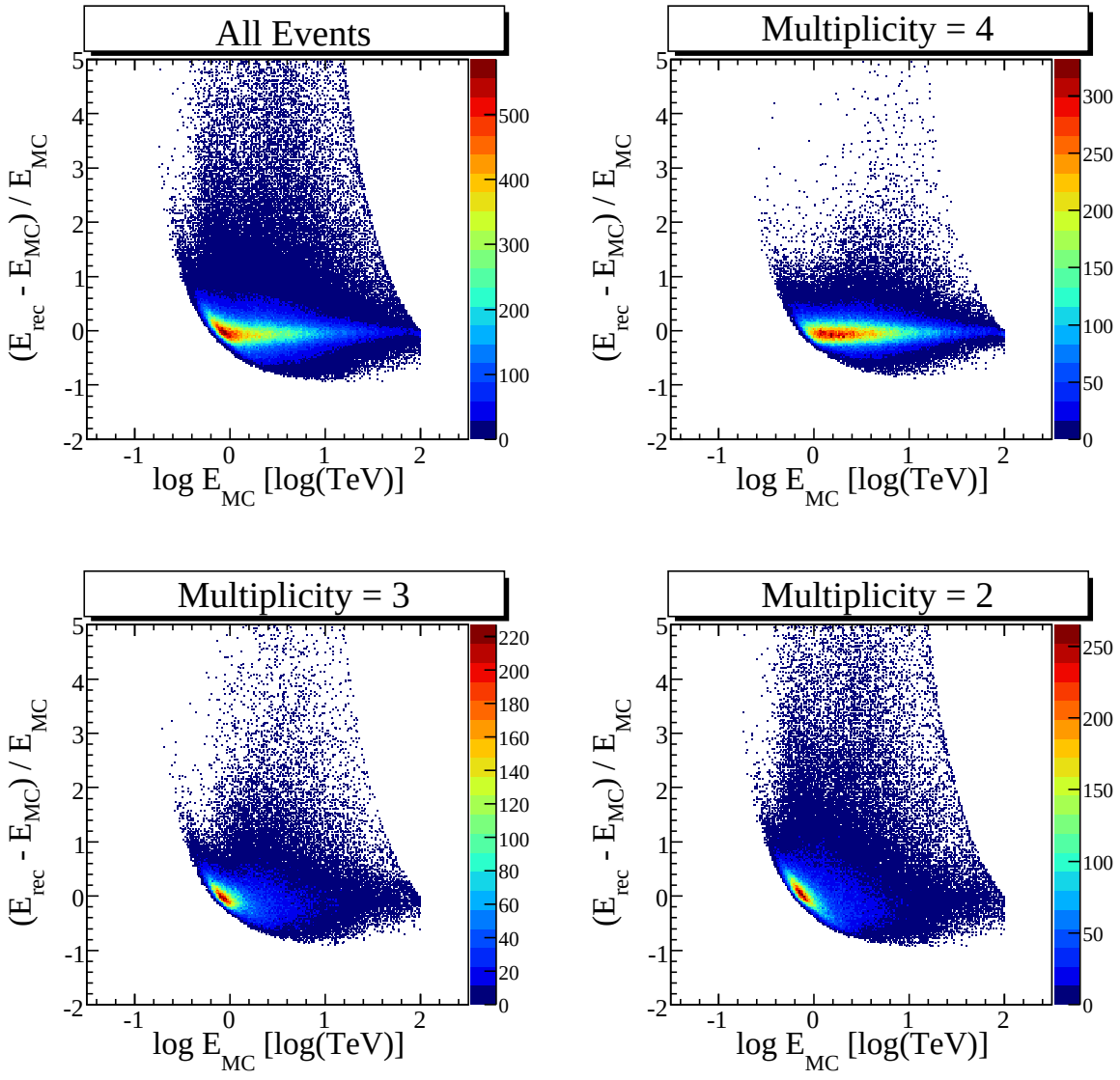

Fig. 3.5: Two dimensional distributions displaying the relative energy error $\Delta E = \frac{E_{\mathrm{rec}} - E_{\mathrm{MC}}}{E_{\mathrm{MC}}}$ as a function of the energy for VHE γ-rays simulated at 50° zenith and 0.5° offset for different multiplicities. Only events that passed standard cuts are included.

resulting in a positive energy bias. The opposite happens at very large energies, where no events with upward fluctuations appear in the analysis as the VHE γ-rays are only simulated up to a certain energy. Consequently, only showers that show a downward fluctuation in size are included, which causes a negative bias for very high energies.

In order to use only events with accurately reconstructed energy for the production of the energy spectrum, one defines a useful energy range that excludes the region with high energy biases at small energies. Therefore the lowest energy bin with an average energy bias $< 10\%$ is found. The **safe energy threshold** is then defined as the energy of this bin plus 10% (see the vertical dashed lines in the top left plot in Fig. 3.6). Due to the stricter size selection, the energy threshold increases when applying hard cuts to a data

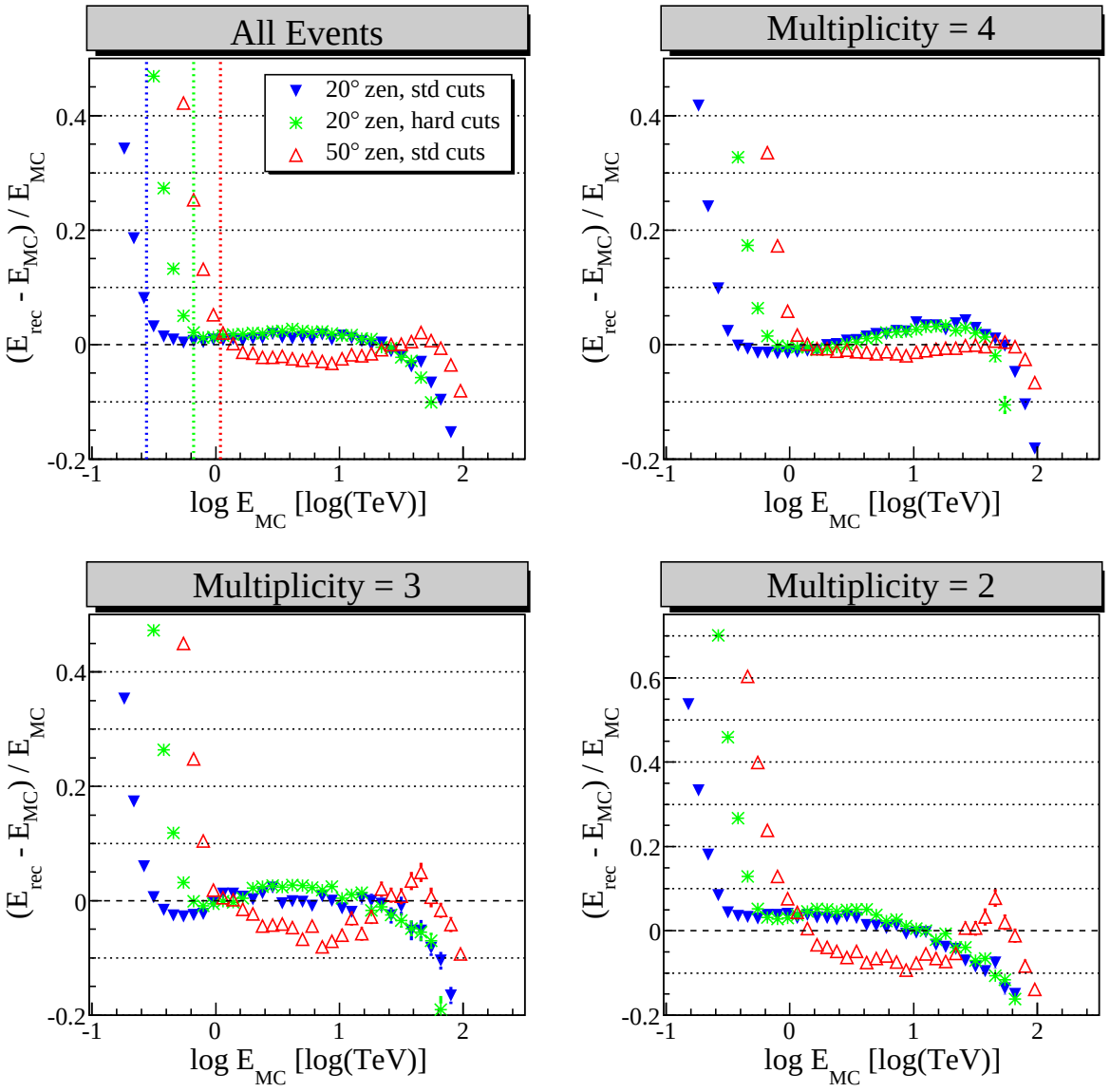

Fig. 3.6: Profile plots displaying the energy bias $\overline{\Delta E} = < \frac{E_{\mathrm{rec}} - E_{\mathrm{MC}}}{E_{\mathrm{MC}}} >$, i.e. the average relative energy error as a function of the energy, for different multiplicities and for two Monte Carlo data sets simulated under 20° zenith and 50°, respectively. The colored vertical lines in the top left plot are the safe energy thresholds estimated for the respective data sets.

set. It shifts to even higher energies when observing under large zenith angles. Again, the reason for this is the larger distance between the shower maximum and the telescope array. Consequently, showers have to have a larger energy to be detected by the telescope system.

Note that the safe energy threshold also depends on the optical efficiency of the system (see section 2.3.5). Since in this work, Monte Carlo simulations with a reduced optical efficiency were used, the respective safe energy thresholds are shifted to higher energies compared to earlier studies of the telescope system [10]. Here, the safe energy threshold

for all events combined for 20° zenith angle is ≈ 300 GeV for standard cuts and ≈ 760 GeV for hard cuts. For 50° zenith angle and standard cuts, the safe energy threshold shifts to ≈ 1.1 TeV.

Above the safe energy threshold, the energy bias curves are flat up to 50 TeV, the exception being two- and three-telescope-events at 50° zenith. Here the curve is not as smooth, with the average energy bias for different energies being in between ±10%. This is very likely a result of the reduced accuracy of the core estimation for two- and three-telescope-events at 50° zenith.

3.4 Energy resolution

When interpreting observations of VHE γ-ray sources, it is important to give an estimate of the average error made in the energy reconstruction. Such an estimate is the average scattering of the reconstructed energy around the simulated energy, i.e. the **energy resolution**. The energy resolution as a function of the energy can be obtained by taking the standard deviation of the Gaussian fitted to the energy bias distribution in each energy-bin.

In Fig. 3.7, the energy resolution as a function of the energy for the previously used simulations and different multiplicities is shown. In order to get an estimate for the average energy resolution, one analyses the distribution of the energy biases for all events, see Fig. 3.8. As a measure of the average scattering around $\Delta E = 0$, the width of the Gaussian fitted to this distribution is taken. This value is taken as the **overall energy resolution**. The results for different multiplicities and zenith angles can be found in table 3.2. Note that the width of the distribution depends on the spectral index Γ. Due to the softer spectrum utilised in this work, more events with higher energies are included in the data set, which results in an slightly higher overall energy resolution than in the case of a steeper spectrum.

zenith angle	**all events** [%]	**Mult=4** [%]	**Mult=3** [%]	**Mult=2** [%]
20° zen	16.72 ± 0.03	11.85 ± 0.03	17.32 ± 0.07	22.75 ± 0.06
50° zen	23.45 ± 0.04	17.88 ± 0.04	27.41 ± 0.09	33.22 ± 0.13

Tab. 3.2: Values for the energy resolution averaged over all energies for different multiplicities, see Fig. 3.8. Standard cuts were applied.

One can see that for 20° zenith, the energy resolution for all events combined amounts to ≃ 18%, but is noticeably better when selecting only four-telescope-events, in which case it is ≃ 12%. One notices that the energy resolution for 50° zenith is significantly worse, especially for two- and three-telescope-events. This worsening can be understood when looking at the corresponding energy bias histograms in Fig. 3.5. One there sees a long "tail" of events with an energy bias > 1.0 in the distributions for two- and three-telescope-events.[3] These are events with core distances far outside of the array (> 400 m)

[3]This tail is also present for 20° zenith but much less pronounced, see Fig. 3.4.

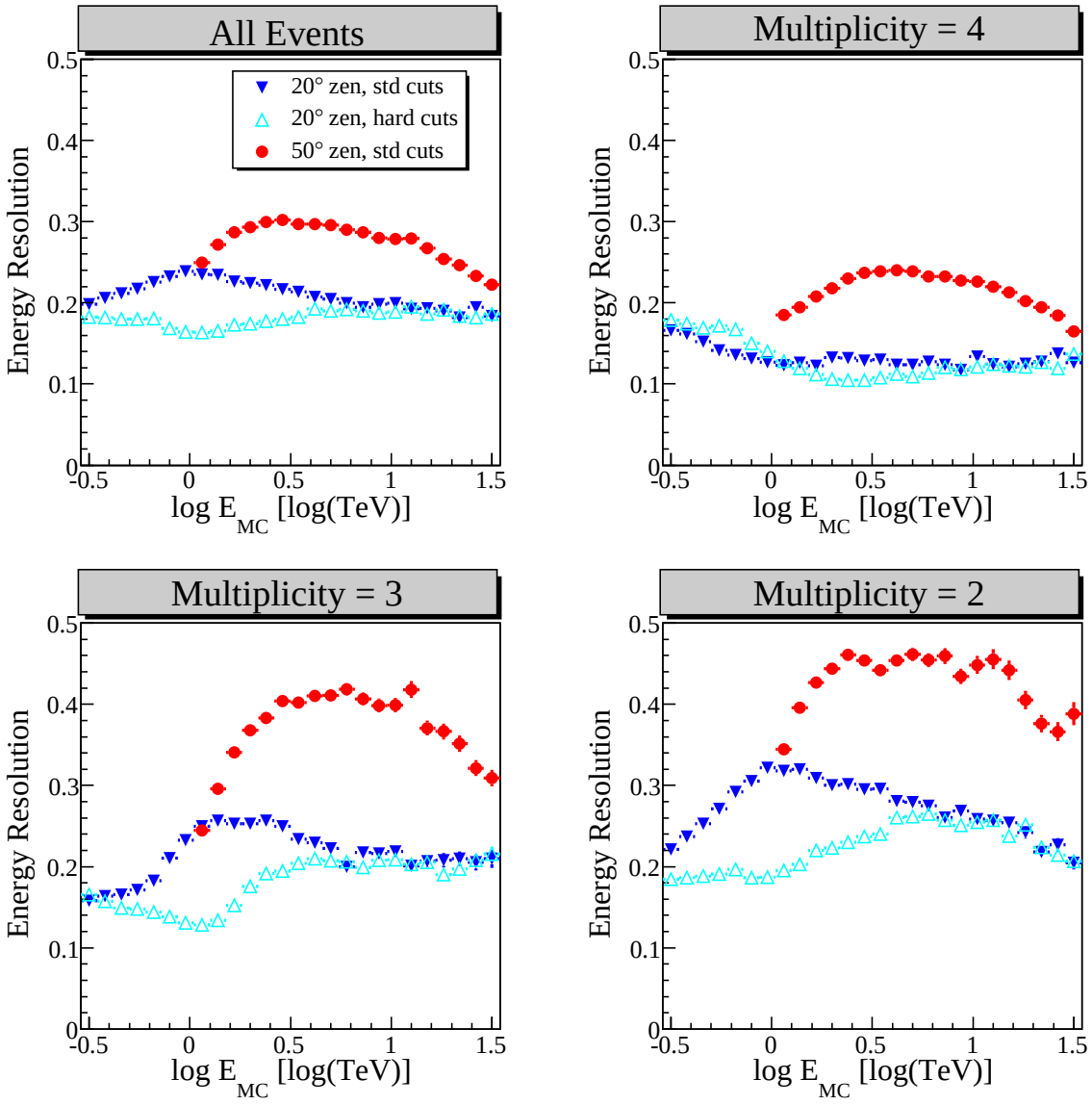

Fig. 3.7: Energy resolution as a function of the simulated energy for different multiplicities and for two Monte Carlo data sets simulated under 20° and 50° zenith, respectively. Note that data points for the resolution are only shown above the safe energy threshold ($\simeq 1$ TeV for 50° zenith).

and for which the error of the core estimation is very high. This leads to an average overestimation of the reconstructed energy: If one looks at the energy lookup table for 50° zenith in Fig. 2.12, one sees that for 400 m impact distance and for a fixed low size, the gradient in energy for decreasing distances is less steep than the gradient for increasing distances. Hence, large statistical fluctuations in the impact distance will result in an overall overestimation of the reconstructed energy.

A possibility to improve the energy resolution at the expense of reduced event statistics is to exclude events with large core distances, as these are mostly events for which the energy reconstruction suffers from large inaccuracies. Alternatively, a cut on small stereo

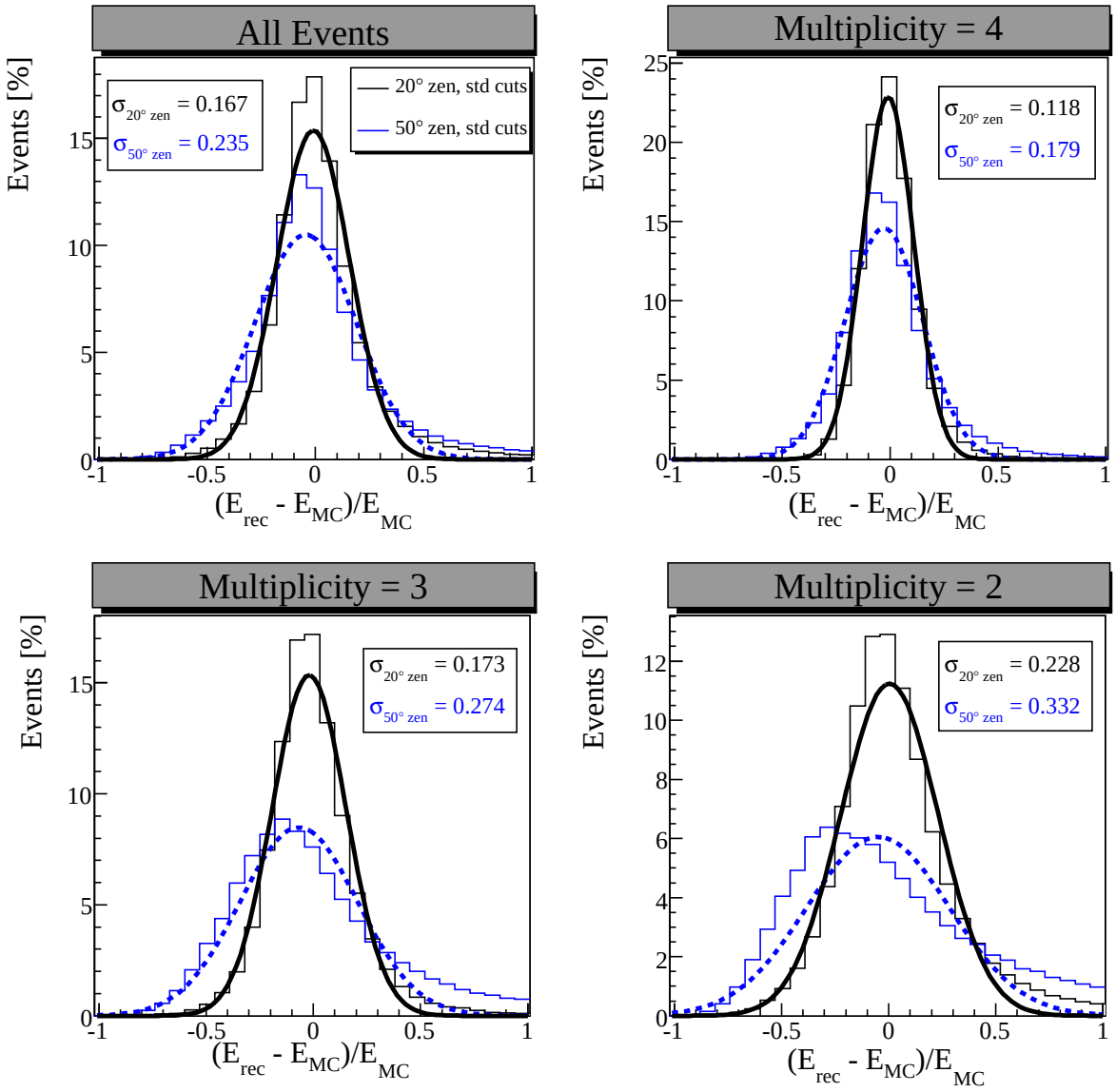

Fig. 3.8: Energy bias distribution for all energy bins. Two Monte Carlo simulations of 20° and 50° zenith were used. A Gaussian was fitted to each distribution. σ denotes the width of the Gaussian and is taken as the **overall energy resolution** for the respective multiplicity.

angles would have a similar effect. However, the testing and implementation of such cuts is beyond the scope of this thesis.

3.5 Summary

This chapter compared the systematics in the energy reconstruction of H.E.S.S. for different event multiplicities and zenith angles. For this the reconstruction chain was tested with two Monte Carlo simulations with 20° and 50° zenith angle, respectively, and 0.5°

offset.

It was found that, at 20° zenith angle, events with lower multiplicities are especially important for energies $< 1\,\mathrm{TeV}$, whereas for large energies and 50° zenith angle most events are four-telescope-events.

Furthermore, it was shown that the core position reconstruction using only two or three telescopes is less accurate. Additionally, the core resolution worsens with increasing zenith: for observations at 20° zenith angle, the core resolution amounts to $\simeq 13\,\mathrm{m}$ (for all multiplicities combined), whereas for 50° zenith angle and all multiplicities, the core resolution is $\simeq 62\,\mathrm{m}$.

The energy bias was introduced as the relative deviation of the reconstructed energy from the simulated energy. It was found that it amounts to $< 5\%$ for four-telescope-events for both zenith angles under consideration. At 50° zenith, two- and three-telescope-events suffer from an energy bias of up to 10%, which is likely the result of the large error in the core estimation for these event classes.

Finally the overall energy resolution of H.E.S.S. was estimated and it was found that it is $\simeq 18\%$ for observations at 20° zenith and 24% for observations at 50° zenith. The worsening of the energy resolution with increasing zenith can be explained by the wrong reconstruction of two- and three-telecope-events with core distances $> 400\,\mathrm{m}$. In this context, it is eventually worth considering whether a cut on the core distance (e.g. $< 400\,\mathrm{m}$) or on small stereo angles (e.g. $\phi_{i,j} > 20°$) could improve the overall energy reconstruction of H.E.S.S. since these cuts would exclude events with misreconstructed core distances and energies.

The next chapter will investigate whether there are asymmetries in the geometry- and energy-reconstruction between individual telescopes by applying several intercalibration methods to two VHE γ-ray data sets. The reconstruction errors stemming from eventual differences will then be compared with the uncertainty of the overall energy reconstruction that was discussed in this chapter.

Chapter 4

Inter-telescope Systematics

In the last chapter, possible systematics of the energy reconstruction using two, three or four telescopes were examined. In this chapter, the investigation of the energy reconstruction of individual telescopes in H.E.S.S. is described and it is discussed how these compare with each other. Comparing the individual telescope responses is important, given the fact that all four telescopes of H.E.S.S. have now run for almost six years, during which the system has been affected by two major effects:

1. Due to corrosion, the telescope mirrors and the Winston cones (see section 2.2.2) have degraded permanently.

2. The gain of the photo multipliers has been adjusted in regular intervals in order to account for the degradation of the system.

Even though the optical efficiencies of the telescopes are regularly estimated using the muon-correction (2.3.6), it is not clear whether these corrections are sufficient to compensate for the changing optical efficiencies. The methods utilised in this chapter allow to verify the functionality of the muon-correction.

In the course of this investigation, it is be checked whether the changes in the telescope system have an impact on the energy reconstruction of the individual telescopes. In order to search for asymmetries in between the respective responses of the telescopes, all four telescopes in the array are compared pairwise. Two methods are used for this pairwise comparison of the telescopes:

- The first method tests whether the two telescopes under consideration reconstruct Cherenkov showers differently. This is done by evaluating the relation between the size and the reconstructed impact distance (see section 2.3.2 for a definition of size and impact distance). As can be seen in chapter 2.3.3, each telescope detects a different size when taking an image of an air shower: the larger the impact distance, the smaller the reconstructed size. For the same shower, one expects the relation between these two parameters to be the same for all telescopes. Hence, by comparing

the differences in size with the differences in reconstructed distance for a telescope pair, one is able to find possible asymmetries in the shower parameter reconstruction in between these two telescopes. If all telescope pairs are compared accordingly, one is able to quantify asymmetries in the telescope responses within the whole array. This method was already applied to the HEGRA telescopes ([26]) and is henceforth called **size-distance intercalibration** (section 4.1).

- The second method compares the energies reconstructed by the individual telescopes. As was shown in chapter 2.3.5, each telescope gives a separate estimate of the primary particle's energy. The energy estimates of all telescopes are then weighted and averaged to calculate the mean energy of the event. The telescope energies are again compared pairwise. This will be called **energy intercalibration** (section 4.2). It is also evaluated how much each telescope's reconstructed energy deviates from the averaged energy of all four telescopes. Thereby it can be checked whether the individual energy reconstruction of one telescope is flawed. This will be called **relative energy calibration** (section 4.3).

Both methods are first tested by applying them to Monte Carlo simulations. After confirming the functionality of the methods, the intercalibration is undertaken for real observational data.

Note that the energy that is used for the spectral studies of VHE γ-ray sources, in contrast to the size, is muon-corrected (see 2.3.6). Differences in the asymmetries found by the two methods can thus be used to analyse the functionality of the muon correction.

As VHE γ-ray sources providing the observational data needed for the systematical tests in this chapter, PKS 2155–304 and the Crab Nebula are taken. These are two of the brightest H.E.S.S. sources that have been monitored over a long time, with rather different mean zenith angles.

For the AGN PKS 2155–304, two different data sets are compared. On the one hand, a data set consisting of almost exclusively VHE γ-rays was used. It only consists of three runs (taken on July 28, 2006) during which PKS 2155–304 was in an exceptional high state. On the other hand, the full data set taken on PKS 2155–304 in the last five years was utilized, which consists of background events also. As a source that was observed under a larger zenith-angle, the third data set used for the following analysis is the Crab Nebula. All observational data taken by H.E.S.S. during the last five years is used for the tests in this chapter. Some properties of the three data sets are summarized in table 4.1.

At the end of this chapter (section 4.4), in order to see whether systematic effects have increased in the last years, the time evolution of asymmetries is investigated. Therefore, the full PKS 2155–304 data set (spanning almost six years) is divided into three two-year long subsets, for which the time evolution of the different asymmetries is examined.

The next section introduces the size-distance intercalibration, that is tested with Monte Carlo simulations and is then applied to the VHE γ-ray data sets listed above.

source	N_{total}	live time	back-ground	average zenith
PKS 2155–304 (bigflare)	5967	1.3 h	1.0%	13.3°
PKS 2155–304 (full data set)	67552	205.4 h	17.5%	20.4°
Crab Nebula	8632	21.8 h	11.3%	48.1°

Tab. 4.1: Properties of the three VHE γ-ray data sets used for the intercalibration in this chapter. N_{total} denotes the total amount of events in the data set (after standard cuts). The background percentage was calculated according to: $1 - \frac{N_{excess}}{N_{total}}$.

4.1 Size-distance intercalibration

The size-distance intercalibration can be used to compare the response of the different telescopes in H.E.S.S.. In order to find possible asymmetries within the array, one compares how the same event is reconstructed by the different telescopes, i.e. at different distances. Therefore the size $s_i(E_\gamma, d_i)$ (reconstructed by telescope i for a shower impact distance d_i that was triggered by a VHE γ-ray with E_γ) is compared with the size $s_j(E_\gamma, d_j)$ of the same shower reconstructed by telescope j.

One then evaluates the difference of $s_i(E_\gamma, d_i)$ and $s_j(E_\gamma, d_j)$ for events with $d_i \approx d_j$. If the responses of the two telescopes under consideration are similar, one expects that $s_i(E_\gamma, d_i) \approx s_j(E_\gamma, d_j)$.

In order to calculate the size-distance asymmetry for a telescope pair, one introduces two variables that display the differences in size and distance, respectively. To get values ranging from -1.0 to 1.0, one scales the difference of the detected sizes s_i and s_j with the sum of the two values and defines the **size asymmetry** a_s as

$$a_s = \frac{s_i - s_j}{s_i + s_j} \tag{4.1}$$

The difference of the impact distances for the two telescopes, d_i and d_j are scaled in a similar way:

$$a_d = \frac{d_i - d_j}{d_i + d_j} \tag{4.2}$$

with a_d being the **distance asymmetry**. For a proper intercalibration of the array, one expects $a_s = 0$ for $a_d = 0$. For an error ϵ in the intercalibration one obtains differing sizes $s_i = f(d_i)$ and $s_j = (1+\epsilon) \cdot f(d_j)$ which results in $a_s(a_d = 0) = \frac{\epsilon}{\epsilon+2}$. Thus, for $\epsilon \ll 1$, the size-distance asymmetry is only half as large as the actual error in the intercalibration.

4.1.1 Core position reconstruction with two telescopes

In the following, the size asymmetry and the distance asymmetry of two telescopes for all events in various data sets are evaluated. This is done for all telescope pairs. For the four telescopes of H.E.S.S., this corresponds to six combinations. For each telescope pair, the impact distance was calculated. The images from the other two telescopes (even if they have also seen and reconstructed the shower) were ignored in the core position reconstruction.

As was described in section 2.3.3, the core position is obtained by intersecting the image axes of the shower images in the ground system. The image axes are drawn along the long axis of the Hillas ellipse, which is constructed for each camera image. When using only two images, this geometry reconstruction is obviously inferior (i.e. suffers from a larger error) to the reconstruction using all four telescopes. It is nevertheless used here in order to discover possible systematics in the shower reconstruction of the telescope pair under scrutiny.

4.1.2 Event selection

Not all events in the available data sets are used for the size-distance intercalibration. For the pairwise comparison of telescopes, events are selected such that the two telescopes (and possibly others) under consideration have both triggered and passed standard cuts (2.3.4) on size, local distance in the camera, θ^2, Mean Scaled Length and Mean Scaled Width (see section 2.3). The standard cuts are applied in order to improve the image quality and reject background events. In order to stay consistent with the distance reconstruction and possible effects between telescopes, both the Mean Scaled Width and the Mean Scaled Length of an event are determined using only the two telescopes that should be compared.

In addition, a cut on the stereo angle $30° < \phi_{i,j} < 150°$ (see 2.3.3) is used. This cut guarantees that the intersected image axes are neither remotely parallel nor that they intersect at small angles, both of which reduces the accuracy of the geometry reconstruction.

4.1.3 Understanding the size-distance asymmetry

Before the different steps in the intercalibration-routine are discussed, a short explanation of the shape of the size-distance-asymmetry plot is given. In Fig. 4.1, one can see the size asymmetry as a function of the distance asymmetry for the telescope pair CT1-CT3. Here, a set of Monte Carlo simulations with 0.5° offset and 20° zenith was used. Each data point in the plot corresponds to a simulated event.

One would expect to see an anti-proportional behaviour of the size asymmetry and the distance asymmetry. This trend is visible in the plot, yet it is superimposed by a horizontal structure. Events in this horizontal structure have different impact distances but similar sizes. The origin of these events becomes clear when one again looks at the relation between size and impact distance (Fig. 2.6): for all impact distances $d_i, d_j < 130\,\mathrm{m}$, i.e. if the telescope that detects the shower lies within the central region of the Cherenkov-

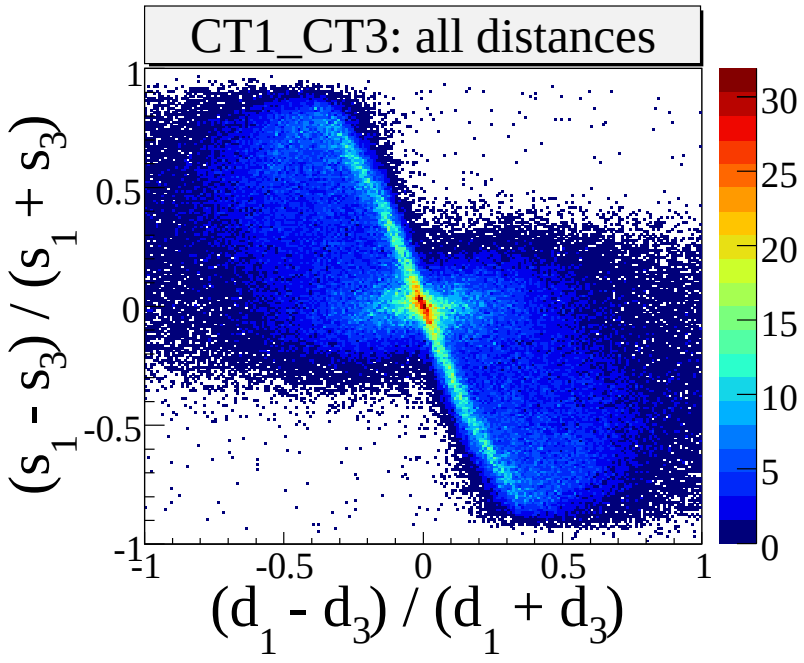

Fig. 4.1: Size asymmetry as a function of the distance asymmetry for the telescope pair CT1-CT3. All impact distances were included.

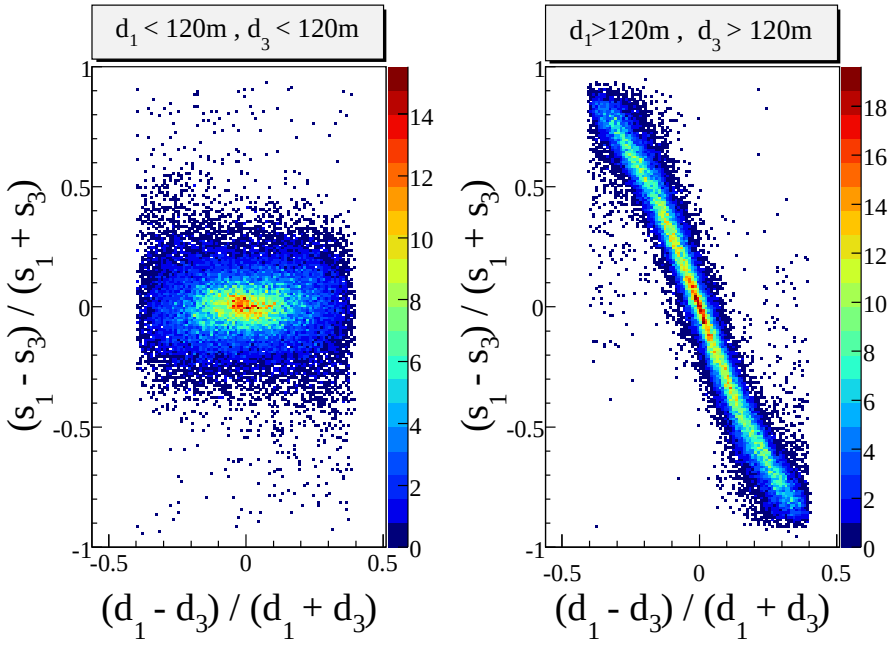

Fig. 4.2: Selection of the Fig. 4.1. *Left:* Only events where the impact distance for both CT1 and CT3 is below 130 m are included. *Right:* Only events where both impact distances were larger than 130 m are included.

light pool, the reconstructed size of the shower is almost constant. Hence, if the core position of a shower is close to (e.g. in between) the two telescopes under consideration, the size asymmetry is ≈ 0 whereas the distance asymmetry is $\neq 0$. Only if $d_{i,j} > 130\,\mathrm{m}$,

i.e. both telescopes lie outside of the Cherenkov light-pool, one observes the expected anti-proportional relation between the size asymmetry and the distance asymmetry.

This is visualised in Fig. 4.2, where selections of the events in 4.1 are shown. In the left plot, the case where both telescopes lie *within* the Cherenkov light-pool is displayed. In the right plot, the case where both telescopes lie *outside* of the central region of Cherenkov light-pool is shown. Events with $d_i < 130\,\mathrm{m} < d_j$ are not considered, explaining why the respective-distributions in Fig. 4.2 lack events with $|a_d| > 0.4$.

The fact that the anti-proportional relation between size and impact distance is only valid for large impact distances, is taken into account in the next section, when two methods are introduced to obtain a value that quantifies possible asymmetries in between two telescopes.

4.1.4 Calculation of the asymmetry values

In this section, it will be explained how a value for the average asymmetry of a telescope pair can be determined from size-distance asymmetry distributions like Fig. 4.1. One evaluates the mean size asymmetry for events with equal impact distances, i.e. with distance asymmetry $a_d \approx 0$. According to [26], this can either be done by fitting the size asymmetry distribution with a Gaussian (**Gauss method**) or by determining the deviation of the size-distance-asymmetry of events with large impact distances from an anti-linear fit (**linear method**). The two respective methods are explained in the following.

Gauss method

The Gauss method is visualised in Fig. 4.3. One evaluates the size asymmetry distribution for events with no distance asymmetry, i.e. one analyses the distribution of a_s at $|a_d| < 0.05$, i.e. in the central x-bins of the size-distance-asymmetry plot. The a_s-distribution in these central bins can be approximated by a Gaussian. The mean value of this fit is then taken as $a_s^{i,j}$, the **size-distance asymmetry of telescope pair i,j**. Note that for this method, events with all impact distances are included.[1]

Linear method

The linear method is visualised in Fig 4.4. Only events with impact distances larger than the Cherenkov light-pool radius are taken (see argumentation in the previous section), which allows to exploit the expected anti-linear behaviour of the size-distance asymmetry plot. In the corresponding size-distance asymmetry histogram, one averages a_s in each a_d bin and thereby obtains one data point per bin. This profile-plot is then fitted with a linear curve. In a perfectly calibrated array, one would expect that $a_s(a_d = 0) = 0$.

[1] Events from the horizontal structure of the size-distance asymmetry plot are taken in order to include the important group of events with core positions within the array, i.e. between the four telescopes. However, since these events have almost no size asymmetry, they may reduce the asymmetry value obtained from this method somewhat.

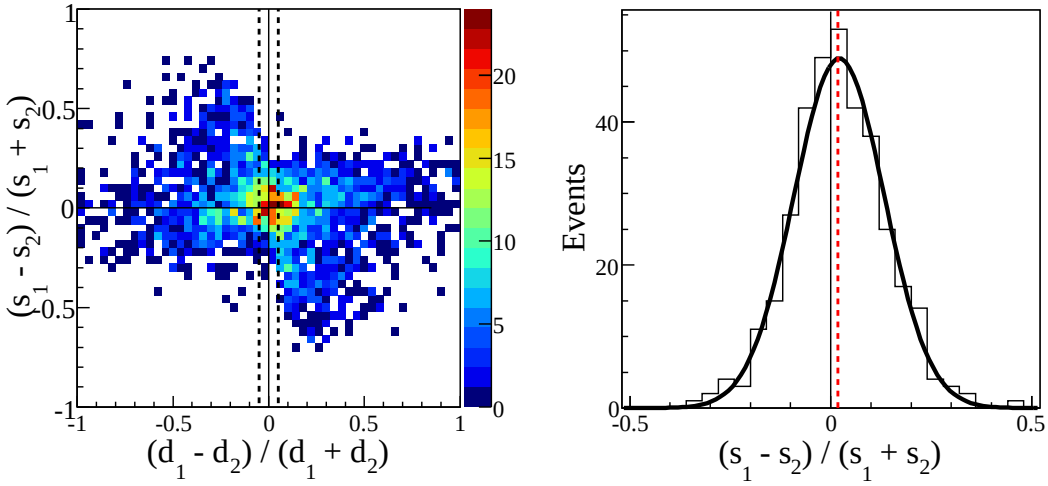

Fig. 4.3: Illustration of the **Gauss method**. *Left:* Size asymmetry as a function of the distance asymmetry for the telescope pair CT1-CT2 and the PKS 2155–304 bigflare data set, including events with all impact distances. 500 events of the data set pass standard cuts and the cut on the stereo angle. *Right:* a_s-distribution for $|a_d| < 0.05$, i.e. event distribution of the region between the dashed lines in the asymmetry histogram (left plot). The asymmetry value $a_s^{1,2}$ for the telescope pair CT1-CT2 is then the mean value of the Gauss fit applied to this distribution (dashed red line).

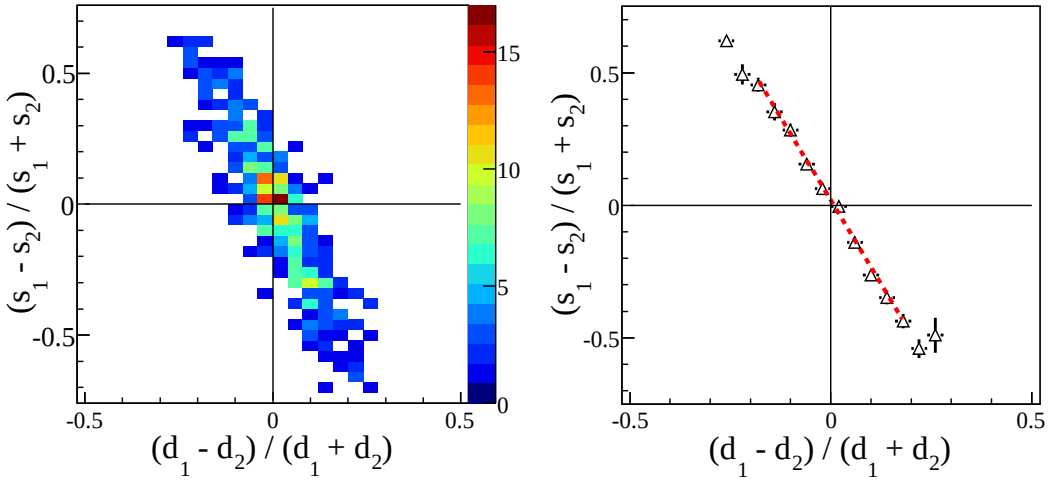

Fig. 4.4: Illustration of the **linear method**. *Left:* Size asymmetry as a function of the distance asymmetry for the telescope pair CT1-CT2 and the PKS 2155–304 bigflare data set, including only impact distances above 130 m. 300 events of the data set pass standard cuts and the stereo cut. *Right:* Profile of the size-distance asymmetry histogram (left), obtained by averaging in each x-bin. The intersection of the linear fit (dashed red line) and the horizontal line at $x = 0$ gives the asymmetry value $a_s^{1,2}$ for the telescope pair CT1-CT2.

Any asymmetry in a_s results in $a_s(a_d = 0) \neq 0$. This deviation can be taken as $a_s^{i,j}$ the **asymmetry value of the telescope pair i,j**, corresponding to the value obtained with

the Gauss method. It can be easily obtained by taking the intersection point of the linear fit and a vertical line at $x = 0$.

The different size asymmetry plots for the PKS 2155–304 bigflare data set for the Gauss method and the linear method are displayed in Figs. 4.5 and 4.6, respectively. The corresponding size-distance asymmetry plots for the other data sets together with the linear profile-plots and the distribution plots, to which the Gauss fit was applied, can be found in appendix B.

Intercalibration sum

Once one has obtained a size-distance asymmetry value for each of the six telescope pairs, one wants to check the consistency of the obtained asymmetry values. This can for example be done by calculating the sum of the asymmetry values for the four edge pairs of the telescope array:

$$\sum_{\text{interc.}} = a_s^{1,2}(0) + a_s^{2,3}(0) + a_s^{3,4}(0) + a_s^{4,1}(0) \tag{4.3}$$

One expects this sum to be close to 0, otherwise there would be a systematic error in the intercalibration method. The error of the intercalibration sum is calculated according to Gaussian error propagation.

4.1.5 Results of the size-distance intercalibration

In this section, both the Gauss and the linear method are tested by applying them to various data sets obtained from Monte Carlo simulations. On the one hand, the methods are tested with simulations with differing optical efficiencies, on the other hand the behaviour of the methods for varying zenith angles are evaluated. Thereby it is also checked whether the two methods give compatible results.

After the tests using simulations, size-distance asymmetries for the real VHE γ-ray sources PKS 2155–304 and the Crab Nebula are calculated.

Monte Carlo simulations with differing optical efficiencies

Perfectly suited for the testing are two sets of Monte Carlo simulations that were produced at different points in time in order to simulate the energy reconstruction of H.E.S.S.. In the "phase1" and "phase1b" simulations (see 2.3.5), different optical efficiencies are attributed to the individual telescopes (see table 2.2). In phase1 simulations, CT3 is simulated with a different optical efficiency than the other telescopes[2], whereas in the phase1b simulations, all telescopes have the same (reduced) optical efficiency. By using the size-distance intercalibration methods introduced in the previous section, one should

[2]Taking into account that it was completed one and a half years prior to the other three telescopes

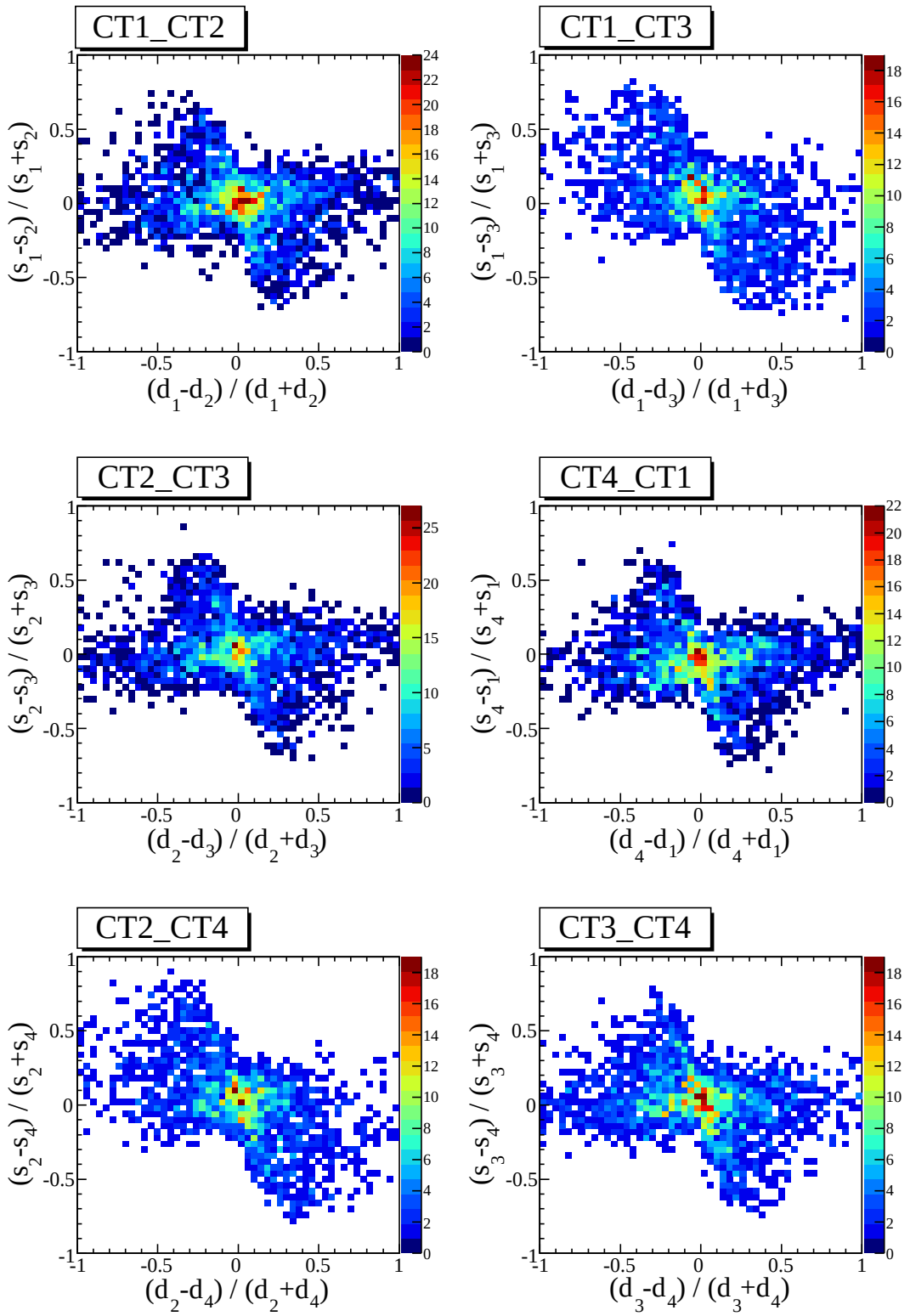

Fig. 4.5: Size-distance asymmetry histograms for all telescope pairs and the PKS 2155–304 bigflare data set. Events with all impact distances are included.

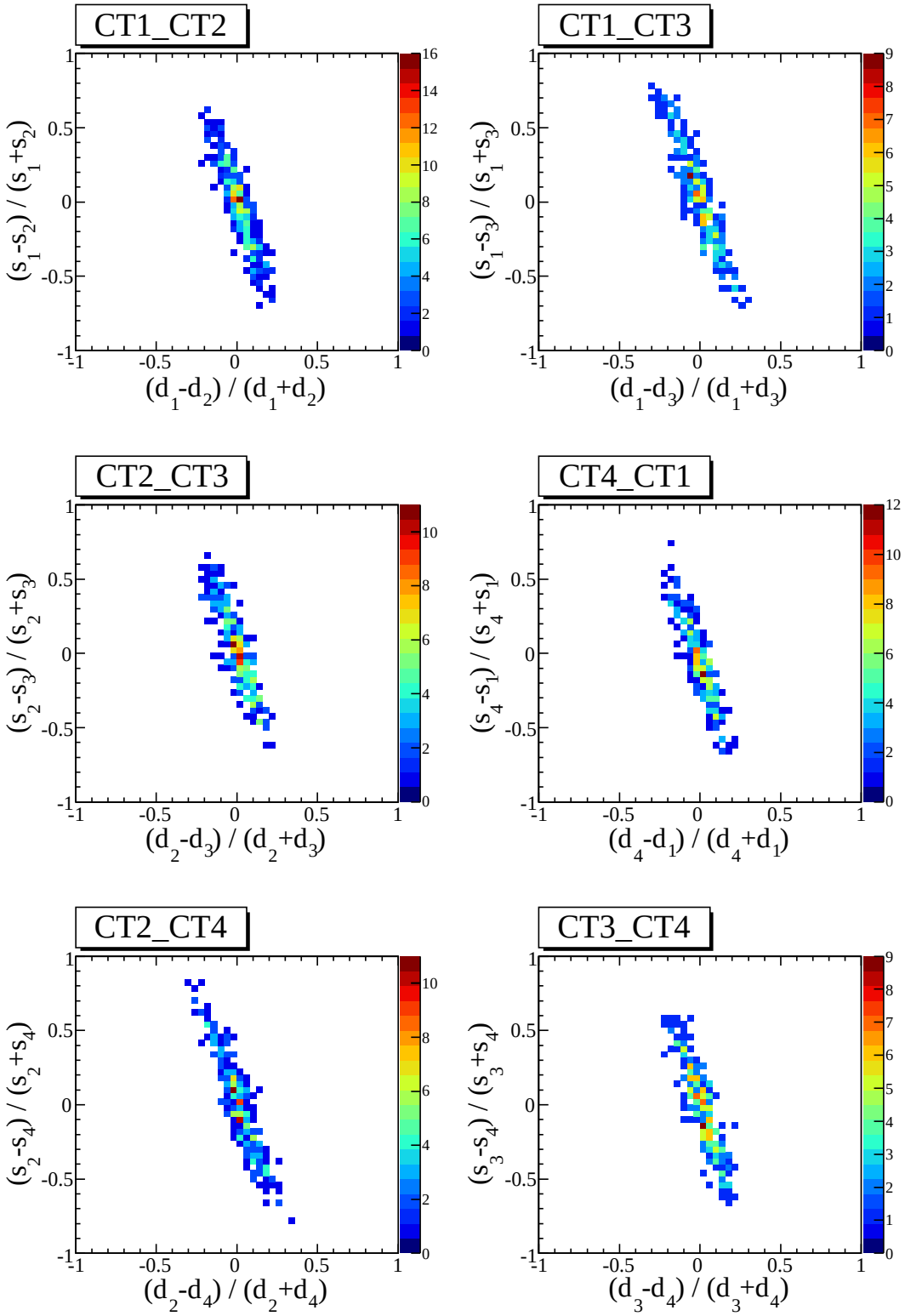

Fig. 4.6: Size-distance asymmetry histograms for all telescope pairs and the PKS 2155–304 bigflare data set. Only events with impact distances d_i, $d_j > 130\,\mathrm{m}$ are included.

be able to quantify the differing response of CT3 in phase1 simulations and thereby confirm the functioning of the intercalibration methods.

For phase1, CT3 is simulated with only 92% optical efficiency (compared to 100% for the other three telescopes), one therefore expects to find the following size-distance asymmetry value for all telescope pairs involving CT3:

$$a_s^{i,3}(0) = \frac{s_i - s_3}{s_i + s_3}(0) \simeq \frac{1.0 - 0.92}{1.0 + 0.92} = 0.042 \tag{4.4}$$

For all pairs where CT3 is not involved one expects to find no asymmetry. The same applies for all telescope pairs for the phase1b data set.

This expected behaviour is indeed confirmed, as can be seen in table 4.2, where the asymmetries of all telescope pairs for both methods and both simulated configurations are displayed. The magnitude of the asymmetry values of all pairs involving CT3 for phase1 simulations is ≈ 0.042, whereas all other combinations yield an asymmetry close to zero.

	linear method		**Gauss method**	
Telescope pairs	**phase1** ($\pm$0.001)	**phase1b** ($\pm$0.001)	**phase1** ($\pm$0.001)	**phase1b** ($\pm$0.001)
CT1-CT2	-0.005	-0.004	-0.002	0.000
CT1-CT3	**0.043**	0.002	**0.046**	0.003
CT4-CT1	-0.003	-0.004	-0.000	-0.001
CT2-CT3	**0.046**	0.005	**0.045**	0.002
CT2-CT4	0.013	0.014	0.017	0.014
CT3-CT4	**-0.039**	0.003	**-0.043**	-0.000
$\sum_{\text{interc.}}$	-0.001 $\pm$0.002	0.001 $\pm$0.002	$3 \cdot 10^{-4}$ $\pm$0.003	0.002 $\pm$0.002

Tab. 4.2: Size-distance asymmetry values and intercalibration sum for phase1 and phase1b Monte Carlo simulations, simulated under 0.5° offset and 0° zenith. $\sum_{\text{interc.}}$ was calculated according to (4.3). In phase1 Monte Carlos, CT3 has a reduced optical efficiency of only 92% whereas in phase1b simulations all CTs have the same optical efficiency (70%). As a result of this, for phase1 simulations, the intercalibration asymmetry is $\simeq 0.042$ whenever CT3 is compared (see bold values).

Additionally, the results for the Gauss method and the linear method are compatible within their respective error ranges, validating the compatibility of both methods. Furthermore, all intercalibration sums are compatible with zero within 1σ, which as well confirms the validity of the applied intercalibration methods.

The error for the individual asymmetry values is the error of the fit to the respective distribution. One notices that the asymmetries are not compatible with zero within 1σ. This is eventually a result of the coarse binning of the asymmetry histograms and the inaccuracies that therefore ensue when applying a fit.

Effect of the zenith angle

Since the intercalibration methods are applied to a data set taken on the Crab Nebula that was observed under an average zenith angle of 48°, the applicability of the methods for larger zenith angles are checked in the following.

As was explained in section 2.1.3, observations at large zenith angles result in a wider area on the ground being illuminated by Cherenkov light, with the light-pool being stretched in one dimension (see Figs. 2.4 and 2.5). Additionally, in section 3.2 it was found that the core resolution is significantly worse for observations at 50° zenith angle. It should therefore be tested, whether the size-distance asymmetry plots change for increasing zenith angle. This is indeed the case, as one can see by comparing the size-distance asymmetry plots of two Monte Carlo data sets with 20° and 50° zenith (see Figs. B.1 and B.2 in the appendix):
Whereas for 20° zenith, the majority of the events have a distance asymmetry close to zero, for 50° the size-distance asymmetry distributions shows a maxima with $a_d \neq 0$. One can see that CT1-CT3 is the only telescope pair whose size-distance asymmetry histogram has the same shape as at 20° zenith. This makes sense as the zenith in the simulations is orientated in the direction of CT4, stretching the core position distribution along the axis between CT4 and CT2. As a consequence of this, CT2 and CT4 on average reconstruct smaller impact distances whereas the impact distances for CT1 and CT3 increase on average compared to simulations with smaller zenith angles.

In order to be able to apply he discussed intercalibration methods to data sets with large zenith angles (like the Crab Nebula), they are slightly modified, thereby accounting for several systematic effects that were discussed in the last paragraph:

1. Due to the fact that more and more events have stereo angles $< 30°$ (see Fig. A.3), the cut on the stereo angle is loosened to $15° < \phi_{i,j} < 150°$.

2. For the linear method (see 4.1.4), only impact distances beyond the Cherenkov light-pool are accepted. For observations at 50° zenith, the radius of the light-pool is increased and therefore only events with $d_{i,j} > 230\,\mathrm{m}$ are included in the intercalibration.

3. For the Gauss method, the interval width (in which the size asymmetry distribution is evaluated and fitted) is doubled (to $|a_d| < 0.1$)). This is done in order to include the bulk of the events, that for some telescope pairs for large zenith angles is no longer located at $a_d \approx 0$.

The asymmetry values for all telescope pairs for phase1b simulations with varying zeniths angles can be found in table B.1. One notices differences of ± 0.01 of the single asymmetry values for increasing zenith-angles. Furthermore the different methods no longer give similar results for all telescope pairs. Its likely that these discrepancies stem from the skewed shapes of the size-distance asymmetry plots of some telescope pairs for large zenith angles (see Fig. B.2).

One can conclude that the intercalibration methods are still usable for data sets that were observed at larger zenith angles. One should keep in mind, however, that the systematical

error of the methods increases for increasing zenith angles, since the core positions on the ground are no longer distributed symmetrical around the center of the array but on average are closer to two of the telescopes. This leads to skewed shapes of the size-distance asymmetry plots respectively to increased size-distance asymmetries for some of the telescope pairs.

PKS 2155–304

	PKS 2155–304 (bigflare)		PKS 2155–304 (all runs)	
Telescope pairs	**linear method**	**Gauss method**	**linear method**	**Gauss method**
CT1-CT2	0.018 ± 0.006	0.021 ± 0.006	0.024 ± 0.002	0.023 ± 0.002
CT1-CT3	0.025 ± 0.007	0.038 ± 0.008	0.018 ± 0.002	0.018 ± 0.003
CT4-CT1	-0.066 ± 0.007	-0.055 ± 0.007	-0.032 ± 0.002	-0.029 ± 0.002
CT2-CT3	0.031 ± 0.006	0.021 ± 0.007	-0.004 ± 0.002	-0.004 ± 0.002
CT2-CT4	0.034 ± 0.007	0.033 ± 0.009	0.007 ± 0.002	0.009 ± 0.003
CT3-CT4	0.021 ± 0.007	0.021 ± 0.008	0.013 ± 0.002	0.013 ± 0.002
$\sum_{\text{interc.}}$	0.005 ± 0.013	0.008 ± 0.014	0.002 ± 0.004	0.002 ± 0.004

Tab. 4.3: Size-distance asymmetry values for the two PKS 2155–304 data sets for both the linear method and the Gauss method. The asymmetry values for each telescope pair were obtained according to the procedure described in section 4.1.4. $\sum_{\text{interc.}}$ was calculated according to (4.3).

After having checked the validity of the linear method and the Gauss method, these are now applied to two data sets of the VHE γ-ray source PKS 2155–304. The corresponding size-distance asymmetry histograms can be found in the appendix (Fig. B.4 and B.5 for the bigflare and Fig. B.6 - B.8 for the full data set). An overview of the results is displayed in table 4.3.

When comparing the results for the two data sets, one notices that the asymmetry values for the bigflare are overall larger than the asymmetries for the full PKS 2155–304 data set. This could very well be because of the fact that the full data set includes ten times more events than the bigflare data set. The asymmetries for the different telescope pairs for PKS 2155–304 are discussed in more detail when the asymmetries of the reconstructed energies have been evaluated in the upcoming section 4.2.

However, the fact that the intercalibration sums for both data sets are close to and compatible with zero, indicates that both intercalibration methods give coherent results.

Crab Nebula

For the Crab Nebula data set, the size-distance asymmetry histograms, the Gauss-distribution in the central impact distance bins and the linear profile plots can again be found in the appendix (Fig. B.9 - B.11).

	Crab Nebula	
Telescopes	**linear method**	**Gauss method**
CT1-CT2	0.009 ± 0.006	0.001 ± 0.005
CT1-CT3	0.003 ± 0.006	-0.001 ± 0.006
CT4-CT1	0.006 ± 0.006	-0.009 ± 0.004
CT2-CT3	0.009 ± 0.005	0.005 ± 0.004
CT2-CT4	0.012 ± 0.006	0.025 ± 0.005
CT3-CT4	-0.011 ± 0.005	0.008 ± 0.005
$\sum_{\text{interc.}}$	0.012 ± 0.012	-0.004 ± 0.01

Tab. 4.4: Size-distance intercalibration values and sum for the Crab Nebula, on the left for the **linear method**, on the right for the **Gauss method**.

Since the Crab Nebula was observed under a larger zenith angle (48° on average), the methods to quantify size-distance asymmetry in between telescopes were altered slightly according to the steps given in the discussion of large simulated zenith angles in the previous subsection.

As one sees in table 4.4, the asymmetries for the different telescope pairs are smaller than for both PKS 2155–304 data sets. They are compatible with zero within 1-2 σ. One notices that the asymmetries obtained by the Gauss and the linear method differ, which can be explained by the worse applicability of the methods to data sets with large zenith angles.

Overall, the conclusion drawn from the size-distance intercalibration for PKS 2155–304 can be confirmed: the asymmetries in the responses of the telescopes in H.E.S.S. are ≤ 0.05 (≤ 0.03 if excluding the bigflare data set).

In the next chapter the asymmetries obtained here are compared with asymmetries between the energies reconstructed by the individual telescopes. This allows to see the effect of the muon correction, that is applied during the energy reconstruction.

4.2 Energy intercalibration

In the last section, differences in the responses of the telescopes were investigated by evaluating the size-distance asymmetry of the different telescope pairs in H.E.S.S.. This was done in order to check whether one of the telescopes reconstructs showers differently than the other telescopes.

In this chapter one wants to examine whether the individual telescopes reconstruct different energies for the same shower. It was explained in section 2.3.5 that each telescope gives an energy estimate for an event based on the comparison of the reconstructed size and impact distance with energy lookup tables. When reconstructing the energy of real VHE γ-ray sources, a muon-correction factor is applied to this energy estimate. This is done to compensate for the different optical efficiencies of the telescopes. By evaluating asymmetries between the energy estimates of the different telescopes, and by comparing

these asymmetries to the size-distance asymmetries obtained in the previous section, one can estimate the effectiveness of the muon-correction.

4.2.1 Procedure

To quantify the difference between the reconstructed energy of two telescopes, one again scales the difference by the sum of the two energy values and defines the **energy asymmetry of telescope i and j** as:

$$\Delta E^{i,j}_{asym} = \frac{E_i - E_j}{E_i + E_j} \tag{4.5}$$

where E_i (respectively E_j) is the energy that was reconstructed by telescope i (telescope j). The energy asymmetry is compared with $E_{i,j}$, the arithmetic mean of the energies reconstructed by telescopes i and j.[3]

In order to gain an average energy asymmetry value for a telescope pair, one proceeds in similar fashion as for the size-distance intercalibration: Like in section 4.1, all telescopes

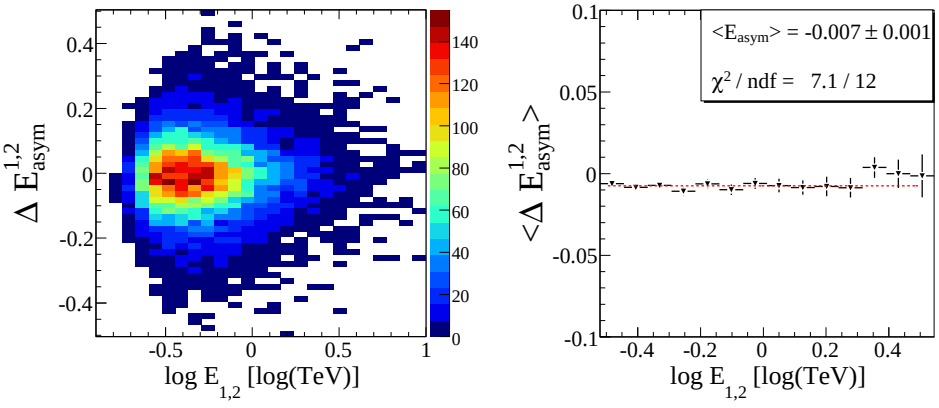

Fig. 4.7: *Left:* Distribution of energy asymmetries $\Delta E^{i,j}_{asym}$ (see equation 4.5) as a function of the mean energy $E_{i,j}$ for the telescope pair CT1-CT2 and the full data set of PKS 2155–304. *Right:* The same distribution averaged in each x-bin, with each data point corresponding to the mean of a Gauss fit in the respective bin. The fitted constant (dashed red line) is used to obtain $<E_{asym}>$, the energy asymmetry averaged over the whole energy range. This value is henceforth taken as $\overline{\Delta E_{i,j}}$, the energy asymmetry of the telescope pair.

are compared pairwise, which means there are six telescope-combinations that have to be evaluated. However, only events where all four telescopes triggered and all four telescopes passed standard cuts were taken for the energy intercalibration.

Energy asymmetries are only compared for the energy range: [300 GeV, 3 TeV] (i.e. [log(−0.5 TeV), log(0.5 TeV)] = [-0.5, 0.5]). As below 300 GeV systematic effects in the

[3] Weights that are used in the standard Hillas energy reconstruction of H.E.S.S. (see chapter 2.3.5), are not taken into account here when calculating $E_{i,j}$, because the energy asymmetry is unweighted, too.

energy reconstruction become dominant (see section 3.3), and for energies above a couple of TeV, event statistics of most gamma-ray sources become very sparse (due to their steep power-law), this energy range shows the most promise for the energy intercalibration attempted here.

The procedure to obtain an average value for the energy asymmetry of a telescope pair is illustrated in Fig. 4.7. Each selected event is filled into a two dimensional histogram with the energy asymmetry $\Delta E^{i,j}_{asym}$ as the ordinate and $\log(E_{i,j})$ as the x-axis (Fig. 4.7, left).

Then the energy asymmetry distribution in each $\log(E_{i,j})$ bin is approximated with a Gaussian. The fit is done using the likelihood-method (instead of the chi square-method), which is better suited for bins with small statistics. The mean value of the Gauss-fit is then taken and inserted into the same $\log(E_{i,j})$-bin in the corresponding profile plot (Fig. 4.7, right). The error of the mean value of the Gaussian in the specific bin is taken as the error for the data point. The event statistics in each bin of the two dimensional histogram have to be high enough so that a proper Gaussian can be fitted, thus only bins with more than 20 events were used. As a consequence, if there are bins without data points in the final energy asymmetry plots (Figs. C.1 - C.3), even though these bins lie within the energy range that was specified as accessible to H.E.S.S., this is due to lack of statistics in this bin.

If no large systematic effect is present, one expects the data points to have an energy asymmetry close to zero. Consequently, the energy asymmetry profile plot ought to be more or less horizontal. One fits a linear function $y(x) = const$ to the plot and obtains $y(0)$ as $\overline{\Delta E_{i,j}}$, the **energy asymmetry value** for the telescope pair i,j.

Finally, to check the consistency of the energy asymmetry values, one (in similar fashion as in (4.3)) defines the **energy intercalibration sum**:

$$\sum_{\text{E.int.}} = \overline{\Delta E_{1,2}} + \overline{\Delta E_{2,3}} + \overline{\Delta E_{3,4}} + \overline{\Delta E_{4,1}} \tag{4.6}$$

The errors of the intercalibration sum are calculated using standard error propagation rules. One again expects this sum to be 0 if there are no systematic errors in the energy intercalibration method.

4.2.2 Results of the energy intercalibration

Monte Carlo simulations

As for the size-distance intercalibration, the method for the energy intercalibration is first tested using Monte Carlo simulations.

Two simulated data sets are compared: on the one hand Monte Carlo simulations[4] with 0.5° offset and 0° zenith are used, on the other hand similar simulations that only differ in the sense that they were simulated under 50° zenith, instead. As this intercalibration

[4]From here on, only simulations from phase1b are used.

method is again applied to the Crab Nebula data set, it is important to look for zenith angle-related systematics.

As one sees in table 4.5, the energy asymmetries for the data set with 50° zenith angle hardly differ from the asymmetry values of the data set with 0°. Thus one can assume that - in contrast to the size-distance intercalibration - the zenith-related systematics are negligible for the energy intercalibration.

Telescope pairs	0° **zenith** (±0.0003)	50° **zenith** (±0.0003)
CT1-CT2	-0.0001	0.010
CT1-CT3	-0.001	-0.000
CT4-CT1	-0.004	-0.007
CT2-CT3	-0.001	-0.010
CT2-CT4	0.004	-0.003
CT3-CT4	0.004	0.007
$\sum_{\text{E.int.}}$	0.0001 ± 0.0006	0.0004 ± 0.0006

Tab. 4.5: Energy intercalibration asymmetry values $\overline{\Delta E_{i,j}}$ for two sets of Monte Carlo simulations: one with 0° zenith, the other with 50° zenith angle. $\sum_{\text{E.int.}}$ was calculated according to (4.6).

PKS 2155–304

The energy intercalibration method is now applied to both bigflare- and full data set of PKS 2155–304.

The respective energy asymmetry values are displayed in table 4.6. The corresponding energy asymmetry profile plots can be found in the appendix (Fig. C.1 and C.2, respectively).

As expected, the energy asymmetries are smaller than the size-distance asymmetries (see table 4.3), which most likely results from the muon-correction. The asymmetry values for the bigflare data set are again larger than the asymmetries obtained from the full PKS 2155–304 data set. Again, the difference in statistics, i.e. the fact that the full data set includes 10 times more events, is most likely contributing to this.

However, one notices, that for the bigflare data set, the asymmetry values for all pairs involving CT4 are particularly high $(0.02 - 0.03)$ compared to the other asymmetries in this data set. Since this behaviour is not visible for the full data set, it is likely that the deviating energy of CT4 is the result of some geometry-related asymmetry in the bigflare runs.

One possible interpretation would be that the reduced energy of CT4 in these runs is due to the wobble offset (see 2.2.2): in order to get background regions observed under the same offset as the source, the array takes runs under offsets of 0.5°, shifting the direction of that offset by 90° with each run. Since the bigflare data set consists only of three runs,

Telescope pairs	PKS 2155–304 (bigflare)	PKS 2155–304 (all runs)
CT1-CT2	0.004 ± 0.003	-0.008 ± 0.001
CT1-CT3	0.010 ± 0.004	-0.015 ± 0.001
CT4-CT1	-0.030 ± 0.003	0.003 ± 0.001
CT2-CT3	0.008 ± 0.003	-0.007 ± 0.001
CT2-CT4	0.025 ± 0.004	0.005 ± 0.001
CT3-CT4	0.018 ± 0.004	0.012 ± 0.001
$\sum_{\text{E.int.}}$	0.0002 ± 0.007	0.001 ± 0.002

Tab. 4.6: Energy asymmetry values $\overline{\Delta E_{i,j}}$ for two PKS 2155–304 data sets: the bigflare data set and the full data set. $\sum_{\text{E.int.}}$ was calculated according to (4.6). Std cuts were applied.

the wobble offset was only orientated into three out of four possible directions, thereby causing one direction (the one in which CT4 is located) to be disadvantaged. In the full data set, equal amounts of runs with all four wobble directions are included, which would explain why the deviating behaviour of CT4 is not visible there.

Crab Nebula

The results for the energy intercalibration using the Crab Nebula data set can be found in table 4.7. The asymmetry values are taken from the fits in the energy asymmetry plots in C.3 (appendix). The individual asymmetry values in the table differ from the ones obtained for PKS 2155–304. This may be due to the different average zenith angle under which the Crab was observed ($\simeq 48°$ for the Crab compared to $\simeq 20°$ for PKS 2155–304) or to the fact that the bulk of the Crab data was taken in another period of H.E.S.S.'s lifetime than the majority of the PKS 2155–304 events. One does not notice a deviating behaviour of the asymmetries of the pairs involving CT4, though.

Telescope pairs	Crab Nebula
CT1-CT2	-0.022 ± 0.002
CT1-CT3	-0.013 ± 0.002
CT4-CT1	0.006 ± 0.002
CT2-CT3	0.012 ± 0.002
CT2-CT4	0.017 ± 0.002
CT3-CT4	0.008 ± 0.002
$\sum_{\text{E.int.}}$	0.004 ± 0.004

Tab. 4.7: Energy asymmetry values $\overline{\Delta E_{i,j}}$ for the Crab Nebula (that was observed under an average offset of $\sim 48°$ zenith). $\sum_{\text{E.int.}}$ was calculated according to (4.6). Standard cuts were applied.

One can conclude that the energy asymmetries in between the telescopes are overall smaller than the asymmetries in the responses obtained from the size-distance intercalibration. This confirms the functioning of the muon correction. Minor asymmetries

between the individual energy estimates of the telescopes remain, yet these are only of the order < 0.02.

4.3 Relative energy calibration

In this section, the deviation of the energy estimates of the respective telescopes from the energy that is reconstructed by the whole array is quantified. The trends obtained from this relative energy calibration are closely connected to the results from the energy intercalibration asymmetries: the same quantities (i.e. the single telescope energies) are compared. Thus, asymmetries that were present in the energy intercalibration are visible in the results of the relative energy calibration and vice versa. Still, the relative energy calibration allows to view the results under a new angle, namely one is able to quantify the relative uncertainty in the energy reconstruction of each telescope.

4.3.1 Obtaining the relative energy uncertainty

In the following, one investigates the difference of the single telescope energies, E_i, and the arithmetic mean of the energy estimates of the four telescopes, $E_{1,2,3,4}$. As an intuitive display of the deviation between the two values, one chooses a modification of the already discussed energy bias (see 3.3): only instead of E_{MC}, the true energy of the event (which of course is only available for simulations), one takes $E_{1,2,3,4}$, i.e. E_{all}, and instead of E_{Rec} one chooses E_i. One consequently investigates the **relative energy uncertainty**

$$\Delta E_i = \frac{E_i - E_{1,2,3,4}}{E_{1,2,3,4}} \tag{4.7}$$

as a function of $\log(E_{1,2,3,4})$.

The same energy range as in 4.2.1 is taken to investigate the relative energy calibration. The event selection is identical to the one used in the energy intercalibration, too. The procedure to obtain the relative energy uncertainty (see 4.8) is similar to the one which was used to obtain the energy asymmetry value for a pair of telescopes in section 4.2.1: for each telescope, a two dimensional histogram is filled with the relative energy uncertainty as a function of $\log(E_{1,2,3,4})$ (see 4.8, left). The distribution in each $\log(E_{1,2,3,4})$-bin is then taken and fitted with a Gaussian. Again, the mean value of this Gaussian becomes the data point for this bin in the relative energy uncertainty profile plot (Fig. 4.8, right), whereas the error of the mean value of the Gaussian becomes its error (see D.2 in the appendix). Only bins with more than 20 events were taken for the profile plot - if a bin has no data point, this is due to the lack of statistics in the corresponding bin.

The mean relative energy uncertainty for telescope i, $\overline{\Delta E_i}$, is then obtained by fitting a horizontal line to the relative energy uncertainty plot. The y-bias of this line again yields $\overline{\Delta E_i}$ of telescope i.

As a cross check for the validity of the used method, one introduces the **relative calibration sum**:

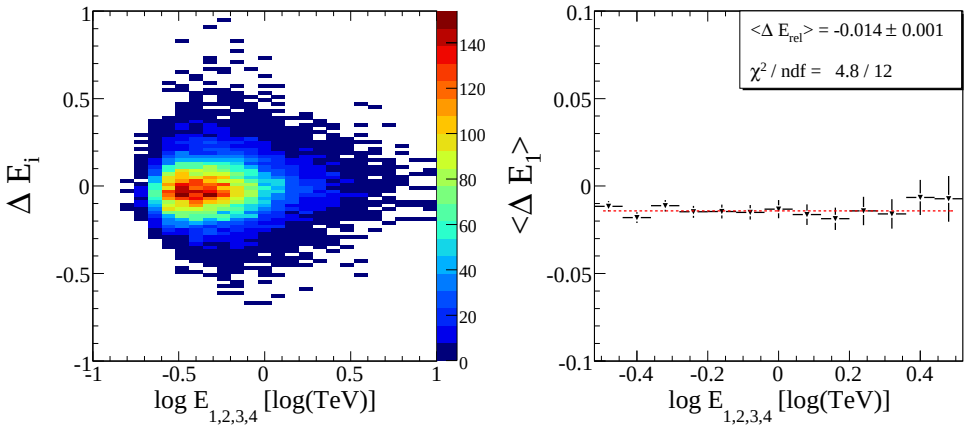

Fig. 4.8: *Left:* Distribution of relative energy uncertainties ΔE_1 (see equation 4.7) as a function of the energy reconstructed by all four telescopes $E_{1,2,3,4}$ for CT1 and the full data set of PKS 2155–304. *Right:* The same distribution averaged in each x-bin, with each data point corresponding to the mean of a Gauss fit in the respective bin. The fitted constant (dashed red line) is used to obtain $<E_{rel}>$, the relative energy uncertainty averaged over the whole energy range. This value is henceforth taken as $\overline{\Delta E_i}$, the relative energy uncertainty of the telescope.

$$\sum_{\text{E.rel.}} = \overline{\Delta E_1} + \overline{\Delta E_2} + \overline{\Delta E_3} + \overline{\Delta E_4} \tag{4.8}$$

One again expects the sum of the four relative energy uncertainty values to be zero if the applied method is working correctly.

4.3.2 Results of the relative energy calibration

The method is again applied to all three VHE γ-ray data sets that were already used in the previous sections.

PKS 2155–304

The relative calibration results for PKS 2155–304 are displayed in table 4.8. The corresponding relative energy uncertainty plots can be found in the appendix (Fig. D.1 and D.2). For the bigflare data set, one gets a confirmation for the deviating behaviour of CT4 in this data set: CT4 reconstructs a 3.5% lower energy compared to the energy reconstructed by the whole array. Like in the energy intercalibration, this effect vanishes once one takes the full PKS 2155–304 data set.

Telescope pairs	PKS 2155–304 (bigflare)	PKS 2155–304 (all runs)
CT1	0.019 ± 0.004	-0.014 ± 0.001
CT2	0.015 ± 0.004	0.003 ± 0.001
CT3	-0.001 ± 0.004	0.019 ± 0.001
CT4	-0.035 ± 0.004	-0.008 ± 0.001
$\sum_{\text{E.rel}}$	-0.002 ± 0.008	-0.001 ± 0.002

Tab. 4.8: Relative energy uncertainty values $\overline{\Delta E_i}$ for two **PKS 2155–304** data sets: the bigflare-data set and the full data set. $\sum_{\text{E.rel.}}$ was calculated according to (4.8). Std cuts were applied.

Crab Nebula

The results for the Crab Nebula data set can be found in table 4.9, the corresponding relative energy uncertainty plots in Fig. D.3. One again notices relative energy uncertainties of up to 2.5%.

Telescope	Crab Nebula
CT1	-0.026 ± 0.003
CT2	0.023 ± 0.004
CT3	$3.6 \cdot 10^{-9} \pm 1.9 \cdot 10^{-6}$
CT4	-0.007 ± 0.002
$\sum_{\text{E.rel}}$	-0.010 ± 0.005

Tab. 4.9: Relative energy uncertainty values $\overline{\Delta E_i}$ for the **Crab Nebula**. $\sum_{\text{E.rel.}}$ was calculated according to (4.8). Std cuts were applied.

4.3.3 Energy spread

In order to evaluate the impact of the relative energy uncertainty on the energy reconstruction, one is interested in how large the single telescope energies scatter around the averaged value obtained by all four telescopes, i.e. one determines a somewhat similar quantity as the energy resolution in section 3.4 (that obviously can only be determined for Monte Carlo simulations).

The energy spread is obtained by taking the width of the Gauss that was fitted to the distribution in each x-bin in the relative energy uncertainty plots (see Fig. 4.8, left). It serves to display how much the relative energy measurement can change due to statistical fluctuations. Fig. 4.9 displays the energy spread of Monte Carlo simulations for different cuts. One sees that the spread decreases with stricter event selection and is best for hard cuts, where it amounts to 12% for energies above 500 GeV. The reduced energy spread for smaller energies results from systematical effects, mirroring the overestimation of the reconstructed energy below the safe energy threshold due to a selection seffect (see 3.3).

As a next step, the energy spread for the full PKS 2155–304 data set using standard cuts is calculated. It is compared with simulations that were simulated under 0.5° offset and 20°

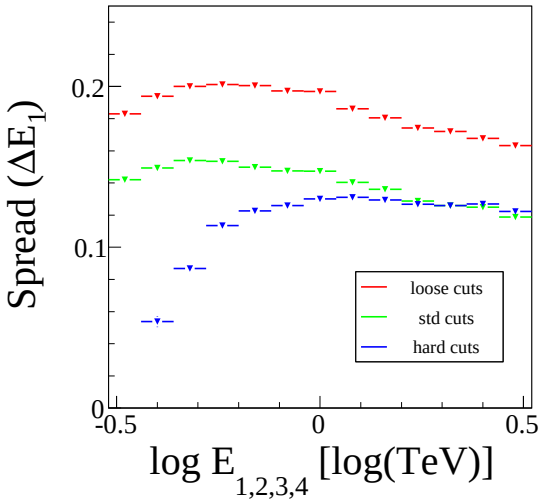

Fig. 4.9: Spread of the relative energy uncertainty of CT1 for loose, std and hard cuts (see section 2.3.4). As a data set, phase1b Monte Carlo simulations with 0.5° offset and 20° zenith were taken. The spread was calculated for loose, std and hard cuts.

zenith. The results are displayed in Fig. 4.10. One is able to make out a good agreement between simulations and data for small energies for all four telescopes. For energies above 900 GeV, the agreement worsens. This can be explained by the steeper power law of the VHE γ-ray source, i.e. the fraction of hadronic cosmic rays increases with energy in the PKS 2155–304 data set. As can be seen in Fig. 2.9, the camera images of hadron-induced showers cannot be properly approximated by a Hillas ellipse, which leads to a much larger uncertainty in the energy reconstruction for these events, i.e. an overall increase of the energy spread for the energy range where they become more dominant.

However, for energies < 1 TeV and standard cuts, the energy spread of the events from the PKS 2155–304 data set is of the order of 15%. If one compares this to the values obtained for the relative energy uncertainties earlier in this section, one sees that the asymmetries in between different telescopes are negligible for the overall energy reconstruction.

4.4 Time evolution of asymmetries

In the previous sections, the asymmetries based on all data collected on the respective sources during the operation time of H.E.S.S. were evaluated. Given the fact that the responses of the individual telescopes eventually have not been changing uniformly, it is interesting to evaluate the changes in asymmetry over time. Therefore, in this section, the evolution of the asymmetry values obtained in the previous three sections will be displayed and discussed. Once more, comparing the size-distance asymmetries and the energy asymmetry values allows to cross check the effectiveness of the muon-correction for different points in the life time of H.E.S.S..

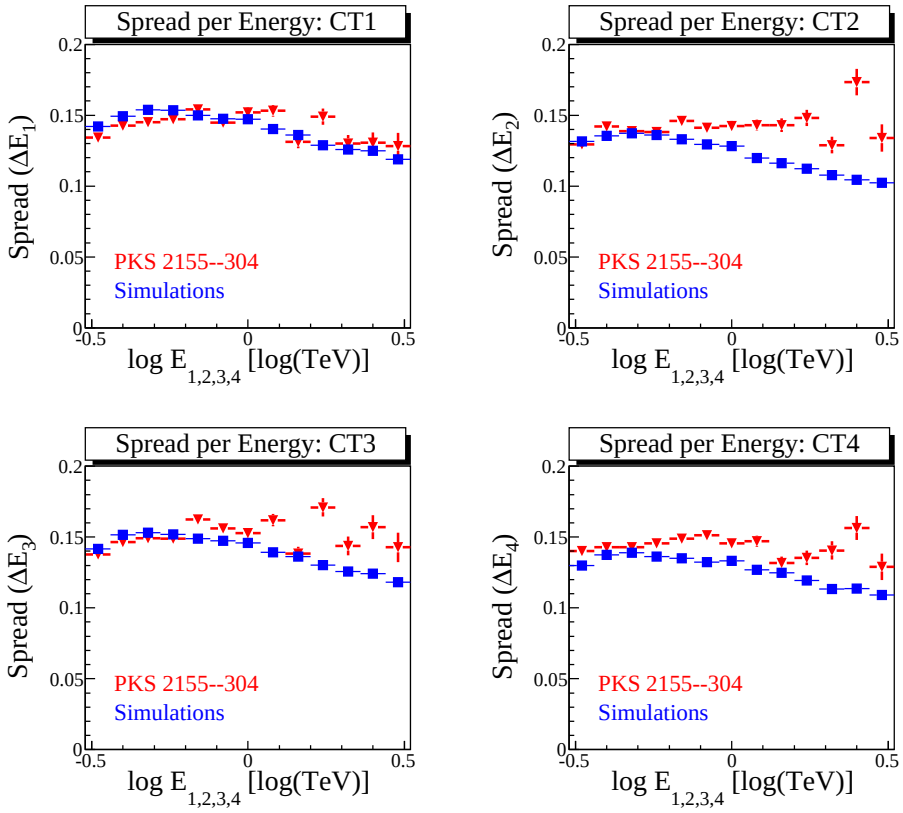

Fig. 4.10: Comparison of the spread of the relative energy uncertainty for phase1b Monte Carlos (0.5° offset and 20° zenith) and the full PKS 2155–304 data set. For both data sets std cuts were applied.

As a source for the investigation of the time evolution of the system, one takes the full data set taken on PKS 2155–304. This data set is most suitable for this section's purpose as it includes an abundance of VHE γ-ray events that were taken subsequently over the span of the last six years. The data set is divided into three two-year subsets, with more or less similar statistics (see table 4.10). In the following, the respective asymmetry values for all telescope pairs will be evaluated for the different subsets.

Time frame	**VHE γ-ray events**	**live time** [h]	**background** [%]
01/01/2004 - 31/12/2005	13569	64.7	31.4
01/01/2006 - 31/12/2007	42609	77.8	10.5
01/01/2008 - 01/08/2009	11374	62.9	27.2

Tab. 4.10: Properties of the three subsets of the full PKS 2155–304 data set after applying standard cuts. The background was estimated according to: $1 - \frac{N_{excess}}{N_{total}}$

4.4.1 Time evolution of the size-distance asymmetry

The time evolution of the size-distance asymmetry values can be found in table 4.11. A visualisation of these results is shown in Fig. 4.11, where the values of the respective size-distance asymmetry values for four telescope pairs are plotted for each of the three time intervals. One can see that the size-distance asymmetries of the different telescope pairs increase over time. Yet still, even for the 2008/2009 - data set, the asymmetry values are within ±0.06.

The overall increase of the asymmetry values with time indicates that the optical efficiencies of the different telescopes do not decay uniformly. In the next section it will be checked whether this trend also prevails for the energy asymmetries.

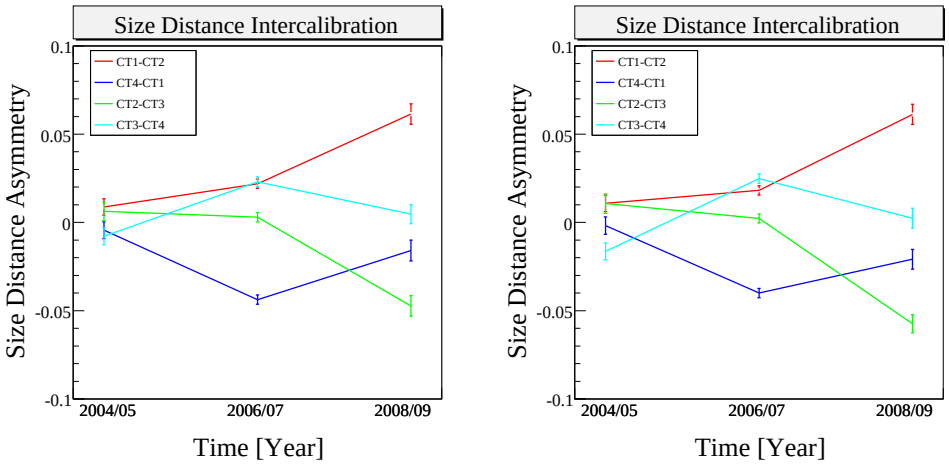

Fig. 4.11: Time evolution of the **size-distance asymmetry**, for both the linear method (left) and the gauss method (right). The respective values are taken from table 4.11. For clarity's sake, only the four telescopes pairs that are used for the intercalibration sum are displayed here.

Telescope	2004/2005	2006/2007	2008/2009
CT1-CT2	0.009 ± 0.005	0.022 ± 0.003	0.061 ± 0.006
CT1-CT3	0.021 ± 0.006	0.017 ± 0.003	0.022 ± 0.006
CT4-CT1	-0.004 ± 0.005	-0.044 ± 0.003	-0.016 ± 0.006
CT2-CT3	0.006 ± 0.005	0.003 ± 0.002	-0.047 ± 0.006
CT2-CT4	-0.015 ± 0.005	0.023 ± 0.003	-0.051 ± 0.006
CT3-CT4	-0.008 ± 0.005	0.022 ± 0.003	0.005 ± 0.005
$\sum_{\text{E.rel}}$	0.003 ± 0.010	0.004 ± 0.005	0.003 ± 0.011

Tab. 4.11: Time evolution for the **size-distance asymmetry values** $a_s^{i,j}$ (see 4.1.4).

4.4.2 Time evolution of the energy asymmetry

The time evolution of the energy asymmetry values can be found in table 4.12, with figure 4.12 being the corresponding visualization. One sees that - in contrast to the size-distance asymmetry values - the energy asymmetry values do not increase significantly with time. This indicates that the muon correction properly corrects the increasing deviation of the optical efficiencies for the different telescopes. Overall, the energy asymmetry values are < 0.02 for all times.

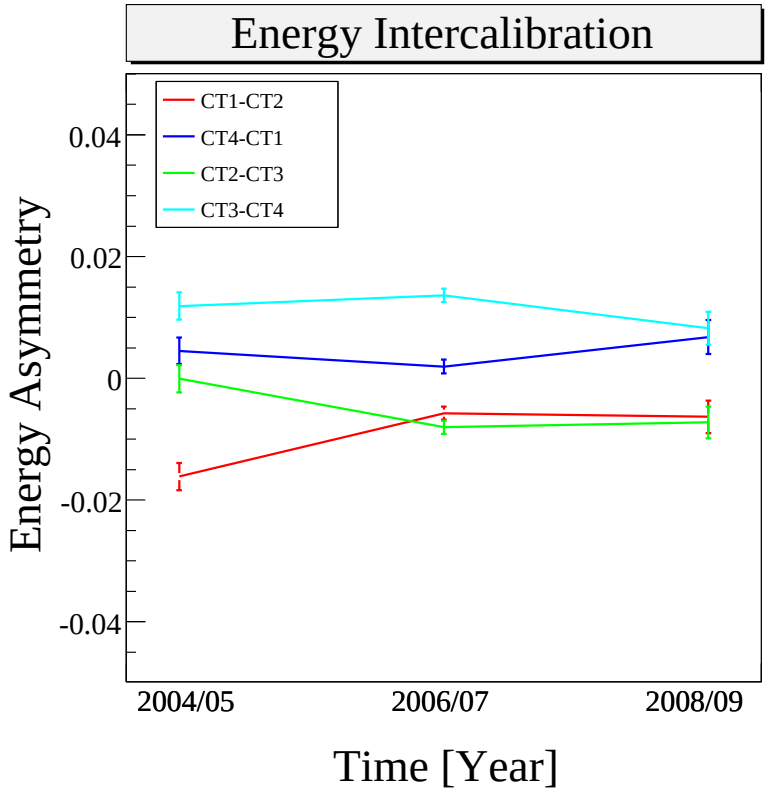

Fig. 4.12: Time evolution of the asymmetry values for the **energy intercalibration**. The respective values are taken from table 4.12. For clarity's sake, only the four telescope pairs that are used for the intercalibration sum are displayed here.

Telescope	2004/2005	2006/2007	2008/2009
CT1-CT2	-0.016 ± 0.002	-0.006 ± 0.001	-0.007 ± 0.003
CT1-CT3	-0.013 ± 0.003	-0.015 ± 0.001	0.015 ± 0.003
CT4-CT1	0.005 ± 0.002	0.020 ± 0.001	0.009 ± 0.003
CT2-CT3	-0.0001 ± 0.002	-0.008 ± 0.001	-0.008 ± 0.003
CT2-CT4	0.012 ± 0.003	0.004 ± 0.001	-0.001 ± 0.003
CT3-CT4	0.012 ± 0.002	0.014 ± 0.001	0.008 ± 0.003
$\sum_{\text{E.rel}}$	0.0001 ± 0.021	0.002 ± 0.017	0.002 ± 0.016

Tab. 4.12: Time evolution of the **energy asymmetry values** $\overline{\Delta E_{i,j}}$ (see 4.2.1).

4.4.3 Time evolution of the relative energy error

Finally, the time evolution of the relative energy uncertainty of the respective telescopes can be studied. The results for this check can be found in table 4.13 and Fig. 4.13. They confirm that the energy reconstruction of the individual telescopes did not get worse during the last five years. For the full PKS 2155–304 data set, the individual reconstructed telescope energies are within ±2% of the mean reconstructed energy for all time frames.

Telescope	2004/2005	2006/2007	2008/2009
CT1	-0.015 ± 0.003	-0.013 ± 0.001	-0.021 ± 0.004
CT2	0.013 ± 0.003	0.0001 ± 0.001	0.001 ± 0.003
CT3	0.015 ± 0.003	0.020 ± 0.001	0.015 ± 0.004
CT4	-0.013 ± 0.003	-0.008 ± 0.001	-0.001 ± 0.004
$\sum_{\text{E.rel}}$	-0.001 ± 0.028	-0.001 ± 0.025	-0.007 ± 0.026

Tab. 4.13: Time evolution of the **relative energy uncertainty** $\overline{\Delta E_i}$ (see 4.3).

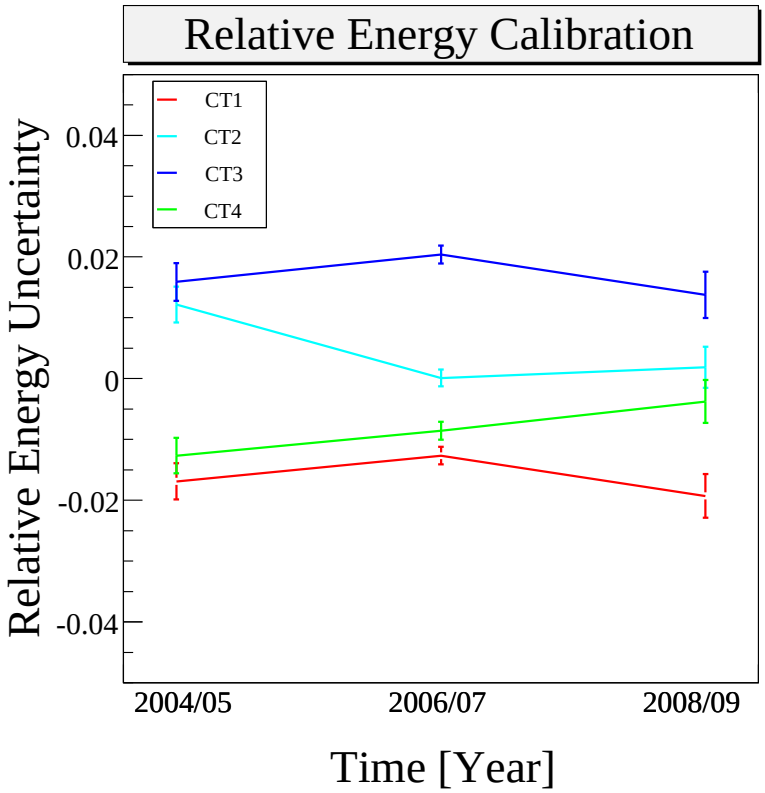

Fig. 4.13: Time evolution of the **relative energy uncertainty** values. The respective values are taken from table 4.13. For clarity's sake, only the four telescopes pairs that are used for the intercalibration sum are displayed here.

Overall, the results in this section confirm the functionality of the muon-correction: the trend of increasing asymmetries observed for the time evolution of the size-distance intercalibration is properly taken into account. The prevailing energy asymmetries are of

a negligible order of magnitude ($< 2\%$), confirming that the energy reconstruction of H.E.S.S. has not worsened over time.

4.5 Summary of the results

In this chapter the telescopes of H.E.S.S. were compared pairwise in order to see whether systematical effects worsen the geometry- or energy-reconstruction of individual telescopes. By applying different intercalibration methods to two bright VHE γ-ray sources, asymmetries in the responses of the telescopes were quantified. It was found that asymmetries in between the telescope responses exist, confirming that the optical efficiencies of the telescopes differ (see 4.1.5). However, these size-distance asymmetries (with one exception) are of the order of ≤ 0.03, i.e. equivalent to a relative difference of telescope responses of $< 6\%$.

By comparing these asymmetries (that reflect asymmetries in the shower reconstruction) with asymmetries in the energy reconstruction, conclusions about the effectiveness of the muon-correction were inferred. It was found that latter asymmetries are less pronounced than the size-distance asymmetries, indicating that the muon-correction is working properly and is able to reduce the deviation of the energy reconstructed by one telescope from the energy reconstructed by the whole array to $2-3\%$ (see 4.3.2). This effect is negligible when comparing it to the spread in single telescope energies around the mean value (15%, see 4.3.3) or the overall energy resolution of H.E.S.S. that is of the order of $17-24\%$ (see chapter 3.3).

The investigation of the time evolution of the asymmetries confirmed that this inaccuracy in the energy reconstruction has remained more or less constant since the H.E.S.S. experiment started taking data.

Overall one can conclude that up to date, there are no major systematical effects within the shower- or the energy-reconstruction stemming from differences in the H.E.S.S. telescopes. Minor systematic effects in between telescopes are present, but are about one order of magnitude smaller than the already known systematical effects in the energy reconstruction.

Chapter 5

Conclusion and Outlook

H.E.S.S. is an array of four Imaging Atmospheric Cherenkov Telescopes that is used to detect very high energy ($> 100\,\mathrm{GeV}$) photons. By observing these VHE γ-rays, some of the most energetic processes in the universe can be investigated. One of the prime agendas of H.E.S.S. is to help unraveling the origin of the cosmic rays, that are likely accelerated in the shock-waves of supernova remnants. In this and many other physical contexts the highest possible accuracy in the reconstruction of the energy spectrum of VHE γ-ray emitters is crucial in order to interpret the observational results.

H.E.S.S. detects VHE γ-rays by observing the Cherenkov light of atmospheric air showers that were induced by VHE-particles. The reconstruction of the primary particle's energy harbors systematic uncertainties, that limit the spectral resolution of the experiment. The objective of this work was to investigate the current accuracy of the energy reconstruction of H.E.S.S.. This investigation was carried out in two steps:

The **overall systematics and energy reconstruction** were investigated by testing the Hillas standard analysis with Monte Carlo simulations. Special attention was paid to the influence of the multiplicity, i.e. the number of telescopes that participated in the reconstruction of the particle shower, on the accuracy of the event reconstruction.

It was found that the geometry reconstruction is less accurate for observations at large zenith angles. The core resolution, i.e. the average scattering of the reconstructed core distances around the simulated value, amounts to $\simeq 62\,\mathrm{m}$ for showers observed at a zenith angle of 50°, whereas for observations at 20° zenith, a much better core resolution of $\simeq 13\,\mathrm{m}$ is obtained. This worse resolution for large zenith angles can be explained by a on average larger distance between the telescope array and the shower maximum.

The higher inaccuracy of the core reconstruction for observations at 50° zenith angle has no significant effect on the error of the energy reconstruction. However, one notices a worsening of the energy reconstruction at large zenith angles for two- and three-telescope events. This can be explained by a significant reconstruction error in the geometry reconstruction of a fraction of events with impact distances $> 400\,\mathrm{m}$ that propagates to an error of $> 400\%$ in the energy reconstruction.

A cut on the core distance or small stereo angles would exclude these events from the analysis and thereby the energy reconstruction under large zenith angles using only two

or three telescopes could eventually be improved. However, further systematical studies are required to investigate all effects of such a cut.

As a next step, the overall energy resolution of H.E.S.S. for observations at 20° and 50° zenith angle was determined and found to be $\simeq 17\%$ and $\simeq 23\%$, respectively. Whereas the first value agrees quite well with systematical studies carried out in the past ([10]), the energy resolution for 50° zenith angle obtained in this work is 5% larger, again due to the large error in the core reconstruction for events with lower multiplicity. When only taking four-telescope-events, the energy resolution for observations at 50° zenith angle increases to $\simeq 18\%$, which is in agreement with the previous studies.

Then, the **event reconstruction of the individual telescopes** based on the H.E.S.S. data on the VHE γ-ray sources PKS 2155–304 and the Crab Nebula was compared. By applying an intercalibration method it was investigated if there are systematic differences between the event reconstruction of the different telescopes. Furthermore, it was determined whether possible asymmetries between telescopes have an effect on the energy reconstruction.

It was found that the asymmetries between responses of different telescopes are $< 10\%$. Regarding the energy estimates of the individual telescopes, the asymmetries are less pronounced, confirming the functioning of the muon correction. The overall differences between the energy estimates of the single telescopes and the energy reconstructed by the whole array are $< 4\%$. Additionally, the time evolution of the asymmetries was monitored (see 4.4). Whereas the differences in the telescope responses have increased in the last five years, the energy asymmetries have remained constant, which further underlines the functioning of the muon correction.

It can be concluded that no significant systematics result from the differences between the individual Cherenkov telescopes of H.E.S.S.. Minor differences are present, but these have no significant impact on the energy reconstruction since they are an order of magnitude smaller than the overall energy resolution of the experiment.

In 2010, the mirrors of CT3 will be replaced, similar replacements are foreseen for the other telescopes following in a time frame of 1-2 years. The new mirrors will increase the optical efficiency of the respective telescopes significantly. Until the mirrors of all telescopes are replaced, this will eventually introduce significant asymmetries in the telescope responses. It will be interesting to repeat the systematical studies performed in this work in order to see whether the muon correction adequately corrects much more severe asymmetries than those present in today's system.

In the near future, H.E.S.S. phase II will be completed, for which a significantly larger, fifth Cherenkov telescope with a total mirror area of $600\,\mathrm{m}^2$ will be added to the centre of the array. The intercalibration of the array with this fifth telescope will be challenging, given its different size and properties. Eventually adapted versions of the methods presented in this thesis will be appliciable to the new setup as well.

With H.E.S.S. II, the sensitivity of the instrument will increase and showers of lower energies will be detectable. This will enable H.E.S.S. to delve even deeper into the mysteries of the non-thermal universe.

Appendix A

Stereo Angle

The stereo angle of a telescope pair is the angle under which the axes of two Hillas ellipses intersect (see 2.3.2). It is obtained from the orientations of the two images in the corresponding cameras ($[0°, 360°]$), which are measured counterclockwise, starting in x-direction.[1] The determination of the stereo angle is visualised in Fig. A.1. The difference of the two Hillas image orientations gives the intersection angle of the two image axes. This definition is ambiguous, though, since for some orientations of the image axes, the difference between the two image orientation angles is $> 180°$ and one can obtain the stereo angle by substracting the difference from 360°.

Consequently, $\phi_{i,j}$, the stereo angle of telescope i and j is calculated according to:

$$\begin{array}{ll} \phi_{i,j} = |\theta_i - \theta_j| & (\text{for} \quad |\theta_i - \theta_j| <= 180\,°) \\ \phi_{i,j} = 360\,° - |\theta_i - \theta_j| & (\text{for} \quad |\theta_i - \theta_j| > 180\,°) \end{array} \tag{A.1}$$

where θ_i (θ_j) is the Hillas image orientation of telescope i (j). This definition is unambiguous.

This definition is motivated by Fig. A.1 and Fig. A.2. It is also noteworthy that the abundance of certain stereo angle values depends on the zenith angle under which events are observed. The stereo angle distribution for different sets of Monte Carlo simulations with varying zenith angle is displayed in Fig. A.3. One sees that for larger zenith angles, more and more events are reconstructed with small stereo angles. This mirrors the fact that the Cherenkov light-pool radius on the ground is larger than for observations at zenith and consequently more and more events have core positions that lie outside of the array. The corresponding impact distances are large and the image axes intersect at small angles.

[1] The image orientations, like all Hillas parameters, are determined in the nominal system, in which the four camera images are superimposed.

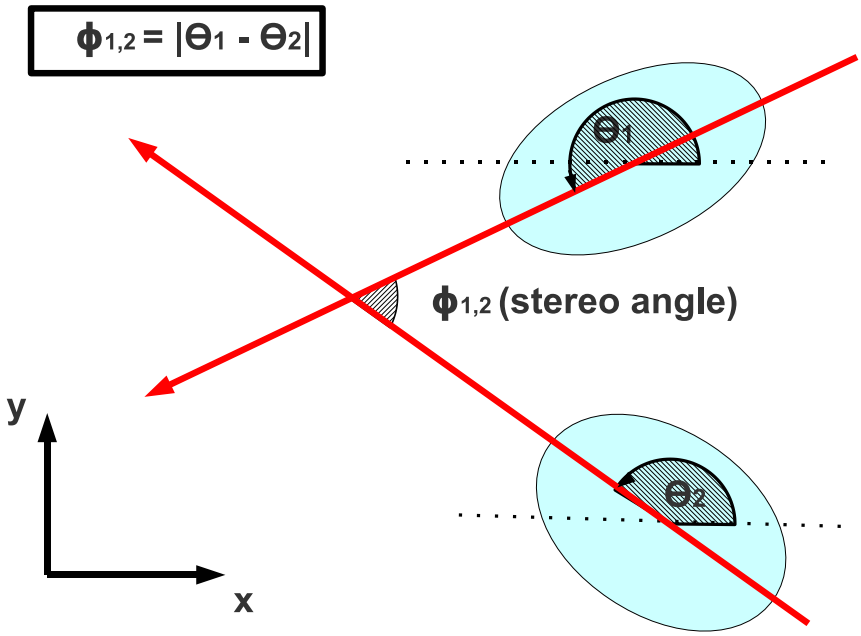

Fig. A.1: Intersection of the image axes of two Hillas ellipses in the nominal system. The difference of the Hillas image orientations ϕ_1, ϕ_2 is $< 180°$, thus the difference is taken as the stereo angle.

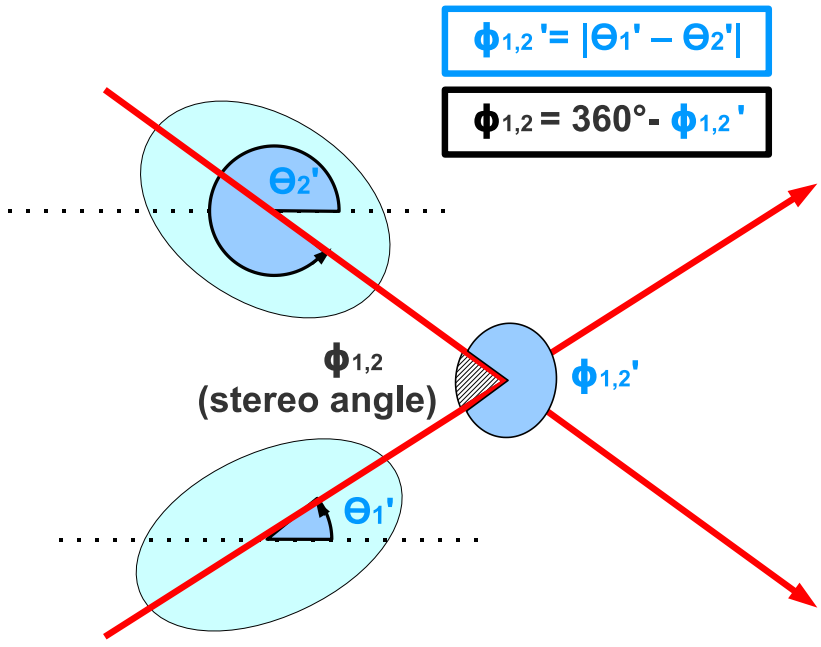

Fig. A.2: Intersection of the image axes of two Hillas ellipses in the nominal system. The difference of ϕ_1, ϕ_2 is $> 180°$, therefore one obtains the stereo angle by taking the complementary angle.

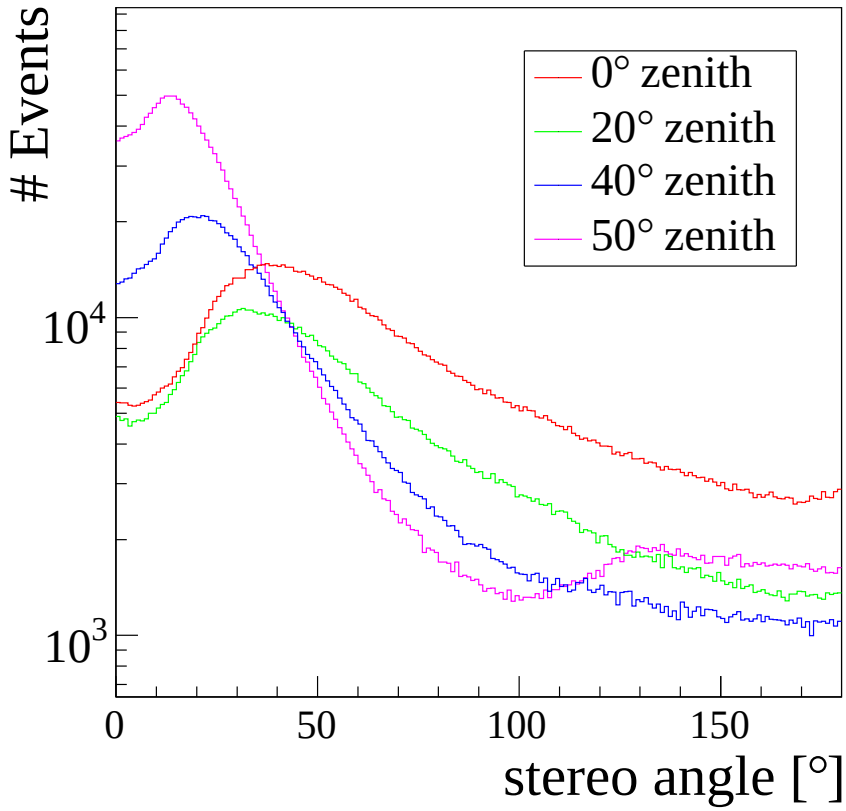

Fig. A.3: Stereo angle distribution for different zenith angles for Monte Carlo simulations with 0.5° offset.

Appendix B

Size-distance Intercalibration Plots

linear method			
Telescope pairs	20° **zenith** (±0.001)	40° **zenith** (±0.001)	50° **zenith** (±0.001)
CT1-CT2	0.006	-0.003	-0.002
CT1-CT3	0.001	0.000	0.002
CT4-CT1	0.008	0.001	0.000
CT2-CT3	-0.006	0.004	0.007
CT2-CT4	-0.016	-0.001	0.001
CT3-CT4	-0.011	-0.001	-0.003
$\sum_{\text{interc.}}$	-0.003 ± 0.002	0.001 ± 0.002	0.002 ± 0.002
Gauss method			
Telescope pairs	20° **zenith** (±0.001)	40° **zenith** (±0.001)	50° **zenith** (±0.001)
CT1-CT2	0.002	0.004	0.007
CT1-CT3	0.000	-0.001	0.002
CT4-CT1	0.002	0.008	0.010
CT2-CT3	0.001	-0.006	-0.006
CT2-CT4	-0.001	-0.009	-0.004
CT3-CT4	-0.004	-0.009	-0.011
$\sum_{\text{interc.}}$	-0.0005 ±0.0032	-0.002 ± 0.002	0.0002 ± 0.0019

Tab. B.1: Size-distance asymmetry values for phase1b Monte Carlos with 0.5° offset and **varying zenith angles**, for both the linear and the Gauss method.

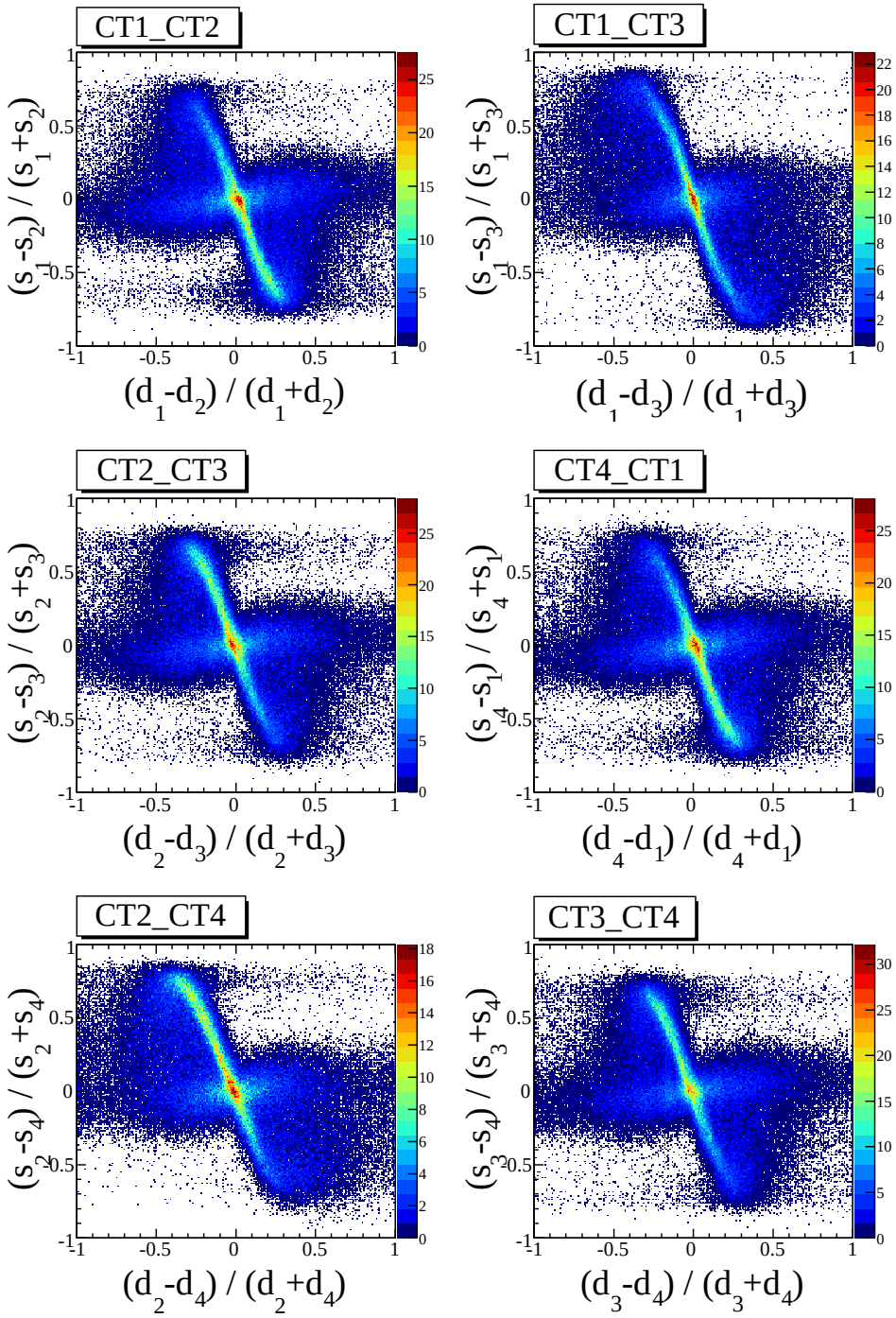

Fig. B.1: Size-distance asymmetry distributions for all telescope pairs for Monte Carlo simulations from phase1b with 0.5° offset and 20° zenith. No cut on the impact distance or the stereo angle was applied.

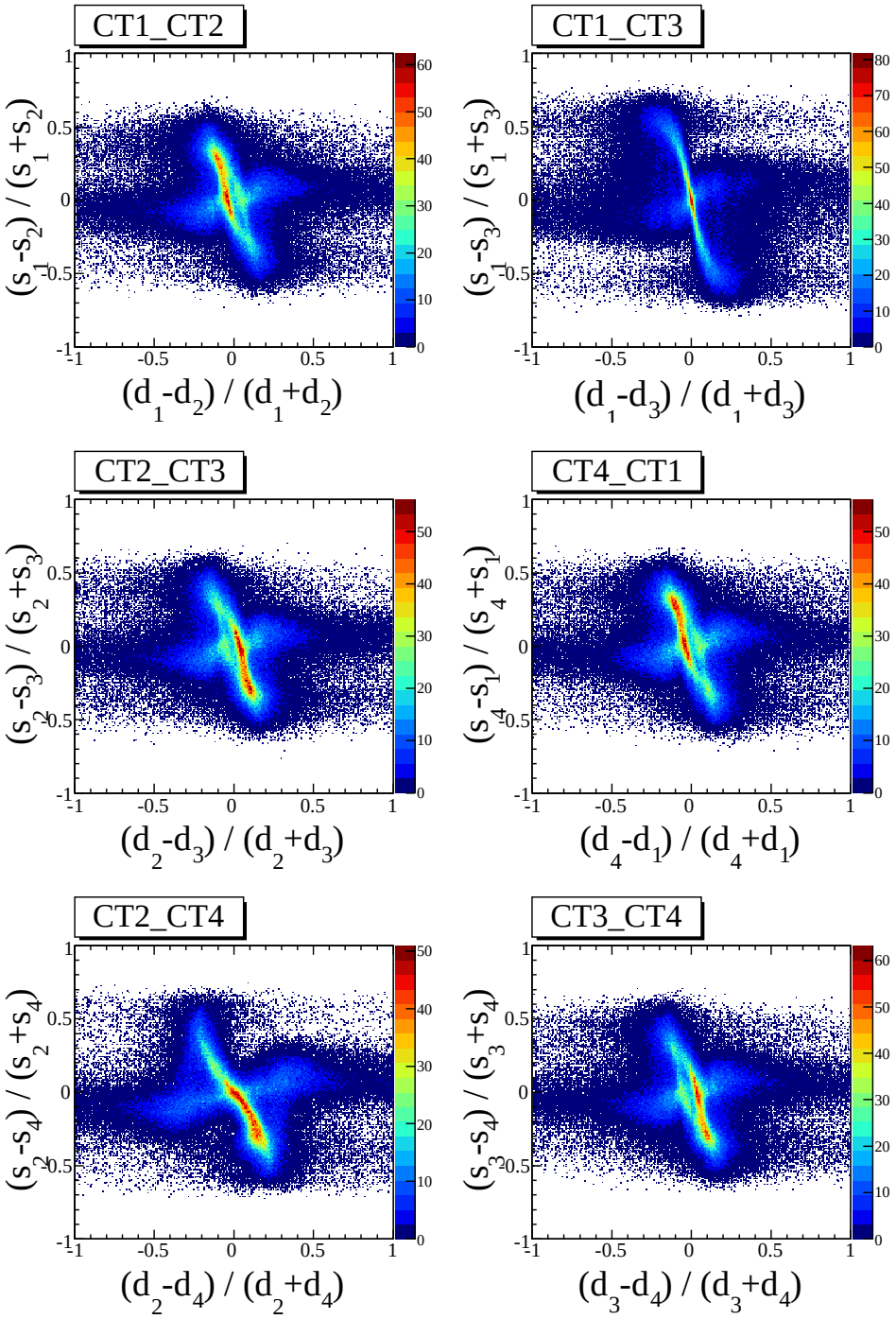

Fig. B.2: Size-distance asymmetry distributions for all telescope pairs for Monte Carlo simulations from phase1b with 0.5° offset and 50° zenith. No cut on the impact distance or the stereo angle was applied.

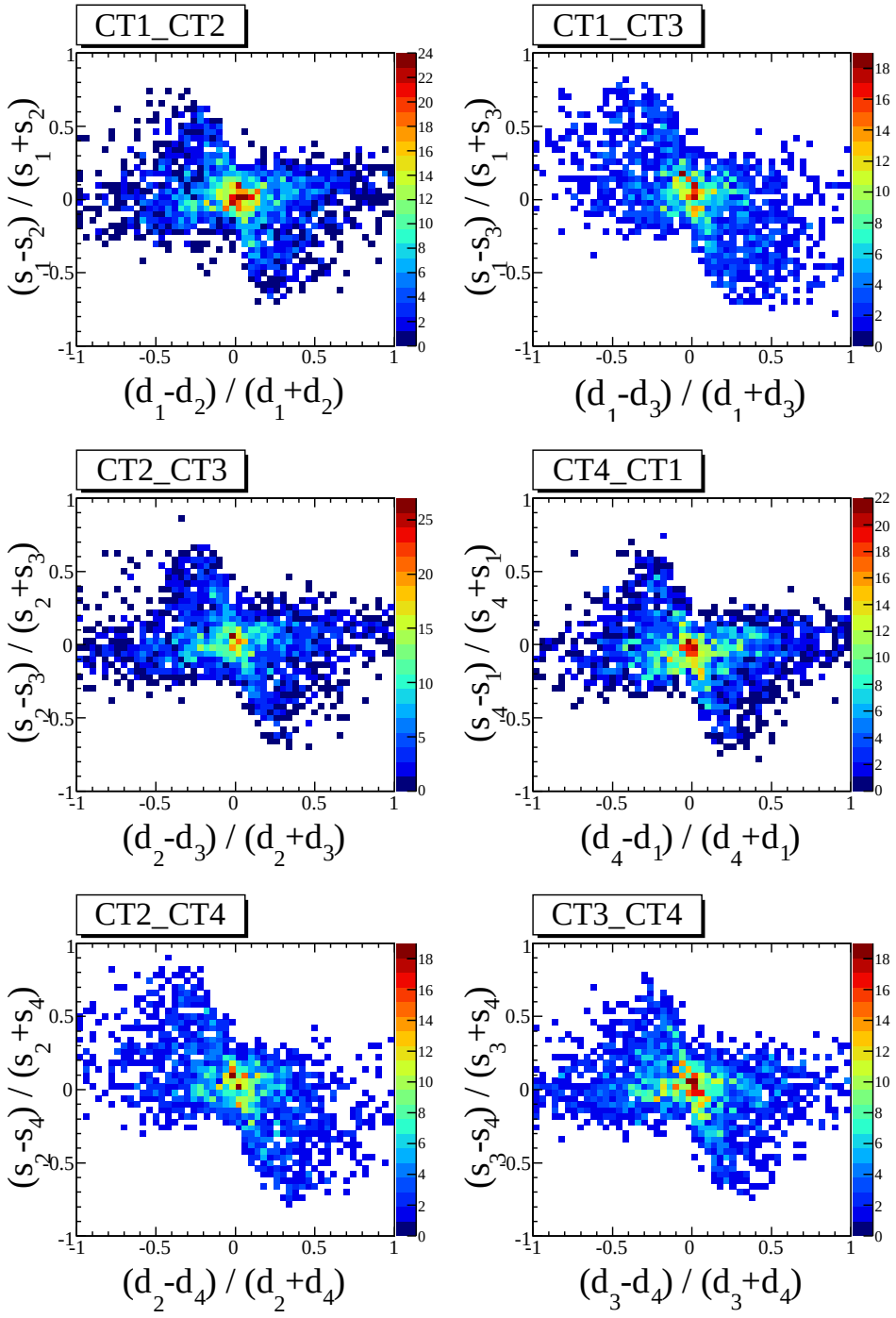

Fig. B.3: Size-distance asymmetry plots for all six telescope pairs for the **bigflare of PKS 2155–304**. All imact distances are included, hence on is able to make out the superposition of a horizontal and an anti-linear structure (see 4.1.3). On average, $\simeq 2300$ events were included in the each of the asymmetry plots (after applying std cuts).

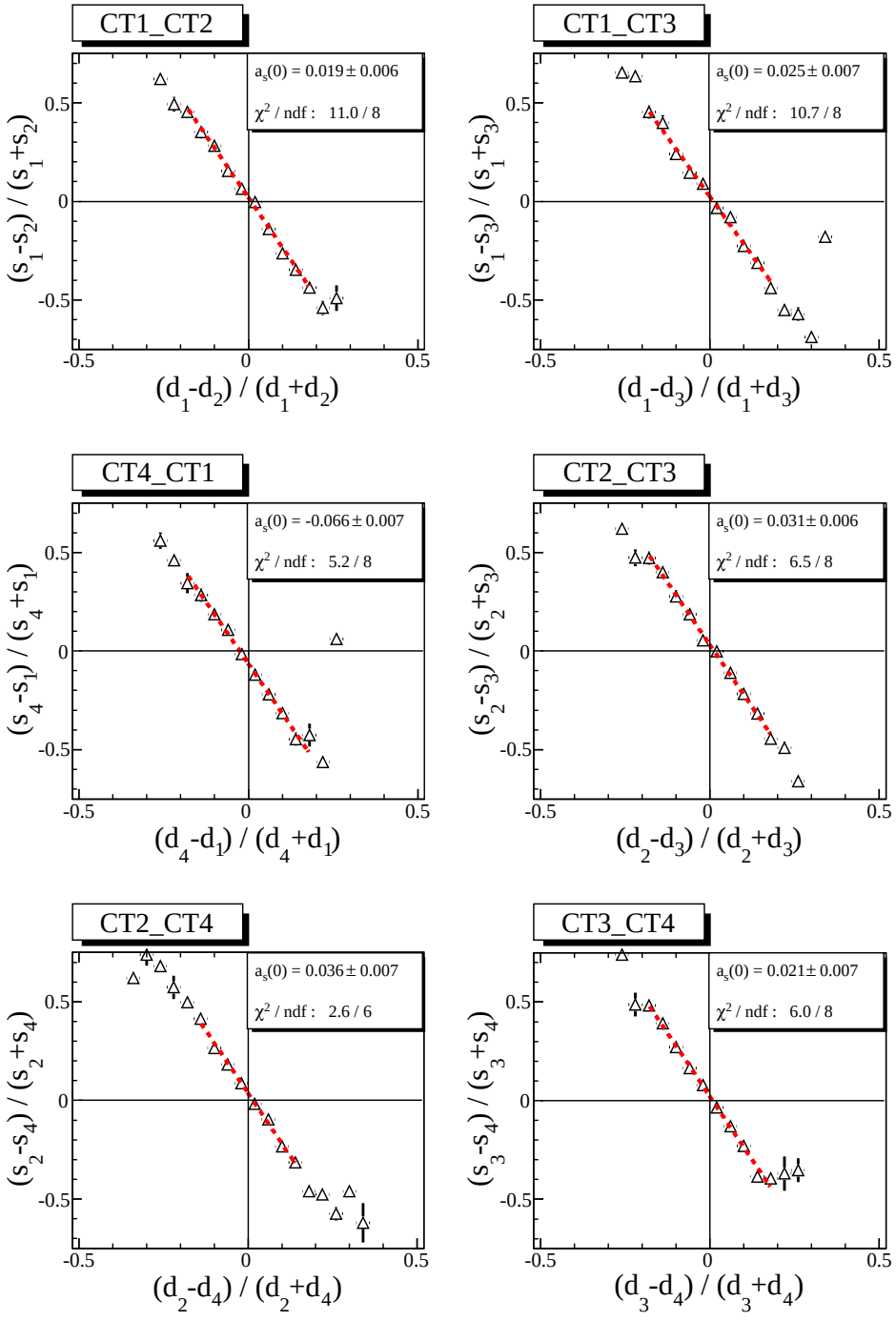

Fig. B.4: Distributions used for the **linear method** for the Size-distance asymmetry plots for all six telescope pairs using the **bigflare of PKS 2155–304** as a data set. Only impact distances $> 130m$ are included, hence the anti-linear structure (see 4.1.3). On average, $\simeq 400$ events were included in the plots (after applying std cuts). $a_s(0)$ denotes the intersection point of the linear fit (dashed red line) and vertical line at $x = 0$ and is taken as the intercalibration value for the specific telescope pair.

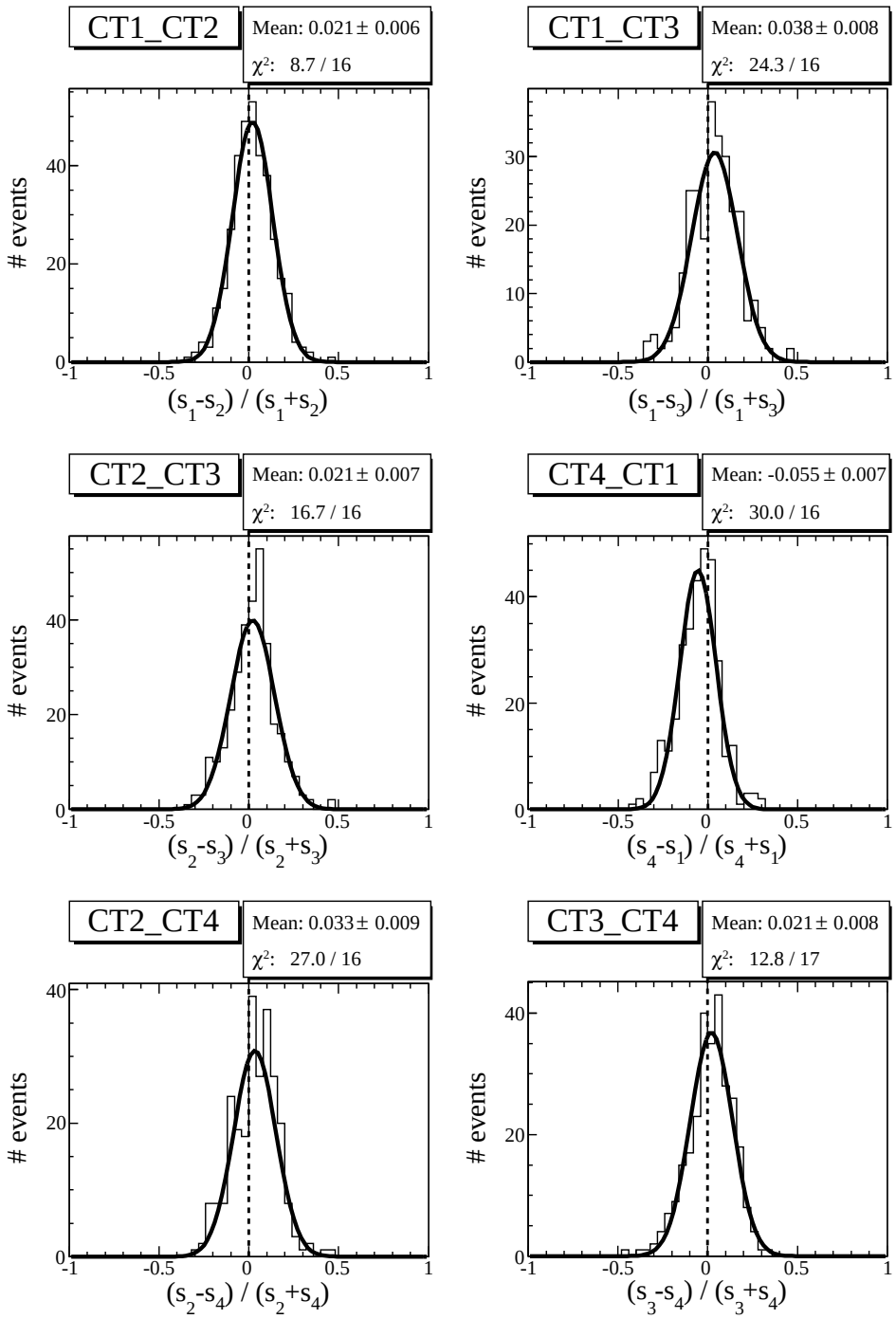

Fig. B.5: Distributions used for the **Gauss method** for the Size-distance asymmetry plots for all six telescope pairs for the **bigflare of PKS 2155–304** (runs 33746, 33747 and 33748). All impact distances are included, but only distance asymmetries whose absolute value is < 0.05. On average, $\simeq 300$ events were included in the plots (after applying std cuts). "Mean" denotes the mean value of the Gauss fitted to the distribution and is used as the intercalibration value for this telescope pair.

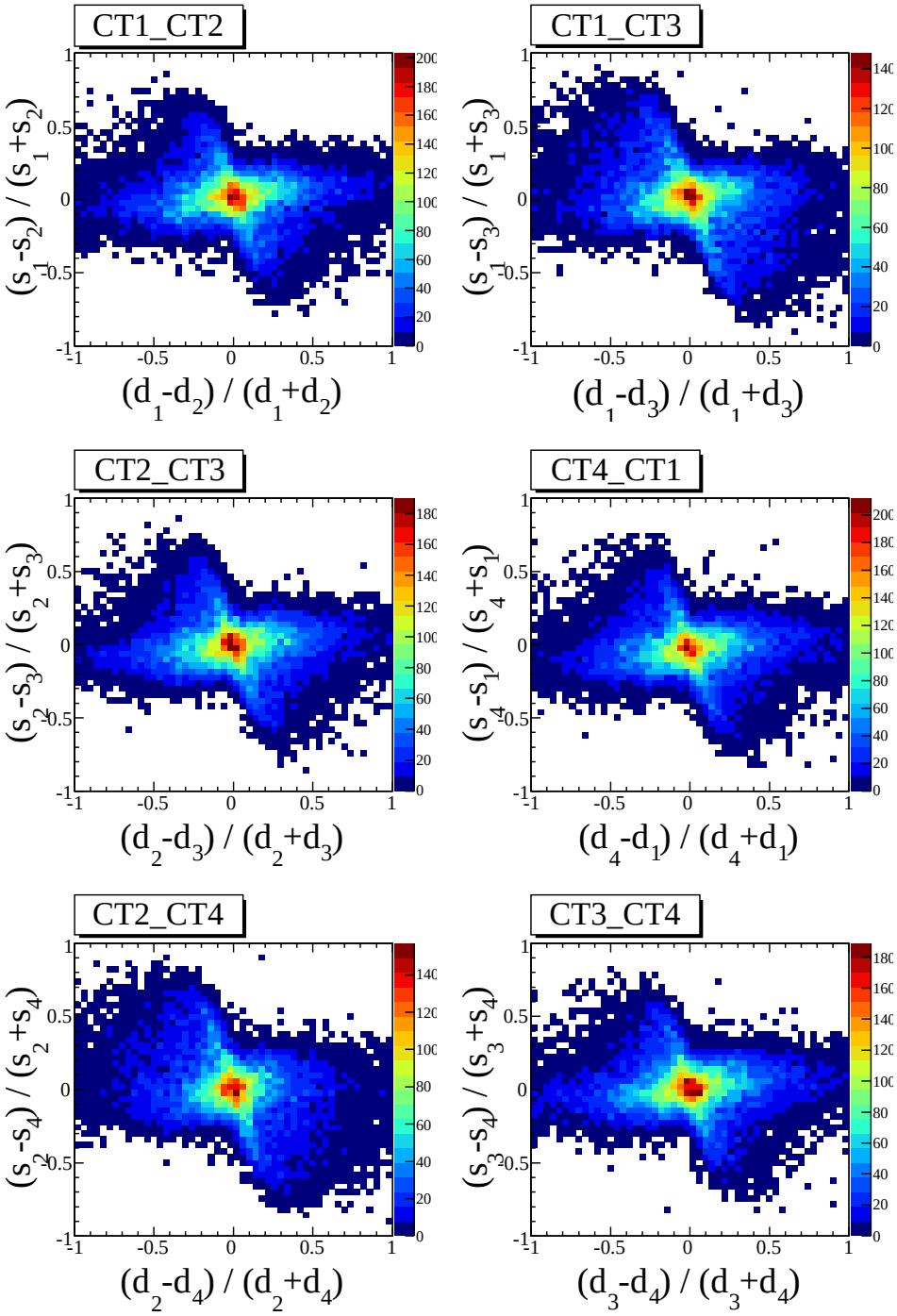

Fig. B.6: Size-distance asymmetry distributions for all six telescope pairs for the **full PKS 2155–304 dataset** (all 467 runs). All imact distances are included, hence on is able to make out the superposition of a horizontal and an anti-linear structure (see 4.1.3). On average, $\simeq$ 22500 events were included in the each of the asymmetry plots (after applying std cuts).

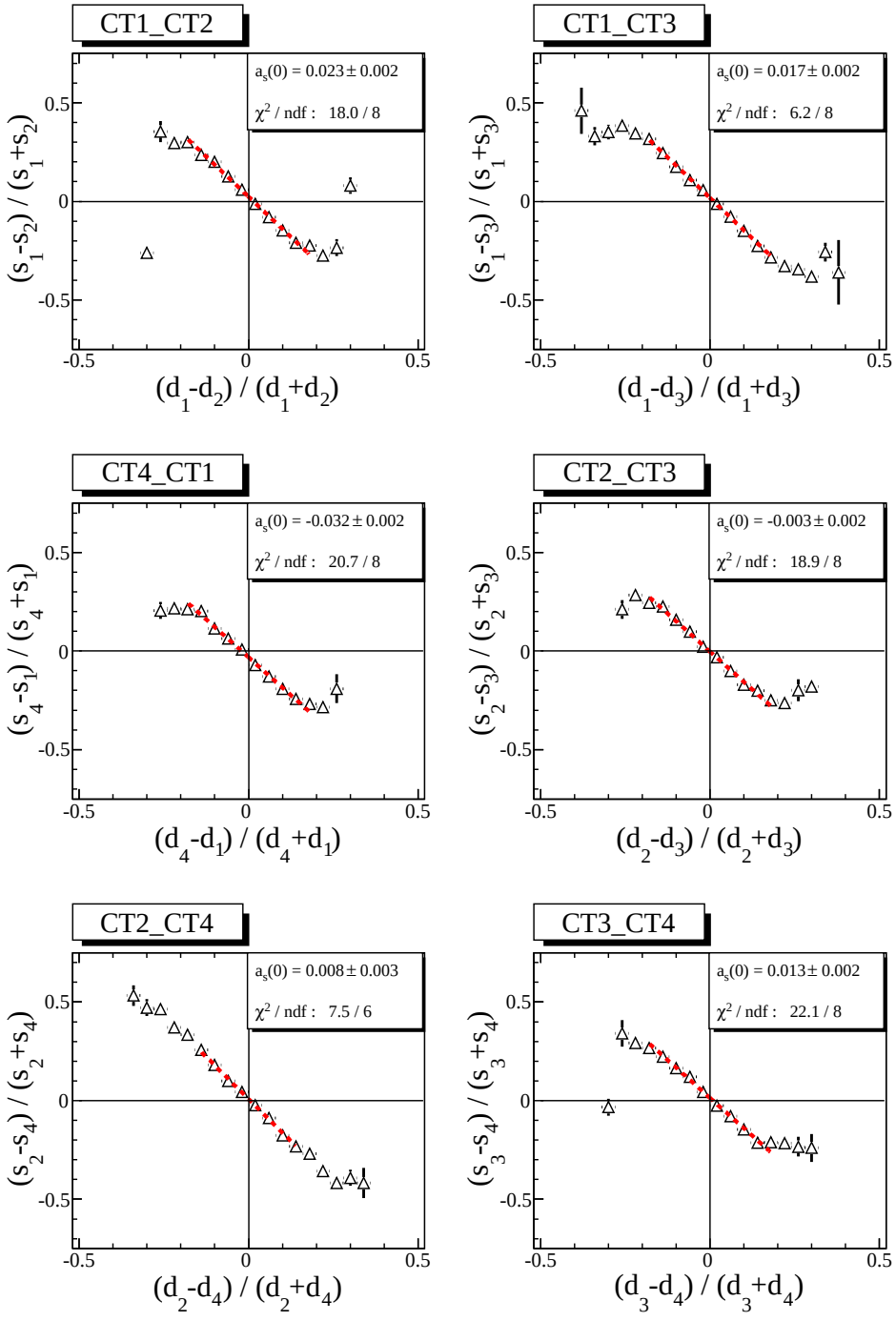

Fig. B.7: Distributions used for the **linear method** for the Size-distance asymmetry plots for all six telescope pairs for the **full PKS 2155–304 dataset** (all 467 runs). Only impact distances $> 130m$ are included, hence the anti-linear structure (see 4.1.3). On average, $\simeq 5500$ events were included in the plots (after applying std cuts). $a_s(0)$ denotes the intersection point of the linear fit (dashed red line) and vertical line at $x = 0$ and is taken as the intercalibration value for the specific telescope pair.

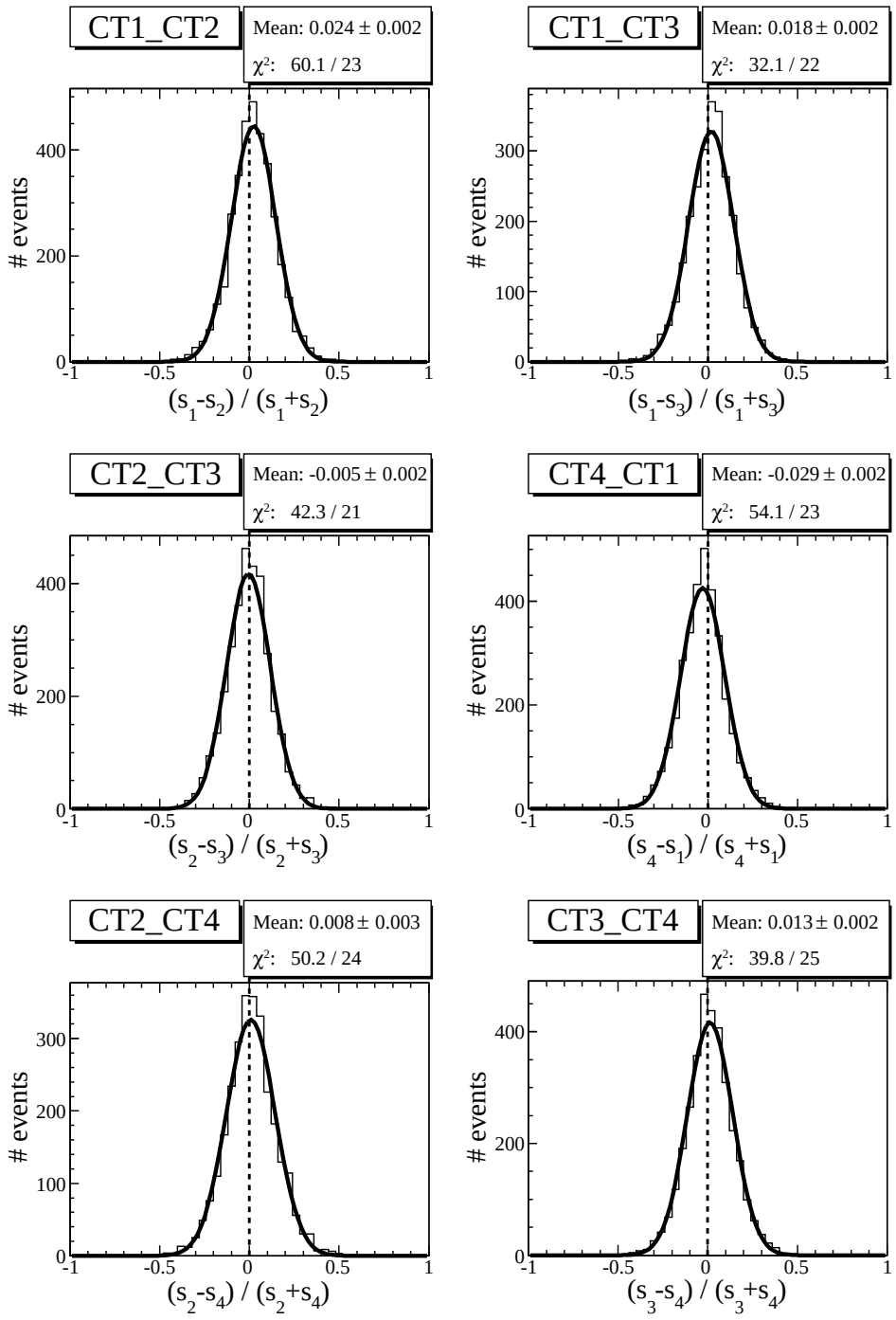

Fig. B.8: Plots used for the **Gauss method** for the Size-distance asymmetry plots for all six telescope pairs for the **full PKS 2155–304 dataset** (all 467 runs). All impact distances are included, but only distance asymmetries whose absolute value is < 0.05. On average, $\simeq 3500$ events were included in the plots (after applying std cuts). "Mean" denotes the mean value of the Gauss fitted to the distribution and is used as the intercalibration value for this telescope pair.

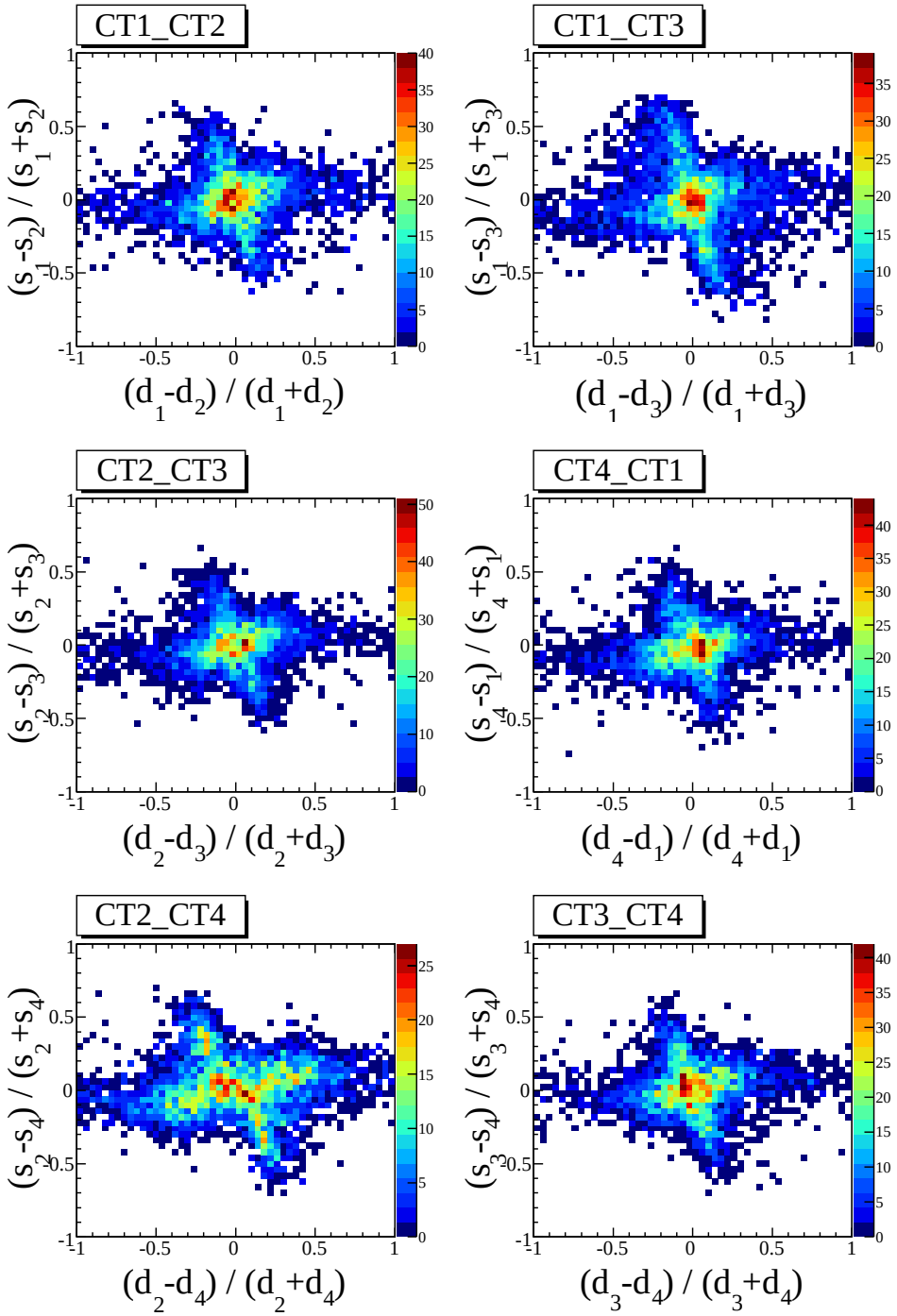

Fig. B.9: Size-distance asymmetry plots for all six telescope pairs for the full dataset taken on the **Crab Nebula** (52 runs). All imact distances are included, hence on is able to make out the superposition of a horizontal and an anti-linear structure (see 4.1.3). On average, $\simeq$ 4000 events were included in the each of the asymmetry plots (after applying std cuts).

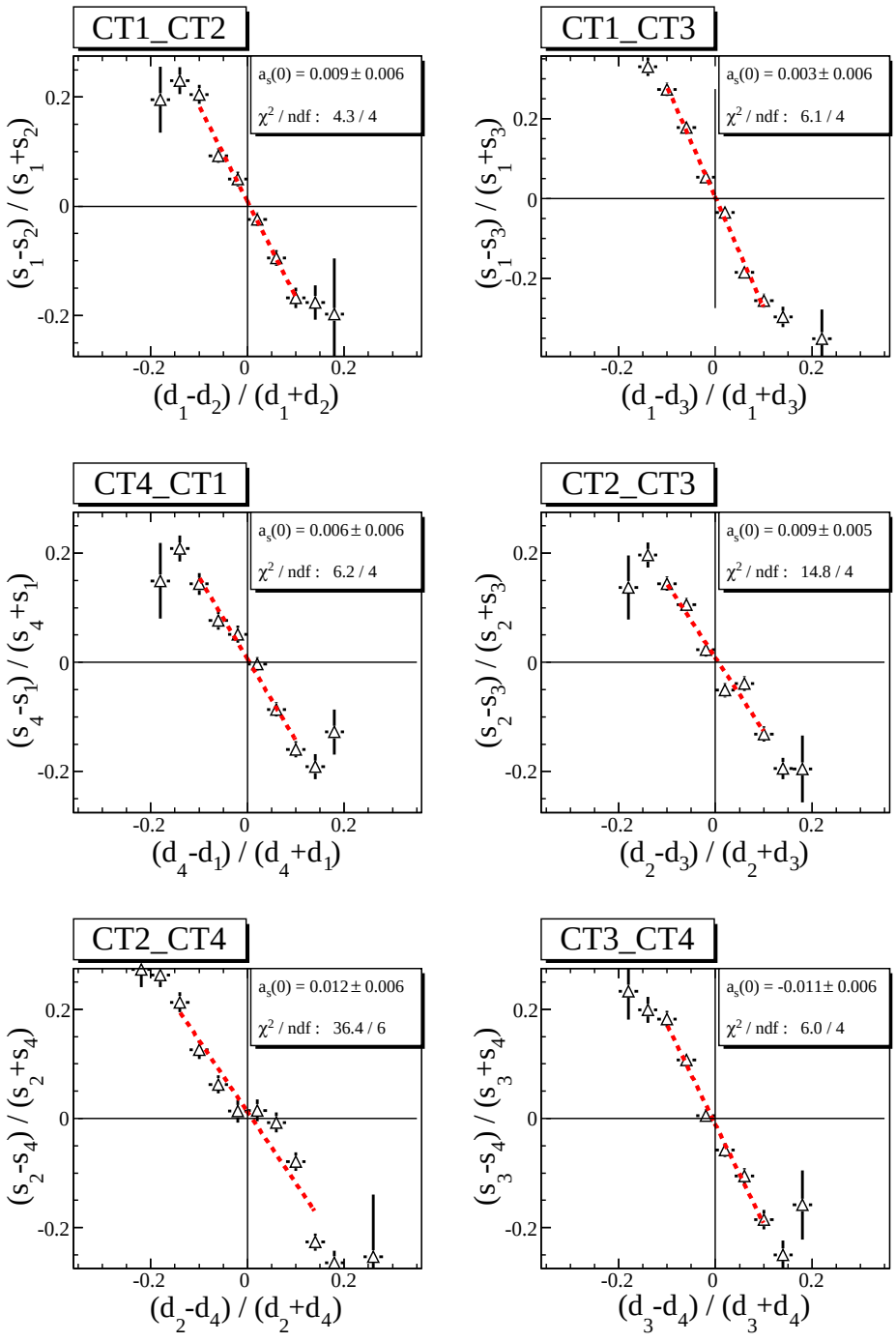

Fig. B.10: Plots used for the **linear method** for the Size-distance asymmetry plots for all six telescope pairs for the full dataset taken on the **Crab nebula** (52 runs). Only impact distances $> 130m$ are included, hence the anti-linear structure (see 4.1.3). On average, $\simeq 2500$ events were included in the plots (after applying std cuts). $a_s(0)$ denotes the intersection point of the linear fit (dashed red line) and vertical line at $x = 0$ and is taken as the intercalibration value for the specific telescope pair.

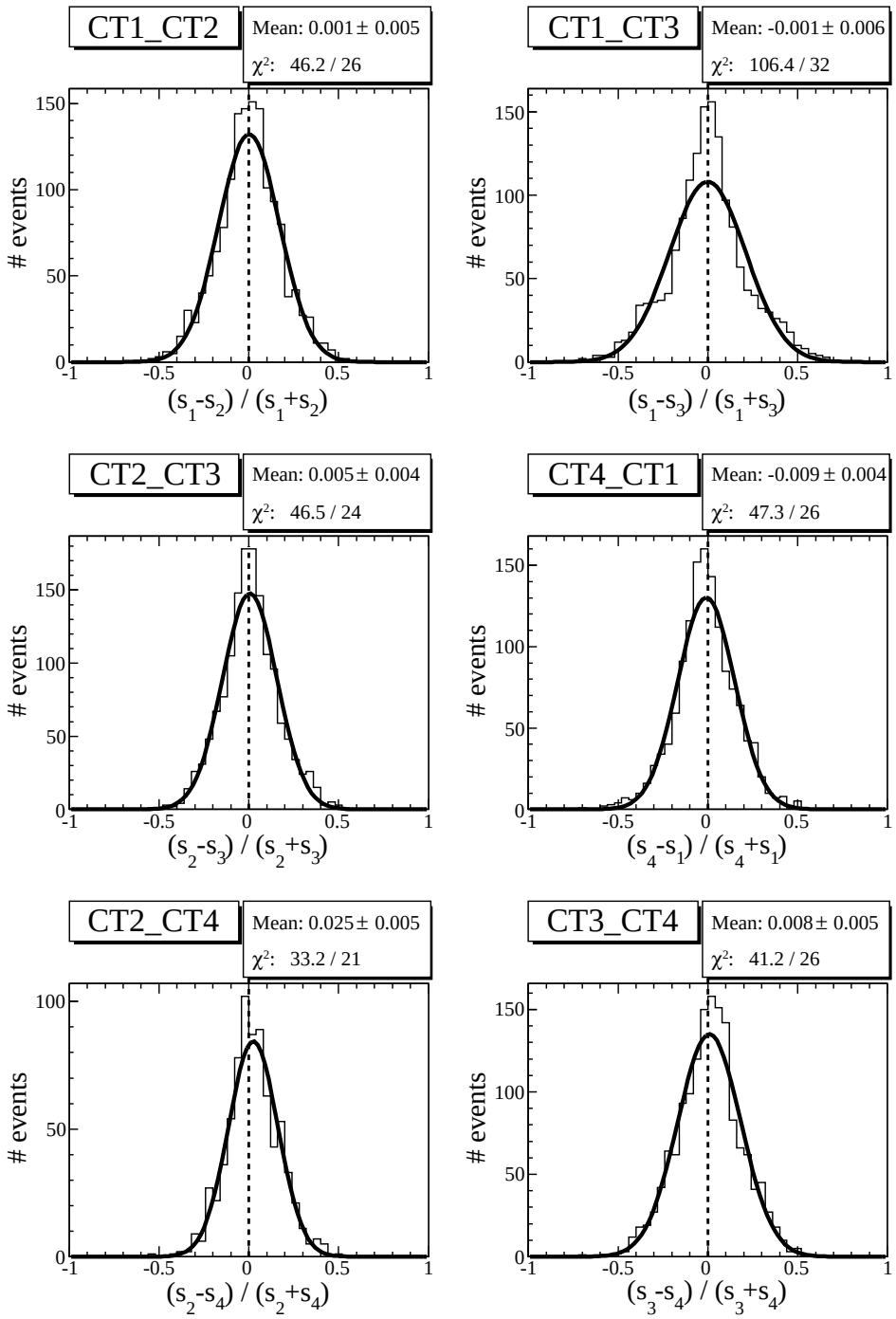

Fig. B.11: Plots used for the **Gauss method** for the Size-distance asymmetry plots for all six telescope pairs for the full data set taken on the **Crab nebula**. Only distance asymmetries whose absolute value is < 0.1 were used for the determination of the asymmetry value. On average, $\simeq 750$ events were included in the plots (after applying std cuts). "Mean" denotes the mean value of the Gauss fitted to the distribution and is used as the intercalibration value for this telescope pair.

Appendix C

Energy Intercalibration Plots

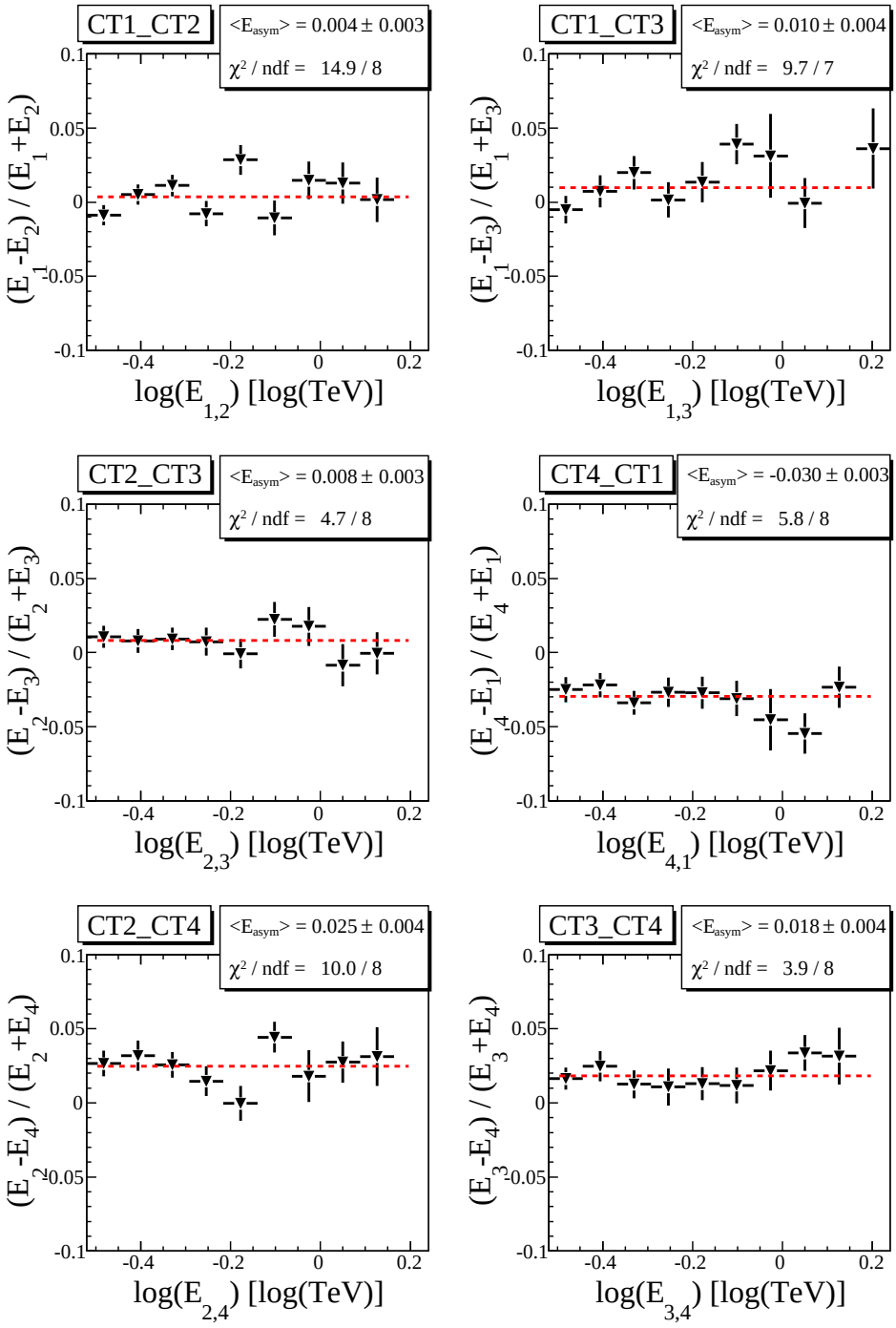

Fig. C.1: Averaged energy asymmetry as a function of the average energy reconstructed by both telescopes for all six telescope pairs and the **bigflare data set of PKS 2155–304**. $< E_{asym} >$ of telescope pair (i,j) is taken as $\overline{\Delta E_{i,j}}$.

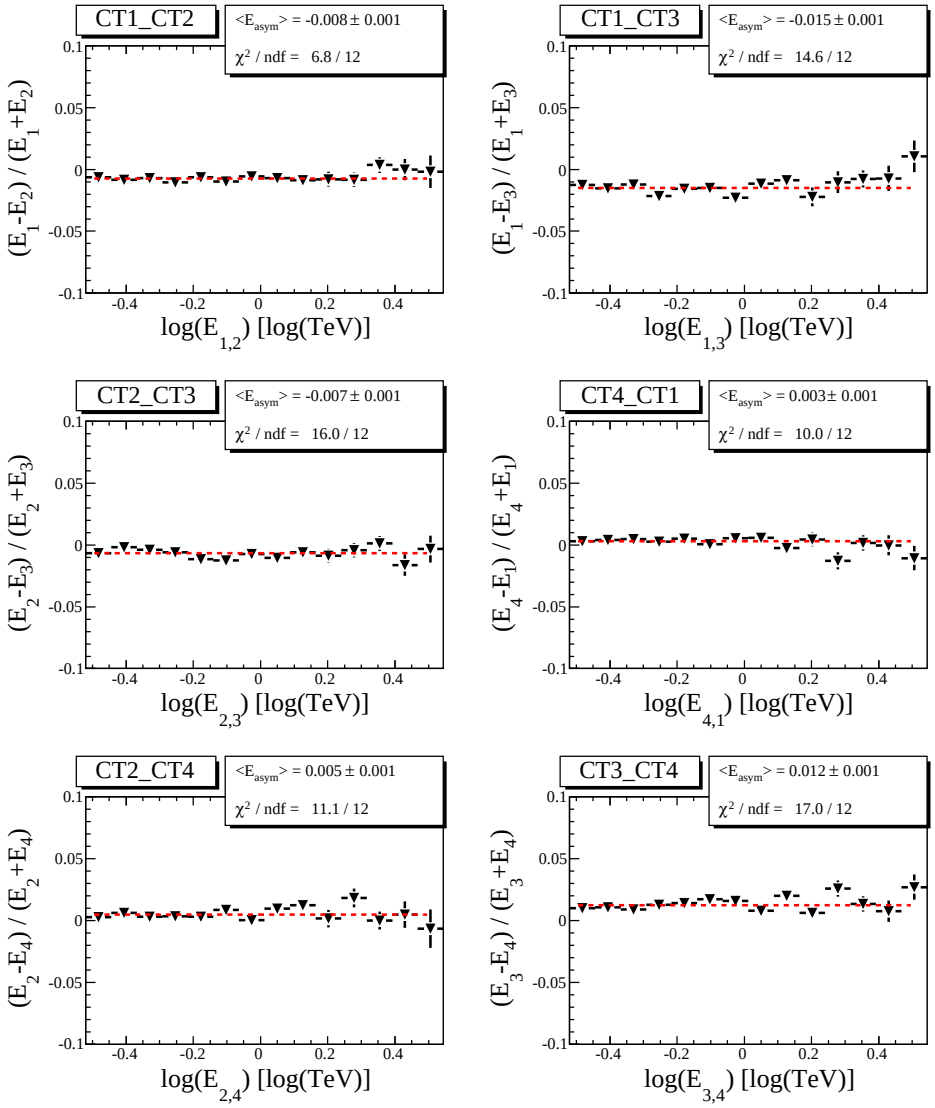

Fig. C.2: Averaged energy asymmetry as a function of the average energy reconstructed by both telescopes for all six telescope pairs and the **full PKS 2155–304 data set**. $< E_{asym} >$ of telescope pair (i,j) is taken as $\overline{\Delta E_{i,j}}$.

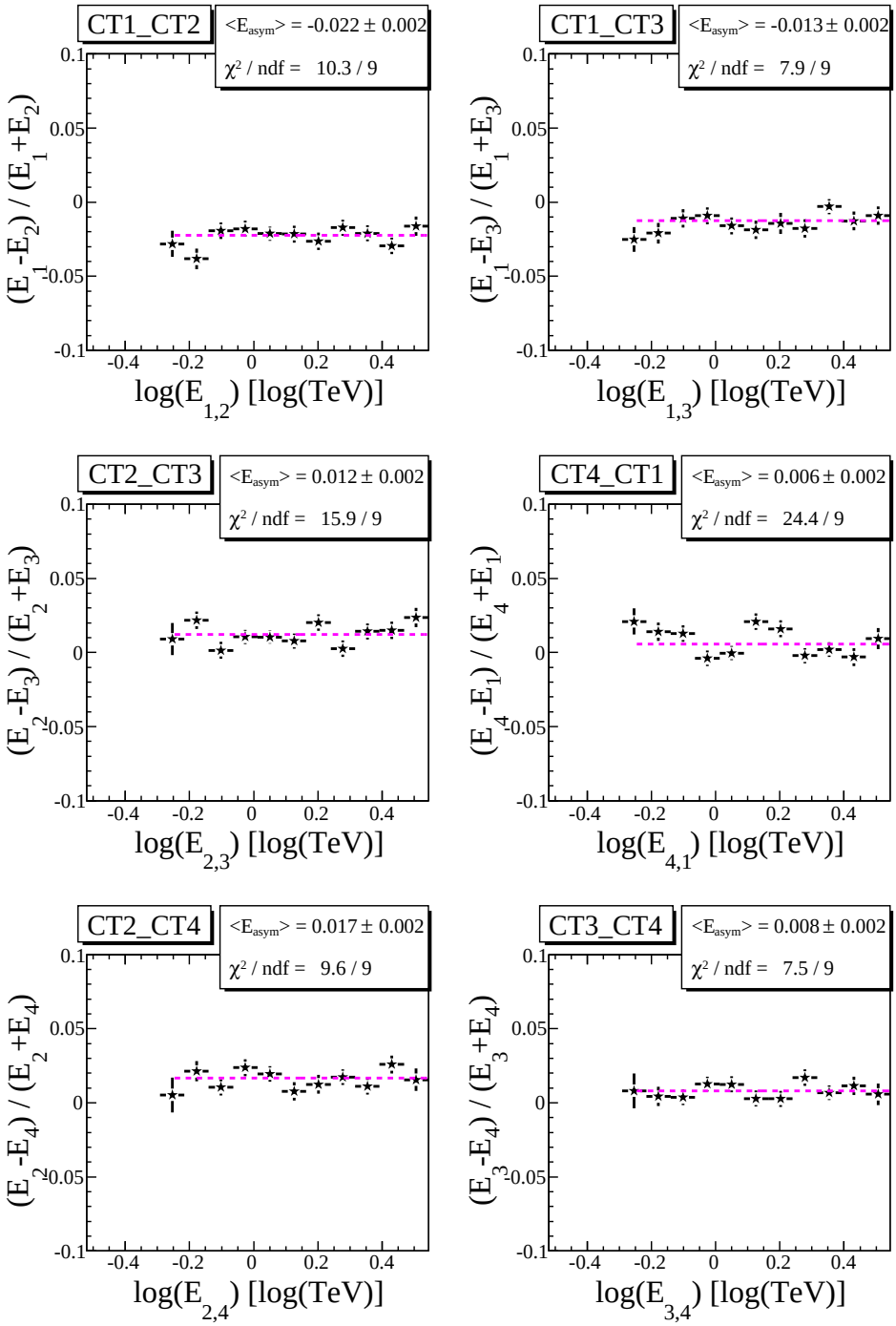

Fig. C.3: Averaged energy asymmetry as a function of the average energy reconstructed by both telescopes for all six telescope pairs and the **Crab Nebula** data set. $< E_{asym} >$ of telescope pair (i,j) is taken as $\overline{\Delta E_{i,j}}$.

Appendix D

Relative Energy Calibration Plots

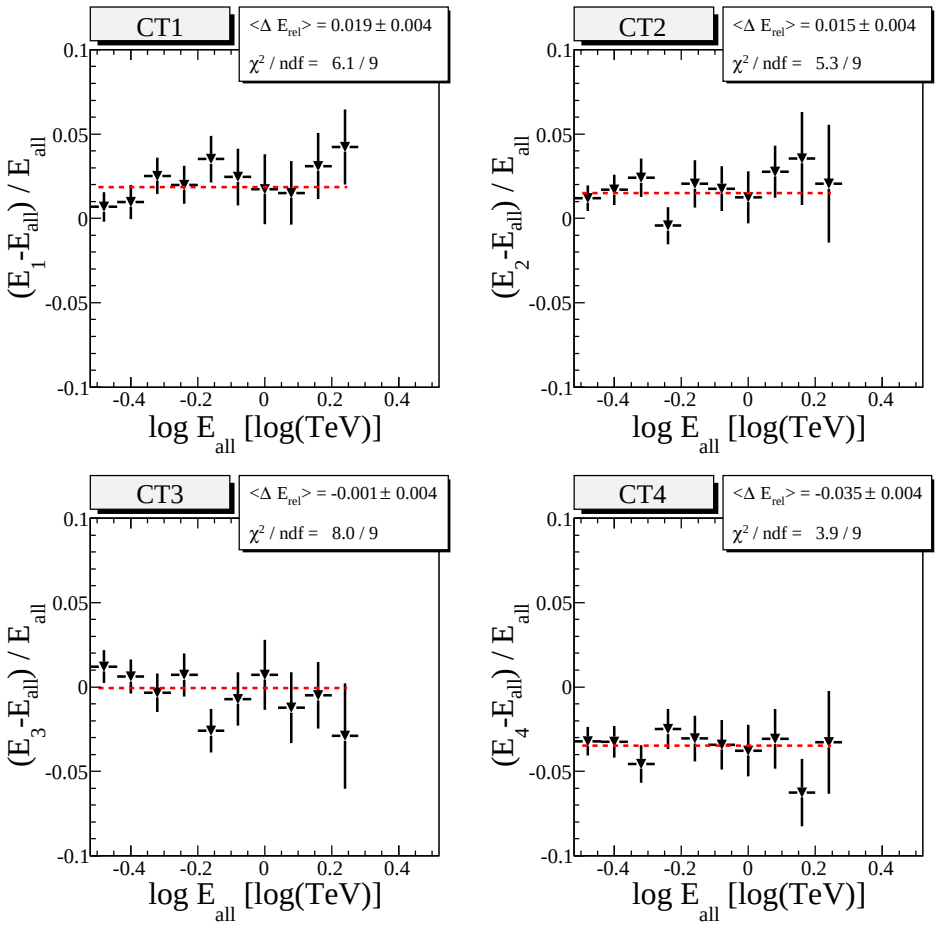

Fig. D.1: Average relative energy uncertainty as function of the mean energy reconstructed by all telescopes of the array for the **bigflare of PKS 2155–304**. $< E_{rel} >$ of telescope i is taken as $\overline{\Delta E_i}$.

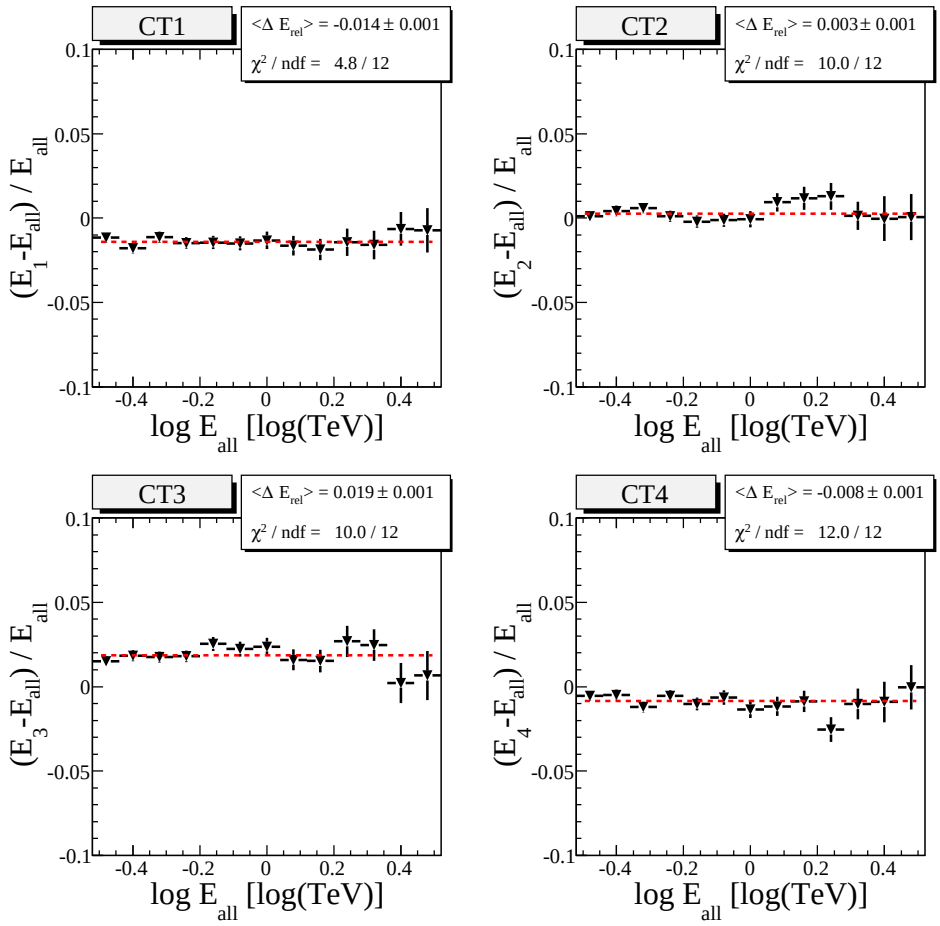

Fig. D.2: Average relative energy uncertainty as function of the mean energy rreconstructed by all telescopes of the array for the **full PKS 2155–304 data set**. $< E_{rel} >$ of telescope i is taken as $\overline{\Delta E_i}$.

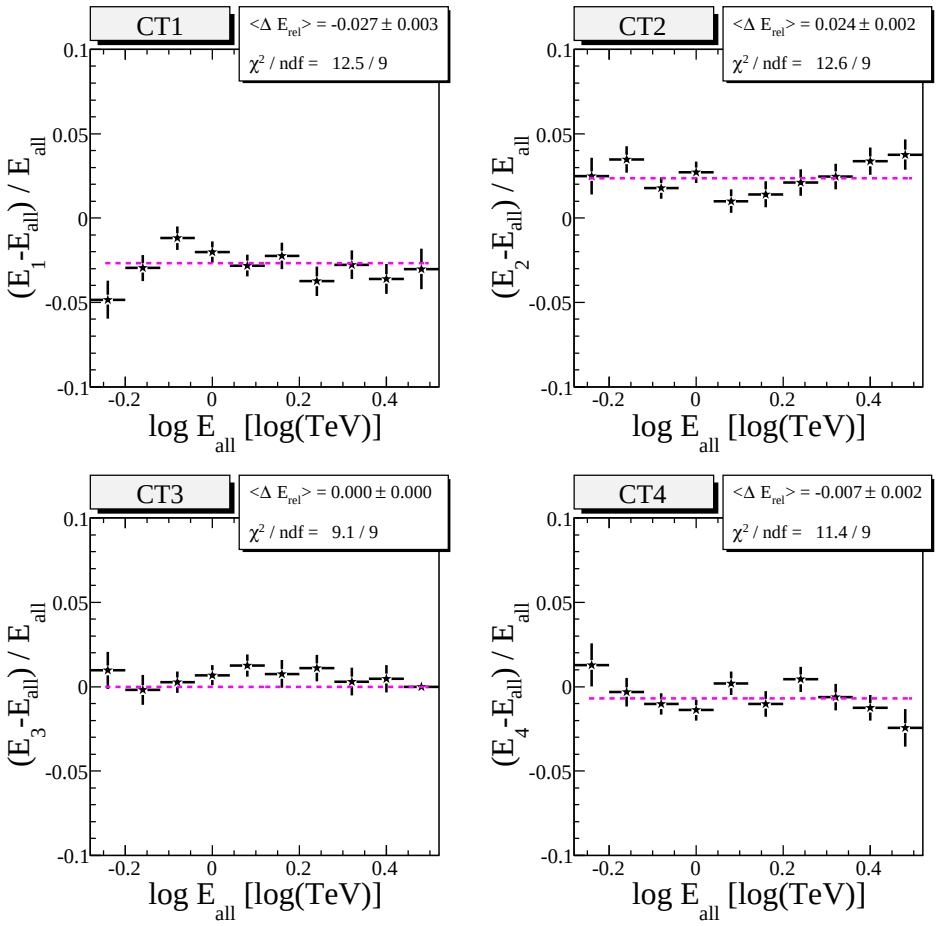

Fig. D.3: Average relative energy uncertainty as function of the mean energy reconstructed by all telescopes of the array for the **Crab Nebula**. $< E_{rel} >$ of telescope i is taken as $\overline{\Delta E_i}$.

Bibliography

[1] T. Gaisser. Cosmic Rays and Particle Physics. Cambridge University Press, 1990.

[2] V. F. Hess. *Ueber Beobachtungen der durchdringenden Strahlung bei sieben Freiballonfahrten. Physikalische Zeitschrift*, 13:1084–1091, 1912.

[3] S.P. Swordy J. Cronin, T.K. Gaisser. *Cosmic Rays at the Energy Frontier. Scientific American*, 1997.

[4] K. Zuber and H. V. Klapdor-Kleingrothaus. Particle Astrophysics. IoP Publishing, 2000.

[5] M. Nagano and A. A. Watson. *Observations and implications of the ultrahigh-energy cosmic rays. Reviews of Modern Physics*, 2000.

[6] R.Chaves et al. H.E.S.S. Collaboration. *Extending the H.E.S.S. Galactic Plane Survey. ArXiv e-prints*, 2009.

[7] H.E.S.S. Collaboration F. Aharonian et al. *Detection of Gamma Rays from a Starburst Galaxy. Science*, 2009.

[8] H.E.S.S. Collaboration F. Aharonian et. al. *Primary particle acceleration above 100 TeV in the shell-type Supernova Remnant RX J1713.7-3946 with deep H.E.S.S. observations. Astron. Astrophys.*, 2007.

[9] F. A. Aharonian. Very High Energy Cosmic Gamma Radiation. World Scientific Publishing Co. Pte. Ltd., 2004.

[10] D. Berge. The gamma-ray supernova remnant RX J1713.7-3946 with H.E.S.S. PhD thesis, Ruprecht Karls Universitaet Heidelberg, 2006.

[11] K. Berloehr. *MC images of air showers.* `http://www.mpi-hd.mpg.de/hfm/~berhlohr/HESS/`.

[12] Particle Data Group. Particle Physics Booklet. Physics Letters B, 2004.

[13] HEGRA Collaboration. *The time structure of Cherenkov images generated by TeV gamma-rays and by cosmic rays. Astroparticle Physics*, 11:363–377, 1999.

[14] S. Funk. A new population of very high-energy γ-ray sources detected with H.E.S.S. in the inner part of the Milky Way. PhD thesis, Ruprecht Karls Universitaet Heidelberg, 2005.

[15] H.E.S.S. collaboration J. Hinton et al. *Background modeling in ground-based Cherenkov astronomy.* 2005.

[16] H.E.S.S. Collaboration F. A. Aharonian et al. Calibration of cameras of the h.e.s.s. detector. *Astroparticle Physics*, 22:109–125, 2004.

[17] A.M. Hillas. *Proceedings 19th ICRC La Jolla.* 1985.

[18] W. Hofmann et al. *Comparison of techniques to reconstruct VHE gamma-ray showers from multiple stereoscopic Cherenkov images. Astroparticle Physics*, 1999.

[19] S. Ohm. *Algorithmen zur Gamma-Hadron-Separation mit den H.E.S.S.-Teleskopen.* Master's thesis, Ruprecht Karls Universitaet Heidelberg, 2006.

[20] Ti-Pei Li and Yu-Quian Ma. *Analysis methods for results in gamma-ray astronomy. Astrophysical Journal*, 1983.

[21] K. Bernloehr. *Shadowing in a H.E.S.S. telescope due to masts and other elements.* H.E.S.S. internal note, 2002.

[22] G. Rowell. *Test measurements of H.E.S.S. mirrors.* H.E.S.S. internal note, 2002.

[23] H. Krawczynski. *Study of several Winston cone geometries.* H.E.S.S. internal note, 2000.

[24] A. Koch and A. Kohnle. *Quantum and Collection Efficiency Measurements of the Photonis XP2960 Photomultipliers.* H.E.S.S. internal note, 2001.

[25] O. Bolz. Absolute Energiekalibration der abbildenden Cherenkov-Telekope des H.E.S.S. Experiments und Ergebnisse erster Beobachtungen des Supernova-Ueberrests RX J1713.7-3946. PhD thesis, Ruprecht Karls Universitaet Heidelberg, 2004.

[26] W. Hofmann. *Intercalibration of Cherenkov Telescopes in Telescope Arrays. Astroparticle Physics*, 20:1–3, 2003.

Acknowledgements

An dieser Stelle möchte ich mich bei allen Menschen bedanken, die auf unterschiedliche Weise zur Entstehung dieser Diplomarbeit beigetragen haben. Mein besonderer Dank gilt

- Professor Werner Hofmann, für die Möglichkeit am H.E.S.S. Experiment erste wissenschaftliche Erfahrungen zu sammeln, für die gute Betreuung und für die lehrreichen Gespräche im Laufe des Jahres.
- Stefan Ohm, für die intensive und gute Betreuung, dafür, dass er sich trotz Promotionsstress immer Zeit genommen hat, meine kleinen und großen Fragen zu beantworten und für seinen unermüdlichen Einsatz und die damit verbundene Geduld, mich mit den Feinheiten der H.E.S.S. Analyse-Software vertraut zu machen.
- Daniil Nekrassov, dafür, dass er immer für meine Fragen Zeit hatte, mir regelmäßig bei der Bug-Suche geholfen hat und die Arbeit in den letzten Monaten intensiv (mit-)betreut hat.
- Andre-Claude Clapson, für die Betreuung in den ersten Monaten und die Beantwortung so mancher Frage in der Zeit danach.
- Christoph Deil, dafür, dass er so ein angenehmer Zimmernachbar war und mir insbesondere im ersten halben Jahr bei meinen alltäglichen Problemen mit Linux&Co tatkräftig zur Seite stand.
- Christopher van Eldrik, für das intensive Korrekturlesen der Diplomarbeit und die vielen kleinen und großen Anmerkungen, die maßgeblich zur Verbesserung selbiger beigetragen haben.
- Anne Bochow, Douglas Hagues und Dirk Lennarz für das Korrekturlesen mancher Teile dieser Arbeit.
- Konrad Bernlöhr und Wilfried Domainko für das Beantworten mancher spezifischen Frage zu Monte Carlo Simulationen beziehungsweise zur Hochenergie-Gamma-Astronomie.
- Ruth Crespo, dafür dass sie stets bei organisatorischen Angelegenheiten behilflich war, sowie Thomas Kihm für die Hilfe bei Computerproblemen.
- Joachim Hahn, Petter Hofverberg, Ryan Chaves, Andreas Hillert, allen oben genannten und dem Rest der Heidelberger H.E.S.S. Gruppe für die angenehme Zeit und die nette Arbeitsatmosphäre während des letzten Jahres.

- Alex, Claudius, und Sebastian, für Vieles (u.a. fürs Korrekturlesen), vor allem aber für die Freundschaft während der gemeinsamen Studienzeit, für die Unterstützung in schwierigen Zeiten und für viele lustige Stunden abseits der Physik.

Zuletzt möchte ich meinen Geschwistern Christine und Jochen sowie meinen Eltern danken, dafür dass sie mich seit ich denken kann bedingungslos unterstützt haben, dass sie immer Verständnis für meine Sorgen hatten und mich stets in meinen Entscheidungen bestärkt haben.

Erklärung

Ich versichere, dass ich diese Arbeit selbständig verfasst und keine anderen als die angegebenen Quellen und Hilfsmittel benutzt habe.

Heidelberg, den 25.11.2009

(Robert Gast)